Characterization of Anodic Bonding

By

Carissa Debra Tudryn

B.M.E. Bachelor of Mechanical Engineering
The Catholic University of America, 2000

SUBMITTED TO THE DEPARTMENTS OF MECHANICAL ENGINEERING AND
MATERIALS SCIENCE AND ENGINEERING IN PARTIAL FULFILLMENT OF
THE REQUIREMENTS FOR THE DEGREES OF

MASTER OF SCIENCE IN MECHANICAL ENGINEERING
MASTER OF SCIENCE IN MATERIALS SCIENCE AND ENGINEERING
AT THE
MASSACHUSETTS INSTITUTE OF TECHNOLOGY
FEBRUARY 2004

© 2004 Carissa Debra Tudryn. All rights reserved.

Signature of author
Departments of Mechanical Engineering and Materials Science and Engineering
February 2004

Certified by
Ralph Hopkins
Charles Stark Draper Laboratory
Thesis Supervisor

Certified by
S. Mark Spearing
Associate Professor of Aeronautics and Astronautics
Thesis Advisor

Certified by
Linn Hobbs
Professor of Materials Science and Engineering and Nuclear Engineering
Thesis Advisor

Certified by
David Parks
Professor of Mechanical Engineering
Thesis Reader

Accepted by
Ain A. Sonin
Chairman, Committee on Graduate Studies
Department of Mechanical Engineering
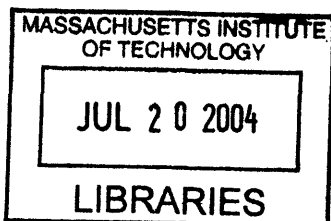
[THIS PAGE INTENTIONALLY LEFT BLANK]

Characterization of Anodic Bonding

By
Carissa Debra Tudryn

Submitted to the Departments of Mechanical Engineering and Materials Science and Engineering on January 16, 2003, in partial fulfillment of the requirements for the dual degrees of Master of Science in Mechanical Engineering and Master of Science in Materials Science and Engineering.

Abstract

Anodic bonding is a common process used in MicroElectroMechanical Systems (MEMS) device fabrication and packaging. Polycrystalline chemical vapor deposited (CVD) silicon carbide (SiC) is emerging as a new MEMS device and packaging material because of its excellent material properties including high strength, hardness, and thermal conductivity. An alternative, low temperature glass to CVD SiC anodic bonding process is required in order to prevent gold tin braze stress relaxation. A novel process recipe, requiring a SiC RMS surface roughness of 45nm, was developed for anodically bonding CVD SiC to bulk and thin-film, lapped Pyrex^{TM} and Hoya SD-2^{TM} glass substrates. The bond quality, residual curvature, and microstructured interfacial features for CVD SiC anodic bonding were shown to be comparable to single crystal silicon (Si) anodic bonding. The Plaza Test specimen, invented by Plaza et al., was used to assess bulk and thin-film, lapped glass bond quality. A two-part contact/bonding model was used to predict the contact and bonding of the Plaza Test structures. Surface contact was predicted by a parallel plate capacitor pull-in model after the voltage was applied, and linear elastic fracture mechanics (FEA) modeling predicted the toughness or work-of-adhesion of the bonded surfaces after the formation of a permanent silicon dioxide bond. The role of the voltage, structure geometry, work of adhesion, and materials used in the model predicted that the bonding mechanism limited the total number of structures that remained bonded. The thin-film, lapped glass bond quality improved when increasing the voltage and time. The calculated, experimental, and modeled thermoelastic curvatures were minimal, indicating low residual stress between the bonded materials. Finally, microscopy and elemental analysis showed distinct differences in elemental depletion band(s) of bulk Pyrex^{TM} and Hoya SD-2^{TM} glasses bonded to Si, and in interfacial bonding between Pyrex^{TM} and CVD SiC compared to Pyrex^{TM} and Si. More elements in the glass network are identified as participating in the depletion layer process than identified in previous studies. Overall, the process recipes, modeling, experimental work, and chemical analysis of glass to CVD SiC anodic bonding showed that CVD SiC can be bonded successfully and be a promising packaging material.

Thesis Supervisor: Ralph Hopkins
Title: Staff, Charles Stark Draper Laboratory
Thesis Advisor: S. Mark Spearing
Title: Associate Professor of Aeronautics and Astronautics
Thesis Advisor: Linn Hobbs
Title: Professor of Materials Science and Engineering and Nuclear Engineering
Thesis Reader: D. Parks
Title: Professor of Mechanical Engineering

[THIS PAGE INTENTIONALLY LEFT BLANK]

Acknowledgements

I would like to express my sincere gratitude to the following people for their guidance, wisdom, and assistance in my dual masters thesis. This thesis involved an extensive amount of thought, fabrication work, and experimental and modeling analysis, which could not have been done by myself. I am also grateful to have been offered a Draper Fellowship. I received the best of both worlds, MIT and Draper, and the best of two masters in Mechanical Engineering and Materials Science and Engineering.

I truly appreciated the lengthy insight, edifying discussions, constant supervision, and challenges from my primary MIT advisors, Profs. Mark Spearing and Linn Hobbs. I'm very grateful to my MIT reader, Prof. David Parks, who gave me insight into future modeling analysis. By attending Spearing's group meetings, I gained a lot of knowledge from other graduate student's research, and their suggestions and observations were valuable to my own research. I thank Kevin Turner for all the discussions, patience, and wisdom. I also express thanks to Hyung-Soo Moon, Dongwon Choi, Christine Tsau, DJ Shim, and Jeremy Gregory. I'm appreciative to Ivan Lee, and Rob Bernstein for use of their lab equipment. I'm grateful to Dr. Stefan Schweizer who assisted me with the arduous TEM prep and analysis. A big thanks to Leslie Regan who always lends a helping hand and ear to each graduate student.

I truly appreciated my Draper Supervisor's, Ralph Hopkins, constant availability, knowledge, patience, and confidence in my research. A sincere thank you to all the Draper technicians and staff who were always catering to my frequent needs involving fabrication work, equipment/software use, or research discussions: Jeff Borenstein, Amy Duwel, Bill Sawyer, Mark Mescher, Matt Varghese, Dave Nokes, Connie Cardoso (my saving grace), Manuela Healy, Bessy Silva, Katherine Ashton, Isaac Costa, Brian Orrick, Mert Prince, Jim Cousens, Bill Donovan, Dave Porter, Peter Sebelius, Richard Caruso, and Jim Bickford. Thank you to the staff who gave me a gift of a Draper window office during my final months.

Not only did I bond samples, but I also had the pleasure of bonding with my friends, roommates, and officemates in order to escape the stresses of class and research: Sarah, Yabei, Marisa, Cari, Robin, Janelle, Femme Cards, PERG, Chris, Anne, Aimee, Kevin, Jaime, Nadine, Mimi, Krissa, Matt, Jeb, Kara, Kyrilian, Gary, Raj, and Dave. I also met many friends along the way training with the MIT Triathlon Club and for marathons, being on AHEC, and involved with NMB and Mars Society. I thank COL Young for all his support and funding of the JPL Mars Mission Robotics Videoconferences. Every evening I came back to a pleasant dorm, Ashdown: thank you, Terry and Anne, Denise, and Cissy.

I have been blessed with a family, who has been a perpetual support throughout my life. They deserve the most heartfelt appreciation. My parents (Mama and

Daddeo), brother (TJ), and sister's (Jessica and Melissa) undying faith, sacrifice, soothing spirit, guidance, judgment, and love have built the person I am today. My grandparents (Nana, Papa, Omi, and Opa), aunts, uncles, and cousins have also given me undying love, support, and encouragement. Each has allowed me to keep my "out-of-this-world" dream alive.

Last, but not least, thank you, Alexis. You have a special place in my heart, and I look forward to learning and dreaming with you.

"Commit to the Lord all you can and your plans will succeed." Proverb 16:3

MARS OR BUST...

Table of Contents

[THIS PAGE INTENTIONALLY LEFT BLANK]

List of Figures

List of Tables

[THIS PAGE INTENTIONALLY LEFT BLANK]

Chapter 1 Introduction

1.1 Device Packaging

Device packaging design is critical to the performance of MEMS (MicroElectroMechanical Systems) microsensor and microactuator devices. The device package provides a stable thermal and mechanical environment, and electrical and hermetic isolation from the external environment [1,2]. A crucial step in the fabrication of a MEMS device is the method used to attach it to the package. The device-attachment method must provide high stability, low creep, low residual stress, and reliable process control.

The system under study is shown in Figure 1-1. The silicon-on-glass MEMS sensor device is attached to a polycrystalline, chemical vapor deposited (CVD) silicon carbide (SiC) package. Typically, a gold-tin braze is used to attach the MEMS device to the CVD SiC packaging. The gold-tin braze yield point is exceeded during the device-attachment, (packaging process), causing creep and/or stress relaxation over time. An alternative device-attachment process is needed to reduce and/or eliminate this gold-tin braze stress relaxation.
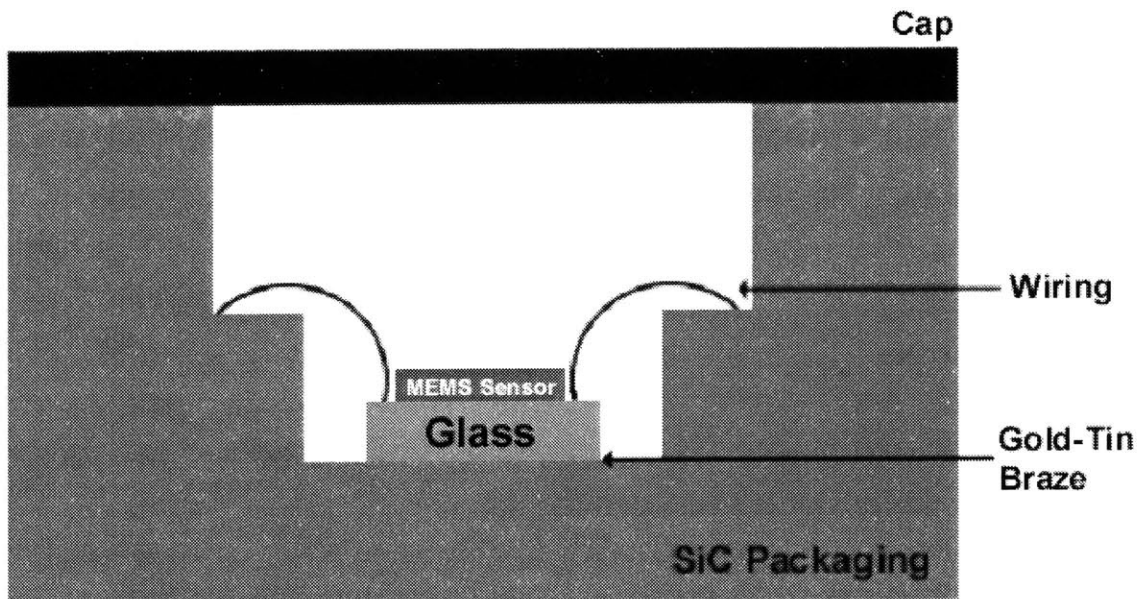
Figure 1-1: SiC Packaging of a MEMS Device

1.2 Device-Attachment Process Requirements

A low-temperature device-attachment process is desirable to implement high-strength, stable bonds between the MEMS device and its package. Anodic bonding is a preferred bonding technique, because it is a low temperature process and produces hermetic and mechanically strong seals [3]. A low temperature packaging process is advantageous because it avoids potential degradation of and damage to the MEMS device and circuitry, and minimizes residual stresses generated by the thermal expansion coefficient (TCE) difference between the materials [3]. Large residual stresses negatively affect the performance of the MEMS device. These stresses lead to distortions in the device output, and in extreme circumstances may cause bond failure.

CVD SiC is emerging as a MEMS packaging material because of its excellent material properties and close TCE match to common materials such as silicon (Si), and HOYA SD-2^{TM} and Pyrex^{TM} (Corning #7740) glasses. Other desirable SiC properties include high strength, chemical resistance, thermal conductivity, hardness, and hermeticity, which are all important for use in harsh environments and in high temperature, power, and frequency devices [4]. Pyrex^{TM} is a borosilicate glass that has been the most widely used to bond to Si because of its high sodium content (known to be a significant factor in the anodic bonding mechanism) and the fact that it has a close TCE to Si. More recently, Hoya SD-2^{TM} glass has been formulated for Si anodic bonding applications because its TCE is more closely matched to Si, from room temperature to the bonding temperature than Pyrex^{TM} [5]. HOYA SD-2^{TM} and Pyrex^{TM} are closely matched in TCE to Si and to CVD SiC over a wide temperature range, as shown in Section 3.1.

The overall approach of using CVD SiC anodic bonding to glass as a packaging solution will benefit the MEMS field significantly. A low stress packaging process, using the anodic bonding technique and CVD SiC, Pyrex^{TM}, and Hoya SD-2^{TM} glass, should be particularly advantageous to commercial applications

such as RF devices, gyroscopes and accelerometers, and precision optical devices.

1.3 Review of Underpinning Technologies

1.3.1 Anodic Bonding

Anodic bonding involves the bonding of glass or ceramics to Si or metals under an applied voltage (200-1000V) and elevated temperature (200-500°C) [2]. This technique has been widely used in the MEMS field to bond a variety of glasses, metals, alloys, and semiconductor materials [2]. Not only have Hoya SD-2[TM] and Pyrex[TM] glasses been bonded to Si, but several other glasses have also been bonded, such as the borosilicate glass, Corning #7070, Tempax (Schott #8330), soda lime # 0080, potash soda lead #0120, and aluminosilicate #1720 [2,6]. Several metals, alloys, and semiconductors with similar TCE have been bonded to these glasses, including, tantalum, titanium, Kovar, Niromet 44, Aluminum, Fe-Ni-Co alloys, silicon, and gallium arsenide [2].

Bulk glass anodic bonding to Si is a mature technology, but bonding Si to Si using a thin glass film (thin film anodic bonding) is a less developed process. The development of a thin film anodic bonding process will enable fabrication of MEMS devices having negligible residual stress [7]. Section 2.2 describes Si-to-Si anodic bonding or thin-film glass anodic bonding processes in detail.

1.3.2 SiC for MEMS

SiC technology used in the MEMS field is still under development. There are a few examples of using SiC in fabrication processes. Micromachined polycrystalline SiC micromotors have been fabricated using a multilayer fabrication process. This process uses low temperature deposition and micromolding techniques to fabricate SiC structural components [8]. Presently, SOI, silicon-on-insulator technology, is widely used in MEMS fabrication. SiC-on-insulator or semi-insulating wafers are also used in microwave applications [4]. The "smart cut process[TM]" is one technique being used to form SiC-on-insulator

[4] . Several other techniques have been explored, but all have several drawbacks such as defects produced from lattice mismatch, when growing epitaxially SiC on Si, and SiC surface roughness hindering direct bonding [9]. Tong et al. [9] explored an alternative process to develop SiC-on-insulator by using anodic bonding. Section 2.3 explains this process in detail.

1.3.3 Packaging

The technology of MEMS packaging continues to be an engineering intensive effort because almost every device requires a custom package development. The evolution of standard packaging methodologies that can be used for a wide variety of devices and applications will have a profound effect on the use of MEMS in systems, for reasons of both improved functionality and reduced development and production costs.

1.4 Research Objectives

There are three principal objectives of the research carried out for this thesis:

1. To establish a protocol in order to bond bulk and thin film Pyrex^{TM} and HOYA SD-2^{TM} glass to CVD SiC.
2. To assess bond quality using the Plaza Test Mask [10].
3. To establish whether residual stresses formed after anodic bonding are consistent with the expected thermoelastic response.

1.5 Thesis Outline

Chapter 2 begins with a review of the anodic bonding literature. This review presents a summary of the bulk glass anodic bonding mechanism, thin-film (Si-to-Si) and SiC anodic bonding techniques, and methods used to characterize anodic bond strength and toughness. There is also a discussion about the Plaza test specimen that is implemented in this study. Finally, Section 2.4 details the device-attachment approach, deduced from available literature. Chapter 3 discusses modeling the bonding and bond toughness for bulk glass bonded to Si

and CVD SiC. Chapter 4 details experimental procedure, sample preparation, and process variables, for bonding bulk glass to Si and CVD SiC. This chapter also presents the results and a discussion of the modeling procedures described in Chapter 3, as well as the chemical analysis performed on bulk glass samples. In Chapter 5, two thin-film bonding techniques are discussed and their resulting bond quality assessed. Finally, Chapter 6 provides an overall conclusion and recommendations for future work.

[THIS PAGE INTENTIONALLY LEFT BLANK]

Chapter 2
Review of Science and Technology of Anodic Bonding

2.1 Anodic Bonding Bulk Glass to Silicon

2.1.1 Mechanisms

Since the invention of anodic bonding in 1969 [11], there has been much research conducted to deduce the mechanisms involved. The following review describes the likely physical mechanisms, particularly as evidenced in current changes with time, and the supporting analytical chemical findings of several researchers.

Anodic bonding is performed by heating a glass and metal (or semiconductor) sandwich, across which a d. c. voltage is applied. Typically, a glass and p-type Si are bonded together. The cathode is attached to the glass and the anode to the Si, so that the Si is at a positive potential with respect to the glass. Figure 2-1 shows a schematic depiction of this electrochemical process [12]. Both silicon and glass remain relatively stiff during the bonding process, since temperatures well below the respective melting point of Si and glass transition temperature are used [12]. This irreversible bonding process produces a permanent chemical bond at the glass/Si interface involving an intermediary SiO_2 interface layer [3,5,13]. With the application of heat and voltage, two types of reactions occur in forming this SiO_2 intermediate bond: ion dissociation/ association reactions and interfacial bonding reactions [14]. The elevated temperature permits ionic conduction within the glass, while the imposed potential drives the migrating ions of opposite charge towards the interface or towards the cathode. The glass behaves as an electrolyte at elevated temperatures because of these mobile ion species. Cations (principally Na) move through the glass toward the negatively-charged cathode. Since the cations move toward the cathode, a depletion layer is formed, and the glass network reconstructs. Therefore, this reconstruction allows for the excess

anionic oxygen species, under the influence of the electrostatic potential, to move towards the interface. The space charging of the depletion layer generates an interfacial electrostatic field. These electrostatic forces pull the glass and Si surfaces together, and hold them during the formation of a permanent bond. The contact starts at a single point between the interfaces, spreads over the remaining area, and allows the diffusion of oxygen anions into the positively charged Si [13,15]. Bond formation can occur only between surfaces that are clean and have sufficiently low surface roughness. The surfaces must be clean because particles will cause unbonded regions and not allow for complete, physical surface contact. Ko et al. [2] state that the glass and metal RMS surface roughness should be less than 1 μm in order for bonding to occur.
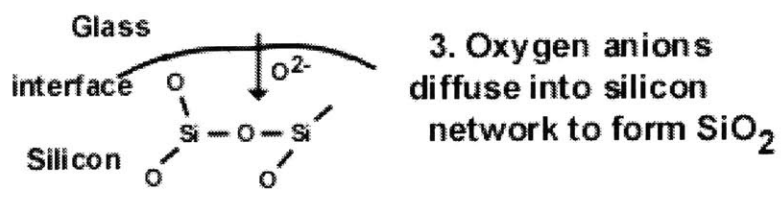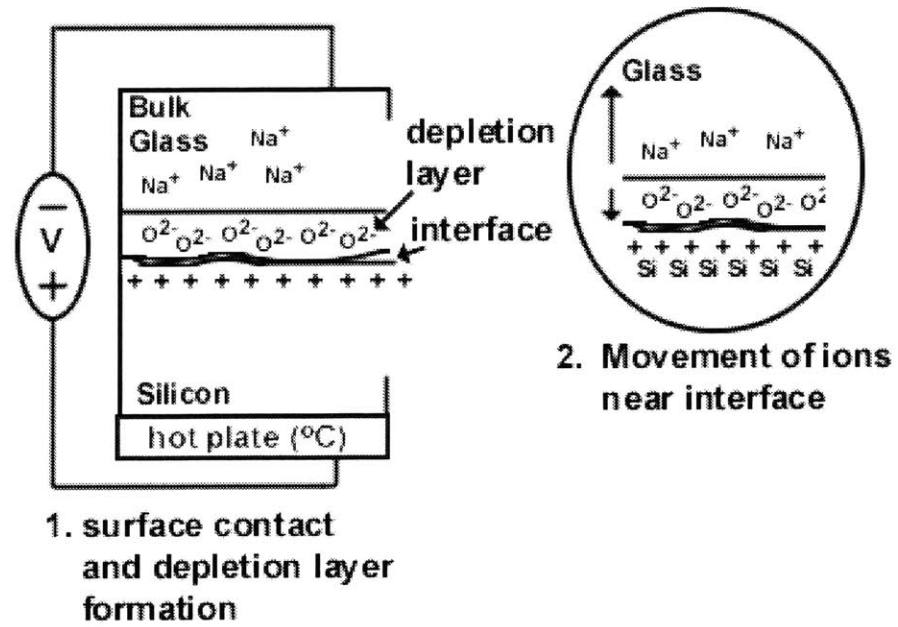
Figure 2-1: Processes Occurring at the Interface During Anodic Bonding

20

The progress of anodic bonding process is monitored typically via the current flowing through the circuit. Albaugh [12,16] modeled the current transient response, d^2I/dt^2, of the current (I) vs. time (t) plot in Figure 2-2. Figure 2-3 shows the depletion layer defined as a variable capacitor, and the bulk glass as a variable series resistor. The model was successfully fitted to the initial experimental current transient response at short bonding times. Modeling longer bonding times proved less successful. This was presumed to be because of leakage across the depletion layer, and because there are several mobile ion species responsible for current flow [16]. Albaugh [12] determined that the current decreases quickly at the beginning of the bonding process because of the initial charging of the depletion layer, and the area under this initial peak gives information about the amount of charge that is leaving the depletion layer.
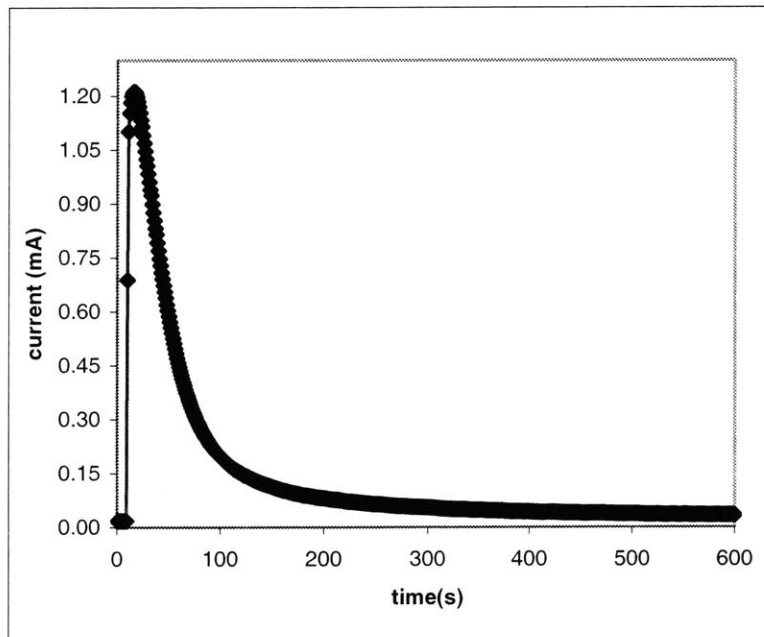
Figure 2-2: Current vs. Time: Pyrex^{TM} bonded to Si at 1kV, 350°C, 10 minutes
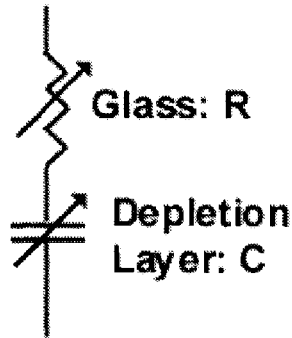
Figure 2-3: Albaugh's Model [12]

The current vs. time kinetics are controlled by the imposed bonding conditions, such as voltage, temperature, environment, and surface chemistry, and Si doping. The findings of Cozma and Puers [17] indicate that a larger in integrated current produces a higher bond quality, and faster overall bonding. Higher voltage, and lower temperature increased the current peak, hence smaller bonding times were needed [17]. Longer times were needed when using low voltages, temperatures, and n-type silicon. The low voltages cause the electric field at the interface to be lower, so that the oxygen anions cannot drift with a high enough drift velocity and to maintain the high oxidation rate at the bond front. Lower temperatures do not allow the rapid build-up of space charge at the interface because of a glass conductivity that decreases exponentially with lower temperature [17]. Lee et al. [18] discovered that a longer time, in excess of 38 minutes, was needed when bonding n-type Si to Pyrex™ glass, compared to the 4 minutes needed to bond p-type Si. Since p-type Si is doped (usually) with boron, it has extra holes in the Si valence band. Therefore, under a strong electric field, these can migrate toward the cathode (to the Si surface nearest the glass). Lee et al. maintain that there is a higher interfacial electrostatic pressure, which in turn, increases the bonding speed [18]. The bonding environment also affects the current peak. The current peak increased when bonding in air compared to in vacuum or an argon environment [17]. However, the mechanisms are unclear. Oxygen in air possibly participates in the bonding process, or the heat transfer in a vacuum is poor [17]. Finally, Cozma and Puers [18] found that hydrophilic Si surfaces, resulting from treatment with a 65% boiling nitric acid solution, and hydrophobic surfaces, resulting from an HF dip,

did not exhibit significantly different current peaks. These results conflict with results the findings of Lee et al. [19] that a hydrophilic Si surface gave a distinguishably higher bonding current and bonded area compared to a hydrophobic Si surface. Lee et al. also performed a chemical analysis that is described below.

Microscopy and chemical analysis of the surface chemistry and glass composition has also been used to further elucidate the mechanism of anodic bonding. The glasses used have amorphous structures composed of many elements. Pyrex[TM] glass is a Na-borosilicate glass, while Hoya SD-2[TM] is a Zn-aluminosilicate glass. Table 1 shows the glass compositions of Pyrex[TM] and Hoya SD-2[TM] glasses. The following recent chemical analyses result have shed further light on anodic bonding mechanisms.

Table 1: Pyrex[TM][1] and Hoya SD-2[TM][2] Glass Composition

Glass	Compound	SiO_2	B_2O_3	Na_2O	Al_2O_3	MgO	ZnO	As_2O_3	Other trace elements
Pyrex[TM]	Mol %	80.6	13	4	2.3	0	0	0	0.1
Na-borosilicate									
HOYA SD-2[TM]	Mol %	25-70	1-5	1-5	20-30	2-5	10-20	1-5	0
Zn-aluminosilicate									

Recently, Nitzsche et al. [6] discounted the long-standing assumption that only sodium cations (Na^+) participate in the depletion of the glass, and that correspondingly, oxygen (O^-) anions from within the glass network diffuse into Si. These investigators used nuclear magnetic resonance (NMR) and *in situ* elastic recoil detection analysis (ERDA) to observe bridging oxygen in glass, and to identify a combined hydrogen (H) and Na depletion zone. From these observations, they were able to propose the revised bonding model that is

---

[1] Pyrex Data Sheet, downloaded from the Corning, Inc.
<http://www.corning.com/lightingmaterials/products/index_pyrex.html> accessed August 6, 2002
[2] Hoya Corporation, Glass Substrates for Silicon Sensors, CA, USA

described here. Borosilicate glasses, such as Pyrex[TM] and Tempax (Schott no 8330), are composed of a continuous random network of Si and boron (B) atoms connected by bridging oxygen atoms. The addition of Na_2O to the glass network causes the formation of negative potential wells bounded by B atoms or non-bridging O ions (NBOs) (Figure 2-4) [6]. Most of the Na cations reside in these potential wells, electrostatically bonded to the negatively charged NBOs at room temperature. Previous authors postulated that thermal excitation moves some of the sodium ions into the intra-network space and allows them to drift to the cathode, forming a sodium depletion layer. However, Nitzsche et al., argued that since there are bridging oxygen atoms in glass, the drift of oxygen anions to the interface and the formation of a hydrogen depletion layer occur from the hydrolyzed glass surface, where water molecules from the ambient environment have diffused into the glass surface, producing hydrolyzed Si-OH: HO-Si bonds or remaining as molecular water [6].

Bridging Oxygen   Non-Bridging Oxygen
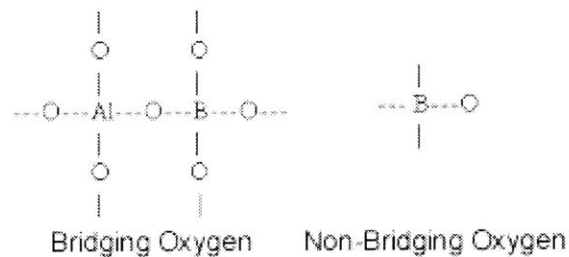
Figure 2-4: Glass Network [6]

Once the voltage is applied, the first result is that the water in the hydrolyzed layer dissociates through electrolysis into H^+ and the hydroxyl group, OH- [6]. The H^+ moves to the cathode and OH- to the anode (glass/Si) interface.   Next, sodium, potassium (K), calcium (Ca), and possibly aluminum (Al) depletion layers develop along with a hydrogen depletion layer. Nitzsche et al.'s [6] ERDA findings for Tempax glass, which has a composition similar to Pyrex[TM], showed that Na diffusion leaves a distinguishable depletion layer near the interface[6]. The other alkali metal, K, along with Ca also were also found to contribute to the depletion layer process. The formation of an Al depletion layer occurred only

using a temperature of 400°C and voltage of 400V. It is presumed that all these reactions therefore occur and determine the rate of anodic bonding. In the amorphous network structure of these glasses, tetrahedral, $[AlO_4]$- and $[BO_4]$-, groups exist. Na is weakly bonded to these tetrahedral groups. Very small activation energies are required for ion migration between the different bonded sites [6].

$$[AlO_4]Na + H+ == [AlO_4]H + Na+$$
$$[BO_4]Na + H+ == [BO_4]H + Na+$$
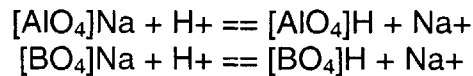
Once the depletion layer develops, the applied electric field impels OH- towards the interface. The hydroxyl groups temporarily bond with Si in unstable $Si(OH)_4$ complexes, and which dissociate to form more stable SiO_2 and evolve H_2O [6]. This proposed mechanism still supports an electric-field-assisted oxide growth at the interface [6].

$$Si + 4[OH]- = Si(OH)_4 + 4e-$$
$$Si(OH)_4 = SiO_2 + 2H_2O$$
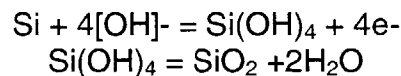
The Si-O bonds at the glass-Si interface are covalent and lead to the high interfacial strength characteristic of anodic bonding. It can be assumed that Hoya SD-2™, or any other oxide glass is subject to a similar mechanism since hydrolyzed layers can readily form at glass surfaces from the ambient water vapor. Hoya SD-2™ has a glass network similar to that of borosilicate glasses. In borosilicate glasses, boron is not tetrahedrally-coordinated without sodium present. Sodium increases the boron coordination and connectivity in the glass network. In aluminosilicate glasses, aluminum is not tetrahedrally-coordinated without sodium present, too.

Xing et al. [13] used Transmission Electron Microscopy (TEM) and Electron Probe Microanalysis (EPMA) to detect more than one depletion layer, just as Nitzsche et al. [6] found. TEM micrographs were taken of several samples bonded under an array of different conditions ranging from voltages of 500V or 800V, temperatures of 250°C - 400°C, and bonding durations of 2 –11,400

seconds. Each of these micrographs showed several distinct bands or layers in the glass parallel to the glass/silicon bonded interface [13]. Xing et al. [13] suggested that these bands were possibly depleted of ions, i.e. sodium and even hydrogen, involved in the bonding mechanism. The regions grew larger as the bonding time increased, but not all of the pictures showed multiple bands. These authors, in agreement with Nitzsche et al. [6], suggested some of the bands might arise from hydrogen piling up in the hydrolyzed glass layer, because H^+ cations can occupy the sites of depleted sodium cations. Xing et al. [13] hypothesized that multiple bands were not found near the interface under all the different bonding conditions because certain temperatures and bonding times gave more distinguishable depletion layers. EPMA results showed a depletion of sodium near the interface and a diffusion of oxygen into the Si. Precipitate-like defects in the Si were evident in the TEM micrographs. This suggested diffusion of oxygen into the Si, which is consistent with earlier literature [13].

Visser et al. [20] used energy-dispersive x-ray spectroscopy (EDX) and an Cameca SX100 electron microprobe to examine the anodic bonding mechanisms of both Pyrex[TM] and Hoya SD-2[TM] glasses. A chemical analysis of the interface was performed upon reversing the voltage on the anodic bond. Bulk Pyrex[TM] and Hoya SD-2[TM] glasses were bonded to bulk p-type Si using a temperature of 400°C, 1000V, and durations of 30 minutes to 1 hour. The voltage was reversed at these same bonds by making the glass positive and the silicon negative. After reversing the bonding process using a temperature of 400°C, voltages of 400V or 1000V, and times of 10 minutes to 1 hour, several defects were produced at the anodically bonded interface [20]. Since two glasses with different chemical compositions were bonded, two types of defects were produced. The electron micropobe scan showed the Na and K concentrations decreased from an interfacial defect into the bulk Pyrex[TM] glass. When reversing the polarity, the Na and K fluxes reverse direction and accumulate at the interface, causing defects which were visible as "brown spots" [20]. The reversed polarity caused a different phenomenon to occur at the bonded Hoya SD-2[TM] / Si interface.

Debonded areas were formed at the interface from an accumulation of craters and several brown spots, which caused each sample to break apart easily. Microprobe scans of the "brown spots" and craters showed that the brown spots were caused by an accumulation of Na, similar to those observed in Pyrex[TM]. The zinc (Zn) concentration was also scanned, but was shown not to participate in the formation of these defects. However, the Zn concentration was depleted near the defects, so it was assumed to have been involved in the anodic bonding mechanism [20].

Finally, the role of the surface chemistry in the sodium depletion layer depth was analyzed using secondary-ion mass spectroscopy. Lee et al. [19] created hydrophilic surfaces on Pyrex[TM] and Si wafers by submersion in a solution comprising ratio of 6parts DI water: 1 part Hydrogen Peroxide: 4 parts Ammonium Hydroxide at 65°C for 5 minutes, and bonded them together using voltages of 60-300V and temperatures of 200-300°C. The SIMS analysis showed that the hydrophilic surfaces created deeper sodium depletion layers at the interface [19]. These results suggest that the hydroxyl groups, -OH, induced a higher potential and corresponding electrostatic force compared to that established during the regular anodic bonding process [19]. Figure 2-5 illustrates schematically the supposed role of the hydroxyl groups in bonding opposing hydrophilic surfaces of two Si wafers.
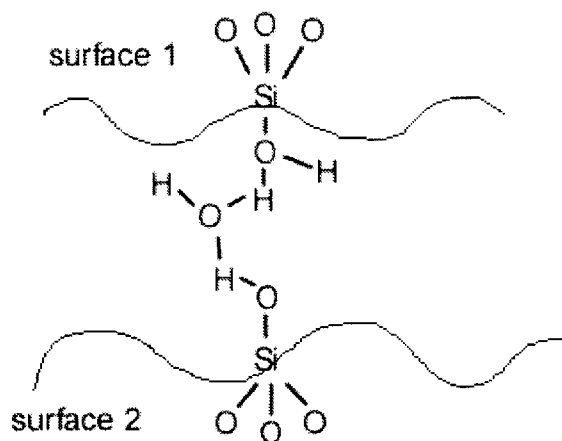
Figure 2-5: Hydrophilic Surface Bonds [21]

Once the -OH groups form hydrogen bonds, the gap between the materials at the interface is reduced, causing a higher electric field to pull the materials together and to form a bond. These results also suggest that hydrophilic surfaces apparently form deeper depletion layers of sodium ions because there are more hydrogens available for the oxygen anions to bond to at the interface. The SIMS analysis provides important, direct evidence that hydrophilic surfaces do participate actively and are important in the anodic bonding process.

In summary, the literature accounts suggest that anodic bonding involves a complex combination of mechanisms. Bonding conditions and material choice greatly influence the exact mechanisms that will occur. Although there are differences between the materials, the steps of cation migration into the glass, anion (O⁻) migration to the interface, followed by the formation of covalent Si-O bonds, is common to all the postulated mechanisms.

2.1.2 Strength and Toughness Methods to Characterize Anodic Bond Quality

Two measures of anodic bond quality are mechanical strength and toughness. Bond strength and toughness have been measured using several test methods: pressure, tension, shear, bending, and fracture mechanics. These methods were used to determine the bond strength and bond toughness as a function of process parameters such as voltage, temperature, and the pretreatment of the surface [5].

Obermeier [22], together with other authors [5], found that bond strength results from fracture tests were inaccurate because the values were not repeatable, and failure occurred in the glass, not at the glass/Si interface. Obermeier [22] used tensile tests to determine the bond strength using bond conditions similar to Wallis [11]. Bond strengths of 30-40 MPa were found for bonds made at 900V and 450°C, compared to the 10.3-20.7 MPa Wallis [11] found using 800V and 500°C. Obermeier's samples failed 100-200μm into the glass from the interface,

so the bond strength values did not give accurate interfacial strength, and reflect the strength of the glass and the residual stress in the bond.

Another fracture test method, using fracture mechanics, was performed to quantify interfacial bond toughness. This technique also relied on a destructive tension test to propagate a crack along the interface. Hurd et al. [23] performed a linear elastic bimaterial fracture mechanics study of the bonded interface between the brittle materials, Pyrex™ and Si. The crack was initiated along the interface using chevron-notched (CN) and straight-through-cracked (STC) compact tension tests. Hurd et al. [23] measured mode 1, plane-strain, fracture toughness as a function of temperature under bonding conditions of 1000V and 30 minutes. Even this linear-elastic fracture technique did not give accurate interface values, because the crack propagated into the more compliant glass. These values correspond to the fracture toughness at a distance 300-500μm from the interface for the CN tests, and 150-250μm from the interface for the STC tests. The CN test specimens yielded reproducible fracture toughness values of 0.63 to 0.68 MPa-m$^{1/2}$ at bonding temperatures in the range of 300-450°C. The STC specimens yielded fracture toughness values of 0.66-0.75 MPa-m$^{1/2}$ at the same temperatures.

In summary, bond strength and bond toughness measurements typically do not produce values characteristic of the interface. In addition, the use of fracture tests can introduce extraneous influences, such as the effects of the residual stress and initial flatness variations, in the final measured strength or toughness. The bond quality using different bonding parameters must be found using another technique.

2.1.3 Bond Quality using the Test Specimen: Plaza Test Mask

Plaza et al. [10] invented another technique to measure bond quality by comparing the electrostatic pressure to bond strength. These authors invented the "Plaza Test Mask" consisting of circles and rectangles of different widths and etch depths. Figure 2-6 shows an acoustic microscope view of the mask.
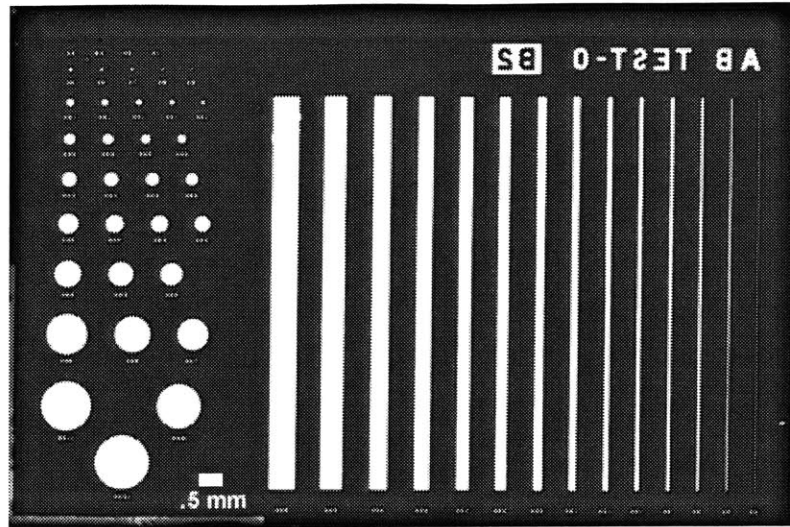
Figure 2-6: Plaza Die Test Mask

The effect of the bonding conditions on the quality of the bonded interface was measured by calculating the electrostatic pressure needed to form a bond between two surfaces with a fixed separation. If the structure remains bonded, then the bond force is assumed to be larger than the elastic restoring force equivalent to the electrostatic pressure. The bonding of the structures is a function of the mask variables (width, etch depth), process variables (voltage, temperature), and geometric and material specific variables such as surface roughness, ionic mobility, etc. The L_{test} and H_{test} values defined in Figure 2-7, are the length and etch depth of a particular structure. Chapter 3.2 details the mechanics governing the bonding of these structures.
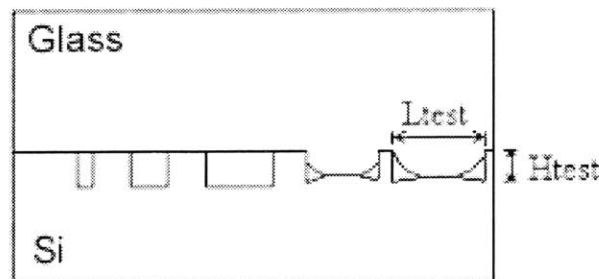
Figure 2-7: Plaza Test Structures [26]

In general, bonding will become more difficult as H_{test} increases and L_{test} decreases. This same trend was also shown in their experimental work. Higher

applied voltages and temperatures bonded deeper etch depths and narrower structures.

The following shows Plaza et al.'s measurement of bond quality by reference to electrostatic pressure. The bond quality was characterized in two steps, first, a visual inspection of which Plaza Test structures actually bonded, and then a calculation of the electrostatic pressure determined by the applied voltage and etch depth. Figure 2-8 shows an acoustic microscope image of bonded and unbonded Plaza Test structures. The nine dark circles and the seven dark rectangular structures represent bonded structures, the white contrast unbonded structures.
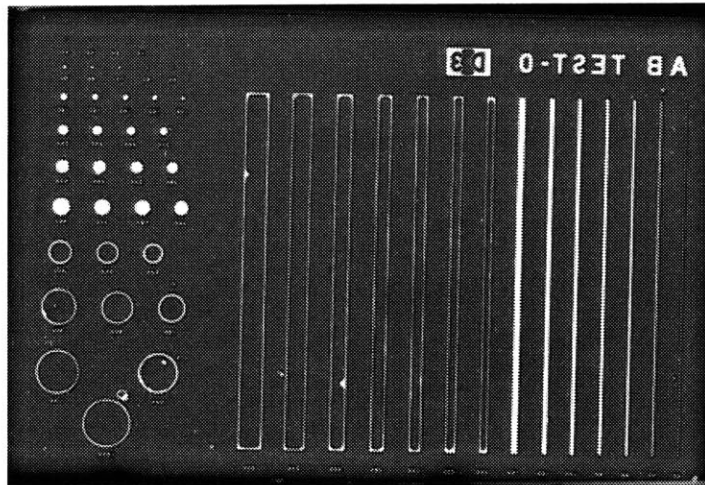
Figure 2-8: Plaza Test Mask Bonded Sample

Next, Equation 2.1 was used to calculate the overall electrostatic pressure of all the structures in Figure 2-8 [10].

$$P = \frac{1}{2}\varepsilon_o \frac{V^2}{H_{test}^2} \quad (2.1)$$

where V is the applied voltage, ε_o is the permittivity of free space (8.85e-12 C/Vm) and H_{test} is the etch depth of the structures. The derivation of Equation 2.1 is made using the model of a parallel plate capacitor in Chapter 3.3.1.

The rectangular and circular structures of Figure 2-8 were bonded using 1000V and an etch depth of 0.2μm. Eqn. 2.1 predicts a constant bond quality among all the structures of Figure 2-8 at those particular bonding conditions represented by an electrostatic pressure of 110.6MPa.

There are several shortcomings in the Plaza et al. analysis.

1.   The electrostatic pressure equation is derived from a parallel plate capacitor model. It is not clear whether this can be applied to the actual bonding process of the structures, and if electrostatic pressure is a measure of bond strength.

2.   Plaza et al. mentioned that if the value of electrostatic pressure is calculated, then the effect of the voltage will more accurately determine the bond quality [10]. The voltage, temperature, time etc. affect the bonding of the overall Plaza Test structures too.

3.   It is not clear if there is a difference in the extent of bonding when the voltage is applied during bonding and after it is removed.

2.2 Thin-Film Glass to Silicon Anodic Bonding

Thin-film anodic bonding, or Si-to-Si anodic bonding, is an alternative procedure that has been studied to bond silicon together using an intermediate thin-film glass layer. Using a very thin glass is advantageous compared to bulk glass because the difference in TCE between materials is not significant, so the thermally-induced stress is reduced. It is anticipated that these thin-film anodic bonds will have less temperature sensitivity [7]. The overall anodic bonding mechanisms when bonding Si-thin-film glass to Si, forming a Si-thin-film glass-Si sandwich, is assumed to be similar to bonding bulk glass to Si.

There are two processes that are used to form this Si- thin-film glass -Si sandwich structure. A thin-film of Pyrex^{TM} glass is deposited by either sputter deposition or electron-beam evaporation onto Si, and then the opposite side of the glass is anodically bonded to Si. Figure 2-9 shows the bonding process of this sandwich.

1. Thin-film Glass Depostion onto silicon dioxide

thin-film glass

SiO$_2$ layer

silicon

2. Anodic Bonding to Silicon

silicon

anodic bond

V

silicon
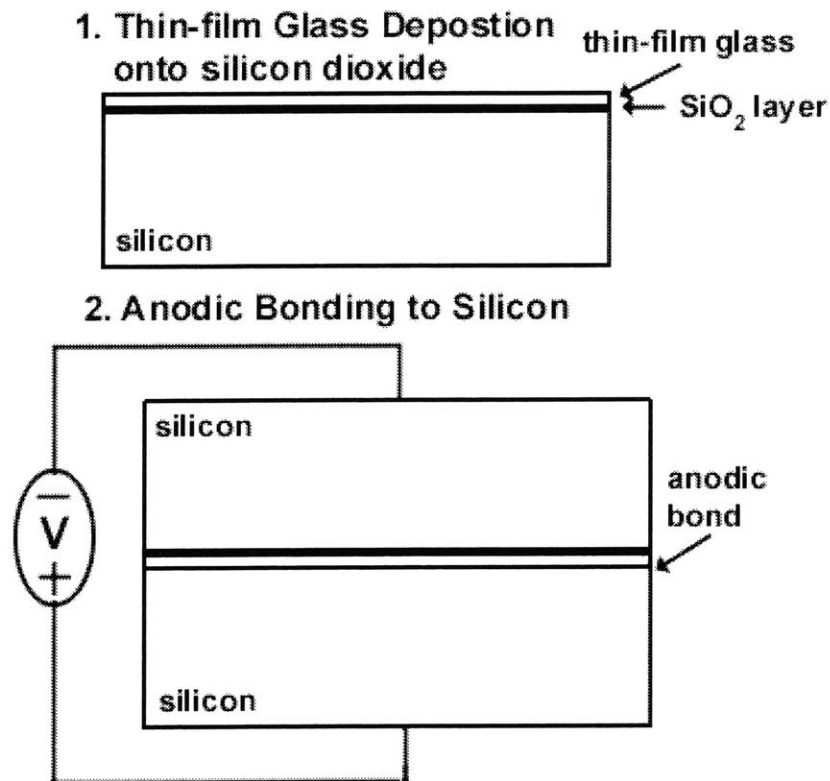
Figure 2-9: Thin-Film Anodic Bonding Process

Sputter deposition is a well-known process invented in 1972 by Brooks and Donovan [7]. Since the layer of sputtered Pyrex^{TM} is very thin (20nm-2000nm) and the composition of sputtered Pyrex^{TM} yields a lower dielectric constant, lower voltages are used, along with a silicon dioxide (SiO$_2$) layer [5,7]. The SiO$_2$ layer further increases the dielectric strength, so the sputtered glass layer will not break down.

A radio frequency (RF) sputtering system is used to sputter thin glass layers from a Pyrex^{TM} glass plate target onto Si wafers. Since the sputtered glass film carries a high residual stress from deposition, annealing it at 550°C in a nitrogen

environment ensures stress relief [7]. Jakobsen et al. [5] noted that RF sputter deposition required long times (greater than 14 minutes [24]) to ensure a glass layer with a suitable composition for anodic bonding. In general, the composition of this sputtered layer does not compare to that of the bulk Pyrex^{TM} glass composition. Figure 2-10 and Figure 2-11 compare the X-ray photoelectron spectroscopy (XPS) analysis of the sodium, oxygen, and silicon concentrations in sputtered Pyrex^{TM} glass, before and after the nitrogen (N_2) anneal, to a bulk sample and to Corning data. After the N_2 anneal, the sputtered Pyrex^{TM} layer of glass is slightly more Si rich and more depleted in Na (0.3% vs. 0.4% before the anneal) [25]. However, these values are much lower than for bulk Pyrex^{TM} (1.6 to 2.3%) [25]. It is known that sodium plays a crucial role in the anodic bonding mechanism, so sputtered Pyrex^{TM} layers may not be so reliable for anodic bonding.
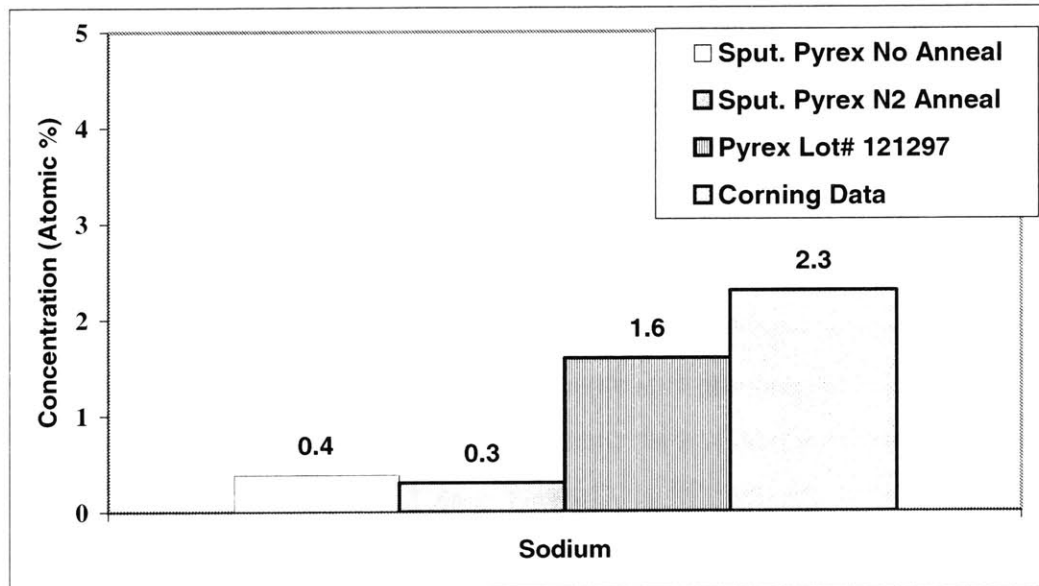
Figure 2-10: XPS Analysis Sodium [25]
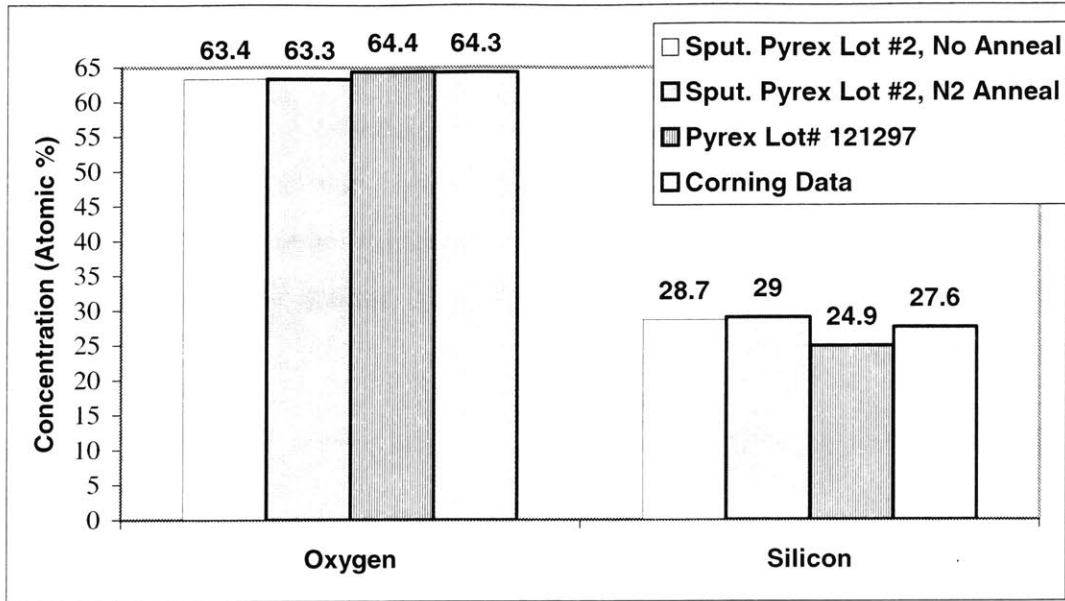
Figure 2-11: XPS Analysis of Oxygen and Silicon [25]

Many authors have found varying results bonding sputtered Pyrex[TM] layers. Jakobsen et. al [5] summarized that some authors found that thin sputtered layers of 20 nm thickness using 10V had bonded, while others found that layers thinner than 500nm did not bond. Hanneborg et al. [7] successfully bonded 2.0 μm of sputtered Pyrex[TM] on Si to another Si wafer, using 300 nm of SiO_2, 400°C, 200V, and 10 minutes. Given the large number of variables, such as temperature, voltage, time, annealing conditions, composition of sputtered glass, and thickness of SiO_2, involved in this process, it is not surprising that results vary considerably.

A more recent, and probably more promising, technique to bond Si to Si via a thin-film glass layer relies on evaporated glass [5]. The authors [5] noted that this deposition technique is three times faster than sputter deposition. Higher deposition rates yielded thicker glass layers at shorter times and compositions with higher breakdown voltages. Evaporated Pyrex[TM] glass layers on Si also yielded higher concentrations of sodium ions (secondary ion counts: evaporated glass > 10^5 a.u. versus sputtered glass < 10^4 a.u.) [24]. Similar to the sputtered glass process, these evaporated layers also required an intermediate oxide layer

and an anneal to relieve process-induced stress. Choi et al. [24] found that evaporated Pyrex™ glass layers thicker than 1.5μm exhibit a lower surface roughness similar to bulk and sputtered glass, which was adequate for Si bonding with voltages of 35-100V, and temperatures of 135°C - 240°C. Since this technique has been recently developed, Jakobsen et al. [5] cautioned that it is still evolving, and much more analysis needs be performed in order to give repeatable results.

2.3 SiC Anodic Bonding

As mentioned before, several materials have been successfully bonded together using the anodic bonding process. Tong et al. [9] have begun the exploration of anodic bonding SiC for use in fabricating silicon carbide on insulator (SiCOI). Recently, Di Cioccio et al. [4] developed a SiCOI technique using the "Smart Cut Process™." Di Cioccio et al. [4] demonstrated successful direct bonding of a hydrogen-implanted SiC wafer to a silicon wafer. They found it necessary to ensure that both wafers had polished, hydrophilic deposited oxide layers. Once direct bonding was complete, a high temperature anneal (1100°C) was performed to split-off the implanted hydrogen layer from the bulk SiC [9]. Tong et al. [9] developed a more reliable and simple SiC-on-insulator technique using anodic bonding instead of direct bonding. They found that the anodic bonding of SiC wafers to glass was more advantageous because surface roughness, a hydrophilic surface, and silicon dioxide layers had less effect on the bonding [9]. A technique was developed to fabricate a thin layer of single crystal 6H-SiC on high temperature (800°C) glass. The ultimate purpose of their process development was to obtain a thin layer of SiC, which could subsequently be used as a substrate for the epitaxial growth of gallium nitride used for GaN-based light-emitting diodes and lasers [9].

SiC bulk wafers of 240μm thickness were H_2^+ ion implanted. The ions penetrated to a peak depth at 0.5μm, and then the SiC wafers were annealed at 800°C for 0.5 hours. Once the ion implantation and annealing steps were

complete, the wafers were anodically bonded to the high temperature glass at 560°C using voltages of 800-1000V. Finally, the SiC layers bonded to the glass were split from the bulk SiC wafer using a thermal anneal treatment at 760°C. These authors studied the annealing temperatures after implantation, and the anodic bonding process. A successful method was found to create a thin SiC layer/glass sandwich that did not have a bond with cracks or defected layers, nor suffered plastic deformation in the glass which affected the final SiC surface roughness.

2.4 Device-Attachment Process Development

This literature review has provided information regarding the different facets of anodic bonding and suggests more areas to explore. The following thesis objectives result from specific findings of this review that were selected for application to the device-attachment process development.

There is relatively little prior work on anodic bonding of SiC to glass. Tong et al. [9] anodically bonded single-crystal SiC to high temperature glass, but this is not relevant to MEMS applications. Packaging MEMS devices using a bulk SiC-glass process requires a lower anodic bonding temperature than in Tong et al.'s work, since other low melting temperature metals are used in the MEMS fabrication process. An innovative, low-temperature technique of anodically bonding bulk and thin-film Pyrex^{TM} and HOYA SD-2^{TM} glasses to a new material, polycrystalline CVD SiC, is developed using appropriate bonding conditions. The anodic bonding of glass to p-type Si is used as a reference for the anodic bonding of bulk glass and thin-film glass to polycrystalline, CVD SiC. P-type Si is used, because Lee et al. [18] found that it results in a faster bonding process.

The anodic bonding of bulk glass to p-type Si and CVD SiC is characterized in several ways using the "Plaza Test Mask" specimen, and control samples without the mask. Different bonding conditions are used in order to determine the extent of the Plaza Test structure bonding. A two-part model is explored to analyze the bonding of the Plaza Test structures and determine the overall bond toughness,

both while the voltage is applied and when it is removed. Hydrophilic surfaces are used in order to determine an increase in bonded structure area and bonding current. The role of residual stress in the bonding process is investigated. Curvature values of the bonded control samples are calculated using plate theory and finite element analysis, measured experimentally, and compared with literature values of the TCE for the bonding materials.

The mechanism occurring in the bulk glass when bonding to Si and CVD SiC is characterized using a high-resolution nanostructural and nanochemical analysis. Transmission Electron Microscopy (TEM) and Scanning Transmission Electron Microscopy (STEM)/ X-ray energy dispersive spectroscopy (XEDS) are used to analyze both Pyrex^{TM} and Hoya SD-2^{TM} glasses. The objectives of the TEM part of the study are to find depletion layers at the Pyrex^{TM}/Si interface as Xing et al. [13] found, and observe if Hoya SD-2^{TM} exhibits this trend. The STEM analysis chemically analyzes the depletion layers in both glasses to see which elements are depleted during bonding. Nitzsche et al. [6] performed a detailed chemical analysis on Tempax^{TM} glass which is very similar in composition to Pyrex^{TM} glass, but not Hoya SD-2^{TM} glass. The mechanism, occurring in Hoya SD-2^{TM} glass, was chemically analyzed by Visser et al. [20], but only in cases in which the polarity was reversed at the anodic bond. The STEM study shows the elemental depletion affect during the regular anodic bonding process. Both TEM and STEM are used to study the mechanism when bonding Pyrex^{TM} to this new polycrystalline, CVD SiC material.

Finally, the experimental procedure of bonding thin-film anodic bonding of sputtered glass is performed, since sputter deposition is a well-established technique. The bond quality of thin-film glass to p-type Si and CVD SiC is determined using the bulk glass approach along with acoustic microscopy.

Chapter 3
Modeling of Bulk Glass to Silicon and CVD Silicon Carbide

This chapter describes the models used in the remainder of this thesis: the Plaza Test Mask deformation model, the two-part bonding model, and models for characterizing toughness, and residual curvature resulting from bonding bulk glass to Si and CVD SiC.

3.1 Materials Modeled

There are four materials modeled in this study: Pyrex[TM], Hoya SD-2[TM], p-type Si and polycrystalline CVD SiC. The two glasses, p-type Si, and polycrystalline CVD SiC, are assumed to be linear elastic and isotropic. Silicon is a single crystalline cubic material with anisotropic material properties. The p-type Si has the (100) plane normal to the bonding surface. The material properties of Si are isotropic in this plane, and more specifically, the biaxial modulus, $[E/(1-\upsilon)]_{(100)}$, is constant, as shown in Equation 3.1, and independent of orientation or direction [1]. This justifies the use of isotropic elastic properties for both materials.

$$\left(\frac{E}{1-\upsilon}\right)_{(100)} = \frac{1}{S_{11}+S_{12}} \tag{3.1}$$

Using values, $E_{(100)}$=130.2 GPa, $\upsilon_{(100)}$=0.279, and compliance constants, S_{11}=6.04e-12/Pa and S_{12}=15.6e-12/Pa [1, 26], the isotropic relationship (3.1) is satisfied.

The silicon carbide used is a polycrystalline, free-standing, monolithic, bulk material fabricated using Morton's chemical vapor deposition process[3]. This polycrystalline material also has isotropic material properties[4]. Since there is no experimental shear modulus established, it was found using Equation 3.2 [1]:

[3,4] Morton Advanced Materials, CVD Silicon Carbide, MA, USA

$$\mu = \frac{E}{2(1+\upsilon)} \qquad (3.2)$$

using values, E = 466 GPa and υ= 0.21[5]. Table 2 and Table 3 show material property data for all the materials, which are taken from the company material data sheets.

Table 2: Modulus of Elasticity and Poisson's Ratio of Materials [26][6,7,8]

Material	E, Modulus of Elasticity (GPa)	υ, Poisson's Ratio
Pyrex[TM]	63.6	0.2
HOYA SD-2[TM]	86.8	0.244
p-type Si (100)	130.2	0.279
CVD SiC	466	0.21

Table 3: Shear Modulus of Materials [27] [9,10,11]

Material	Shear Modulus, μ (GPa)
Pyrex[TM]	26.2
HOYA SD-2[TM]	34.9
P-type Si	79.0
CVD SiC	192.56

The materials modeled have similar TCE's over the bonding temperature range. Figure 3-1 shows the effective ΔTCE between Pyrex[TM] and HOYA SD-2[TM] glasses, Si, and CVD SiC from 20°C to 350°C.

[5,6,11] Morton Advanced Materials, CVD Silicon Carbide, MA, USA.

[7,9] Pyrex Data Sheet, downloaded from the Corning, Inc.
<http://www.corning.com/lightingmaterials/products/index_pyrex.html> accessed August 6, 2002
[8,10] Hoya Corporation, Glass Substrates for Silicon Sensors, CA, USA
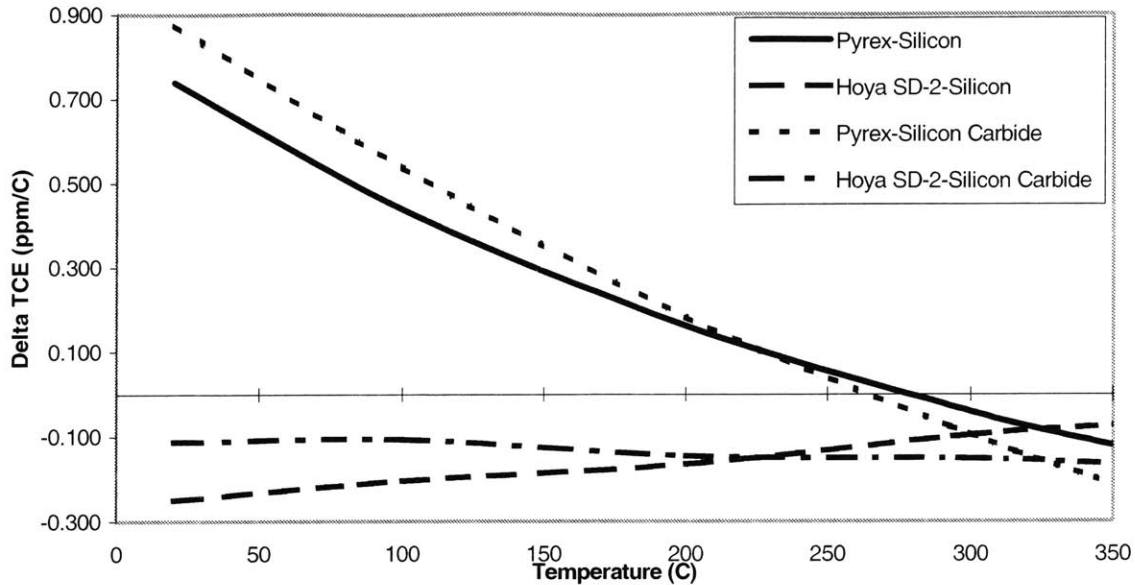
Figure 3-1: Effective Delta TCE of Glass to Si and CVD SiC as a function of temperature.
$(TCE_{glass} - TCE_{Si/SiC})$ [28][12,13,14]

3.2 Plaza Test Mask Deformation Model

The pull-down mechanism of the Plaza Test structure is defined in two ways. The first, necessary mechanism is the elastic deformation of the Si and the glass substrate in order to overcome the etch depth. A side view of the Plaza Test structure array and etch profile is shown in Figure 3-2. Once both materials are in contact, the second mechanism is the diffusion of oxygen anions towards the Si to form an SiO_2 bond. Figure 3-3 shows bonded structures after the anodic bonding operation. This mechanism is also assumed to occur when bonding with CVD SiC. Once the materials elastically deform and come into contact, diffusion of oxygen into the SiC lattice occurs to form SiO_2 with the available Si.

---

[12] Morton Advanced Materials, CVD Silicon Carbide, MA, USA
[13] Pyrex Data Sheet, downloaded from the Corning, Inc.
<http://www.corning.com/lightingmaterials/products/index_pyrex.html> accessed August 6, 2002
[14] Hoya Corporation, Glass Substrates for Silicon Sensors, CA, USA
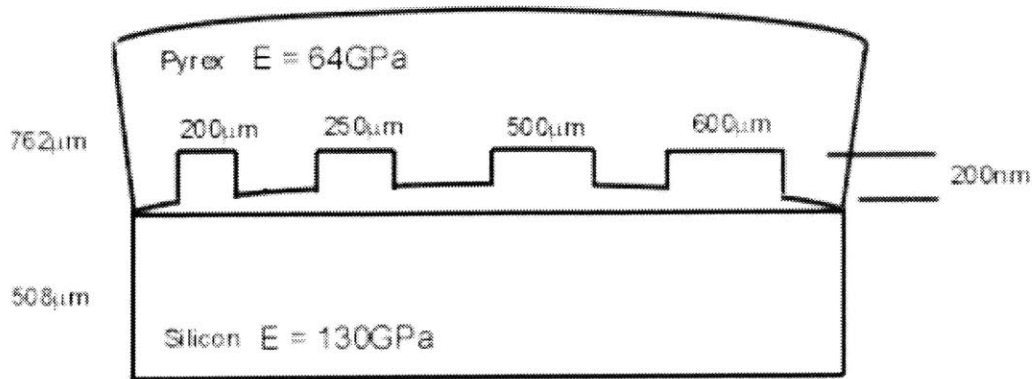
Figure 3-2: Schematic of the Pre-Anodic Bond of Die Size Sample
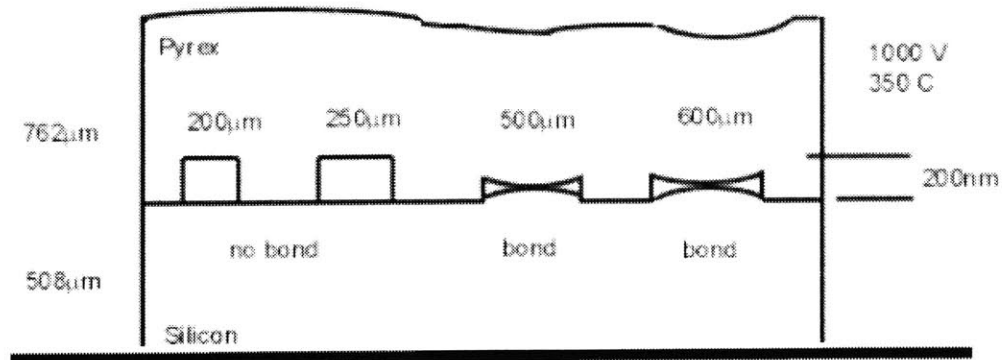
Figure 3-3: Schematic of the Post- Anodic Bond of Die Size Sample

An individual Plaza Test structure is shown in Figure 3-4. The dimensions shown in this figure are defined as the height of the glass (H_1)=762 µm, the height of the Si (H_2)=508 µm and SiC (H_2)=470 µm, the total variable width of the etched structure (W_t)=600 to 20 µm, the overall width of the structure (W_o)=1600 µm to 1020 µm, and the length of the structure (L)= 8500 µm. The etch depth, g_o, in the glass is either 0.2 or 0.4 µm. Figure 3-5, a top view of the Plaza Test Mask array, shows the distance of 500 µm between each Plaza Test structure. The similar magnitudes of W_o, H_1, and H_2 imply that the structure must be modeled explicitly as three dimensional and cannot be approximated as a beam or a plate. The ANSYSv.6.0 finite element analysis (FEA) package was used to perform the modeling analysis. Due to the thickness of the structure in the z direction, 8-node plane strain deformation was assumed in the modeling. Two-dimensional modeling was used. Elastic material behavior was assumed throughout.
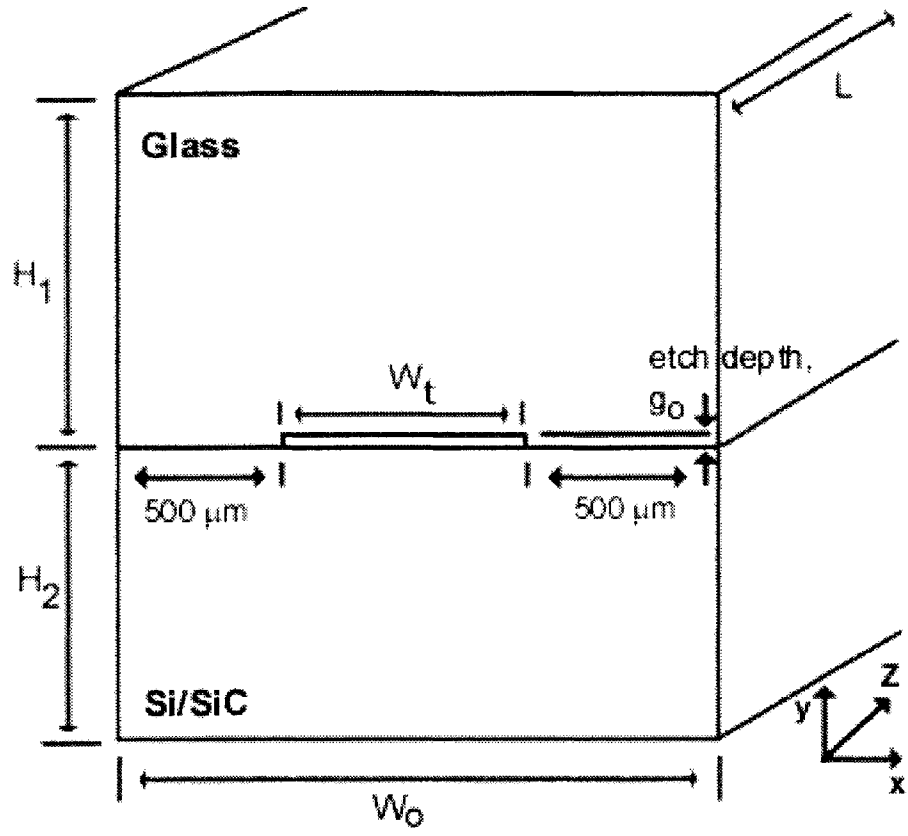
Figure 3-4: Side View of Structure Modeled
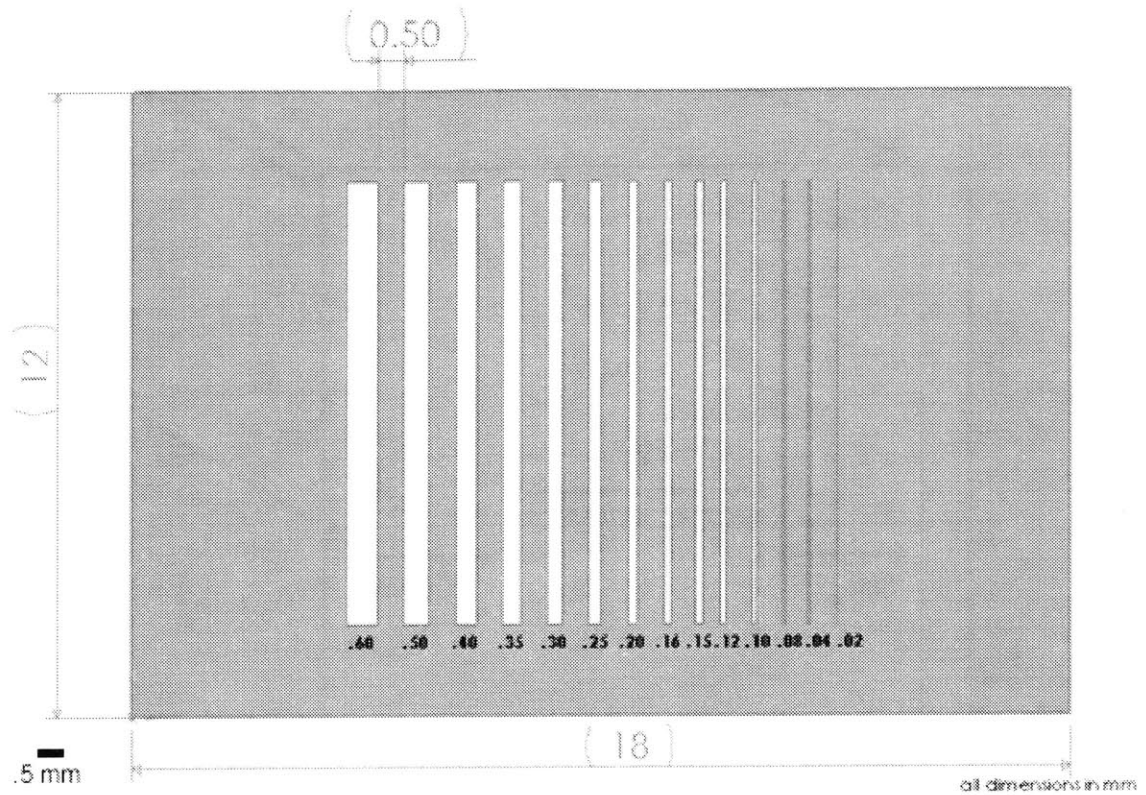
Figure 3-5: Top View of Plaza Test Mask Array in Glass

3.3 Two-Part Bond Model

The following analysis describes the two-part bonding model of the Plaza Test structures. The overall model requires elastic deformation as the principal mechanism to adhere the surfaces. The first part occurs when the applied voltage brings the two surfaces into contact. The second part occurs, when interdiffusion and chemical bonding (SiO_2) form a permanent bond. The structures remain permanently bonded when the bond strength exceeds the elastic restoring force, or in a fracture mechanics approach, the bond toughness exceeds the strain energy release rate.

Figure 3-6 shows a simple diagram which displays the forces involved when the materials contact and when they bond. The spring force represents the elastic response of the surrounding material that resists bonding, the electrostatic force represents the voltage-induced force during bonding, and the bond force represents the bond strength after bonding.
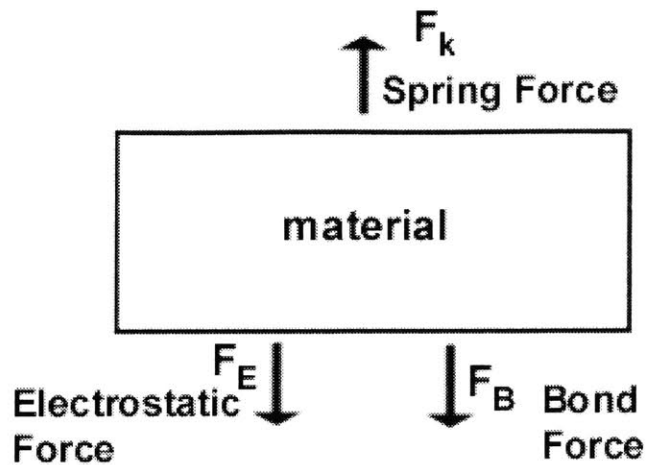
Figure 3-6: Force Diagram

Figure 3-7 shows the contacting of the material surfaces. At equilibrium, when the net force is equal to zero, the point of contact occurs when the electrostatic force equals the opposing spring force. A parallel plate capacitor pull-in model predicts which structures contact when the voltage is applied.
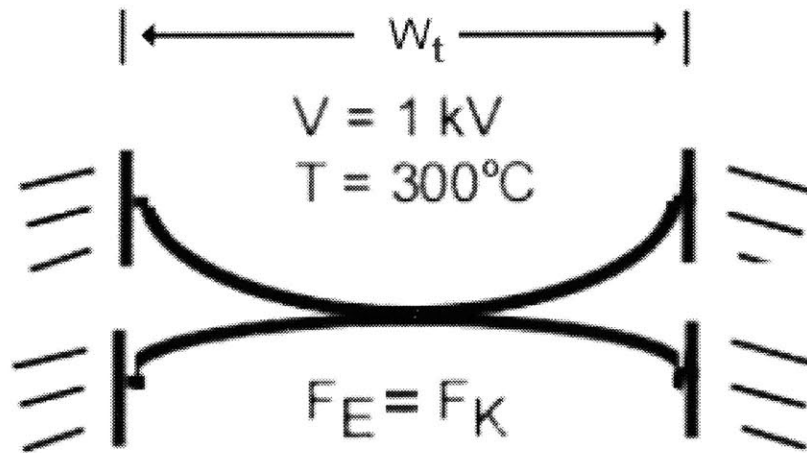
Figure 3-7: Surface Contact

Figure 3-8 shows the permanent bonding of the surfaces when the voltage is off. At equilibrium, when the net force is equal to zero, the point of bonding occurs when the bond strength equals the elastic restoring force. Linear elastic fracture mechanics is used to predict whether the two surfaces remain bonded, given a certain toughness of the interface.

W_t

$V = 0$ V

$T = 23°C$

$F_B = F_K$
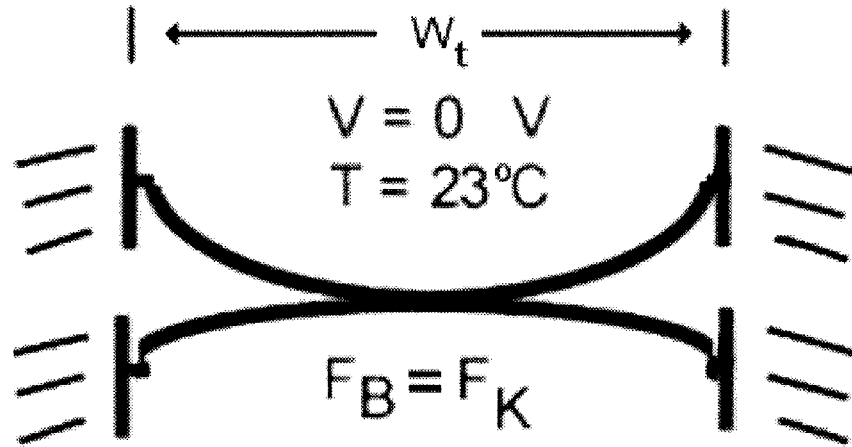
Figure 3-8: Surface Bonding

3.3.1 Contact: Parallel Plate Capacitor Pull-in Model

In order to model the structure contacting mechanism in terms of a parallel plate capacitor, an equivalent stiffness and capacitance are calculated. The parallel plate deforms rigidly in order to pull-in or contact, whereas, the actual structures exhibit a more complex deformation. However, the principal contact mechanism of the structure surfaces is at the middle of the structure width where the deformation is most like a parallel plate. Once the center regions of the two surfaces are in contact, the contact front spreads outward towards the edges.

A double-spring mass structure models the contacting surfaces of the Plaza Test structures. Figure 3-9 shows the difference between a simple parallel plate and the more complex double-spring mass system. This double-spring mass structure is an idealization of a Plaza Test structure. Figure 3-9 shows the spring forces which represent each material of the system: Spring force 1, F_{k1}, is due to the glass and spring force 2, F_{k2}, is due to the Si or CVD SiC. The springs are in series. The electrostatic force is the force caused by the electric field across the gap and pulls the materials to contact. The materials move distances represented as $g_{1,2}$ across the etch depth, g_o.

The stiffness values of the glasses, Si, and CVD SiC are found using ANSYSV.6.0. Since the springs of Figure 3-9 are in series, the equivalent spring stiffness, k_{eq}, is calculated using Equation 3.3 :

$$k_{eq} = \frac{k_1 k_2}{k_1 + k_2}$$

(3.3)

where k_1 is the stiffness constant of the glass and k_2 is the stiffness constant of the Si or CVD SiC.
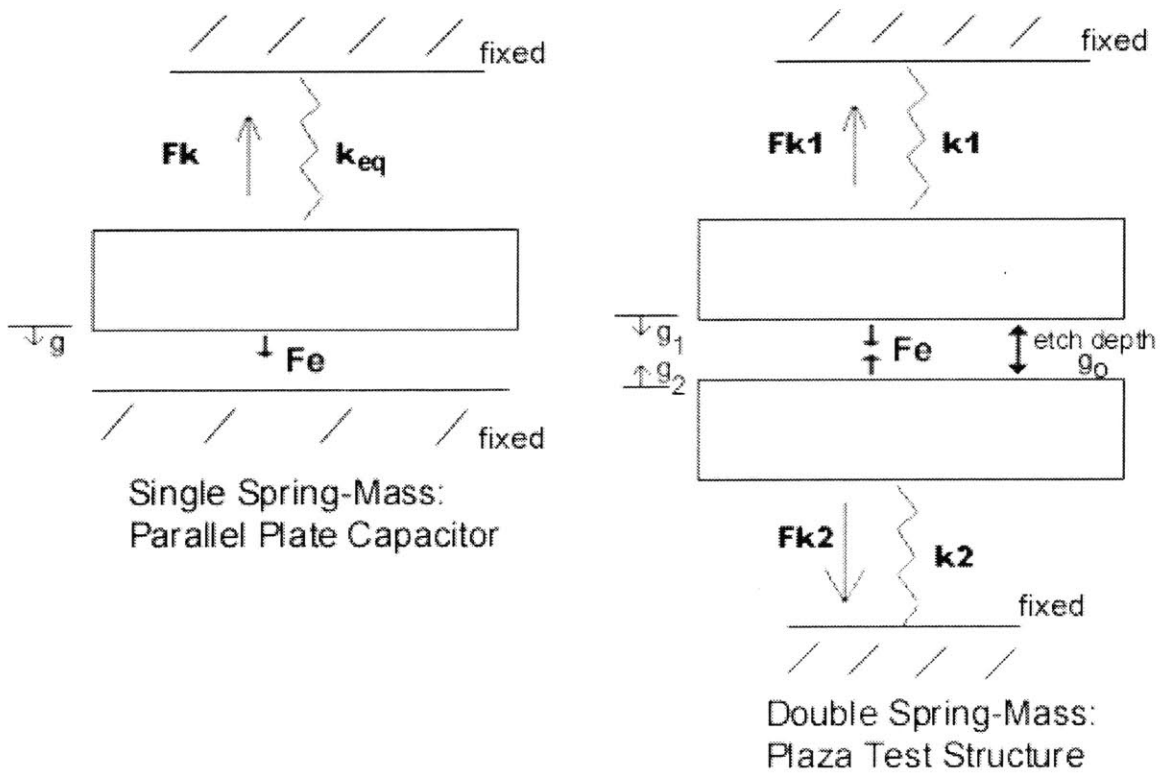
Figure 3-9: Spring-Mass Structures of Parallel Plate [1] and Plaza Test structure

Figure 3-10 shows the dimensions of a bimaterial structure system modeled in ANSYSv.6.0. The x and y directions are assumed to be fixed on each side of the structure. It is assumed that the 500μm surfaces on each side of the etch depth are not fixed, but contact in order to simulate the bonding process. It is also assumed that the top and bottom glass and Si/CVD SiC surfaces without the fixed boundary conditions are traction free. The etch depth is defined as the total variable width, W_t, of each structure. The distance between each Plaza test structure is 500 μm and the etch depth, g_o, in the glass is 0.2 μm. The ANSYSv.6.0 input can be found in Appendix 7.1. The following procedure

describes the ANSYSv6.0 modeling in order to calculate the stiffness, $k_{1,2}$, of each material in the bonded glass to Si system.
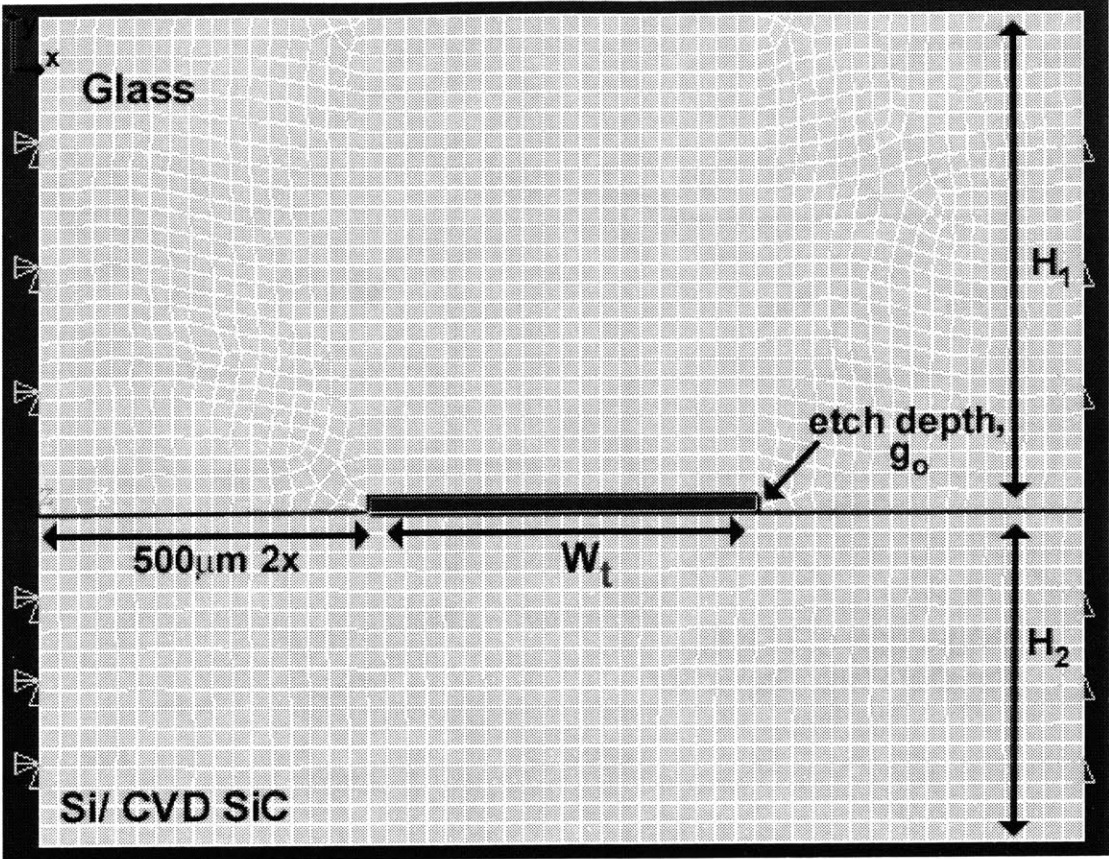
Figure 3-10: Dimensions of Bonded Structure

Similar pressure values are fixed on the nodes of both surfaces: the glass surface in the etched region, and the Si surface on the opposite side. Each surface deforms to a displacement such that the sums of the displacements equals the whole etch depth. Figure 3-11 and Figure 3-12 show the ANSYSv.6.0 output of the two components (not drawn to scale and shown separately for clarity) of Figure 3-10. Figure 3-11 shows the deflection contour maps of Pyrex[TM] glass, and Figure 3-12 shows the corresponding deflection of the Si. Each material deforms a peak distance, i.e. Pyrex[TM] deforms 116nm in Figure 3-11 and Si deforms 84nm in Figure 3-12. Once the total central displacements of each surface, 116nm+84nm, equals the etch depth, 200nm, the force is calculated from the pressure. Different pressure values are used to calculate a

delta force divided by a delta central displacement of each material in order to obtain each material's k constant. The same program is used to model the bonding of glass with CVD SiC.
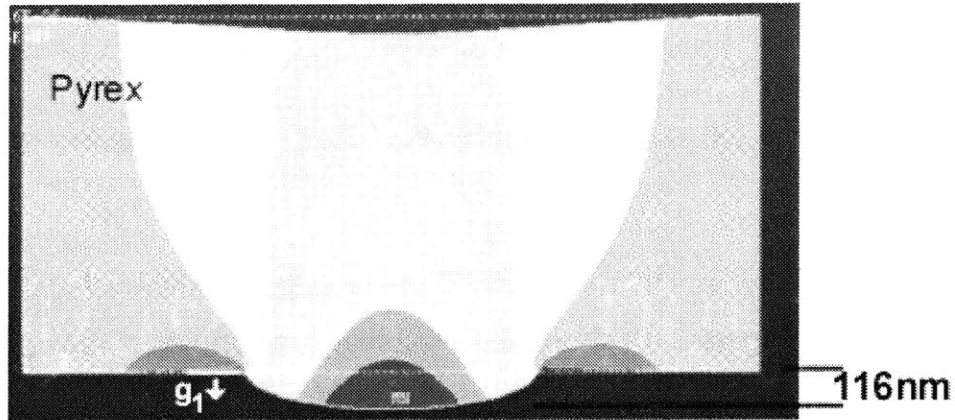
Figure 3-11: Pyrex™ Glass Deformation
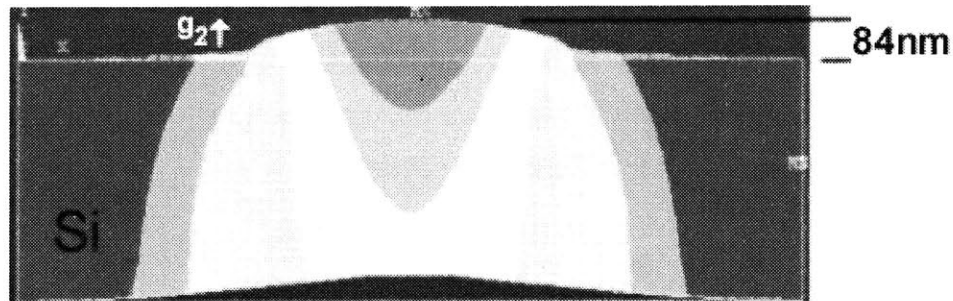
Figure 3-12: Silicon Deformation

Similar pressures are applied to the material interfaces at the etch depth. Each force from an applied pressure is found using:

$$F = PA$$
(3.4)

where the area is equal to the variable width of the structure and the length of the etched structure, 8.5 mm. Once each force, F, is calculated, the stiffness constant, k, is found using:

$$k_{1,2} = \frac{\Delta F}{\Delta g}$$
(3.5)

where Δg is the difference in peak displacement of each material from the ANSYSV.6.0 calculation at a particular force, F.

Once the $k_{1,2}$ constants and k_{eq} are calculated, the Plaza Test structure system is equated to a parallel plate capacitor (Figure 3-9) with a the spring force [1]:

$$F_k = k_{eq}(g_0 - g)$$ (3.6)

where g_o is the etch depth at zero applied voltage, and g is the displacement of the materials.

Next, the structure is related to the parallel plate capacitor, and the electrostatic force is calculated. Figure 3-13 shows the electrical components of the sample compared to a parallel plate capacitor. The electrical components of the sample are defined: R_1 is the glass resistance, R_2 is the Si resistance, C_1 is the depletion layer capacitance of the glass, and C_2 is the capacitance of the etched gap. The anodic bond sample has two capacitors, C_1 and C_2, in series and two resistors, R_1 and R_2. An equivalent capacitor must be found in order to model the anodic bonding circuit as a parallel plate capacitor.
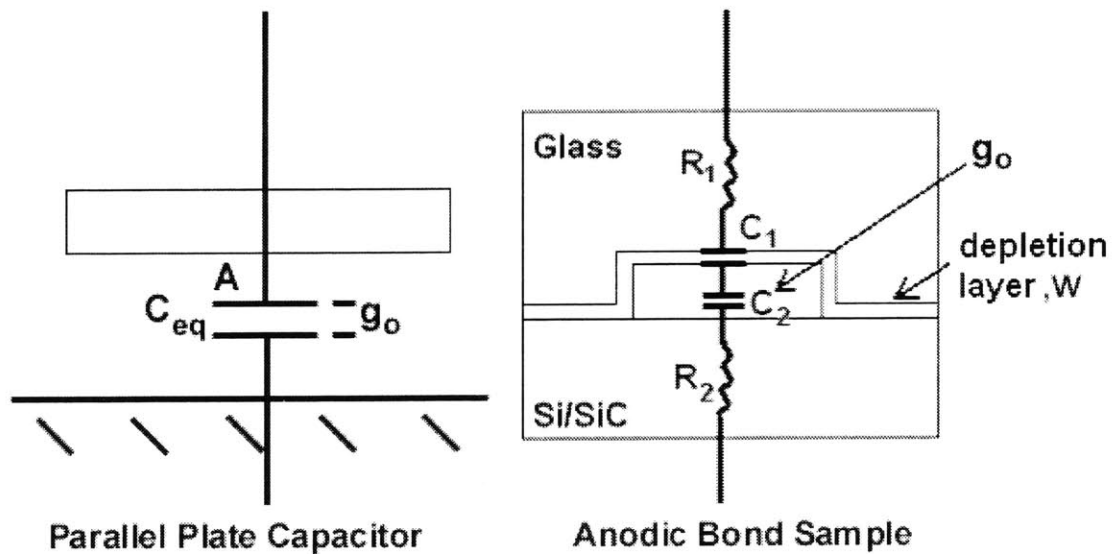
Figure 3-13: Parallel Plate Capacitor [1] versus Anodic Bond Sample

Thus, C_1, the capacitance of the depletion layer, is found using:

$$C_1 = \frac{\varepsilon_o \varepsilon_{Pyrex} A}{w} \tag{3.7}$$

where ε_o is the permittivity of free space, 8.85 e-12 C/ V m, ε_{Pyrex} is the dielectric constant for Pyrex[TM] glass, 10 C/ V m [29], A is area of the depletion layer, and w is the thickness of the depletion layer. The depletion layer thickness, w, varies according to the applied bonding conditions. Figure 3-14 shows a graph of the sodium depletion layer thickness versus bonding time of the Tempax[TM] glass (which has a similar composition to Pyrex[TM]) [6]. The bonding temperature and time increase as does the depletion layer thickness. Figure 3-14 indicates that using a voltage of 250V, bonding temperatures of 210-280°C, and a bonding time of 10 minutes should, at least, produce a sodium depletion layer of 0.7μm [6]. It is assumed that using higher temperatures of 300-350°C and voltages of 500V and 1kV, and a bonding time of 10 minutes, the depletion layer will be greater than 0.7μm and closer to 1μm. The sodium depletion layer thickness and dielectric constant are also assumed to be similar for Hoya SD-2[TM] glass.
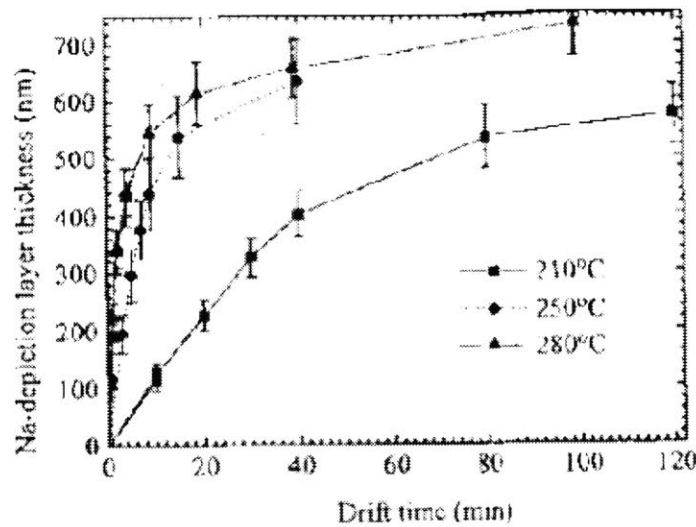
Figure 3-14: Sodium depletion layer thickness in Tempax as a function of the drift time at various temperatures and drift voltage of 250V [6]

C_2, the capacitance of the etched gap, is found using:

$$C_2 = \frac{\varepsilon_o A}{g_o} \tag{3.8}$$

where A and ε_o are equal to the values in Eqn. 3.7, and g_o is the etch depth of 0.2 µm.

The equivalent capacitance, C_{eq}, is found and equated to C_2 using the following assumptions. Since the variables, A and ε_o are equivalent in Eqns. 3.6 and 3.7, the difference between C_1 and C_2 is $C_1 = 10/w$ and $C_2 = 1/g_o$. The depletion layer thickness, w, varies from 0.2 µm to approximately 1µm, and g_o of Equation 3.8 is approximately 0.2 µm. Therefore, C_1 to C_2 is $C_1 \cong 2 \rightarrow 10\ C_2$. When substituting this relation in Equation 3.9, the equivalent capacitor, C_{eq}, is approximately equal to C_2:

$$C_{eq} = \frac{C_1 C_2}{C_1 + C_2} = \frac{2}{3} \rightarrow \frac{10}{11} C_2 \cong C_2 \tag{3.9}$$

Since C_{eq} is equal to the capacitance of the etch depth or gap between the materials, the double spring mass system is comparable to the parallel plate capacitance. Therefore, the anodic bond sample can be modeled using a single capacitor, and the electric force or pressure established at the interface by the pull-in voltage can be derived. The following section presents the derivation of the electrostatic force and pull-in voltage.

The anodic bonding mechanism is related to a parallel plate capacitor that is charged using a voltage source. There is work done on the system represented by potential energy, W, when the parallel plates move a distance, g. The potential energy is defined as the force between the parallel plates, F, which is created by the charges, +Q and –Q, multiplied by the distance the plates move, g. This parallel plate system is modeled using a two-port capacitor, shown in Figure 3-15, since the potential energy is a function of two variables: an electrical variable, charge, Q, and a mechanical variable, displacement, g [1].
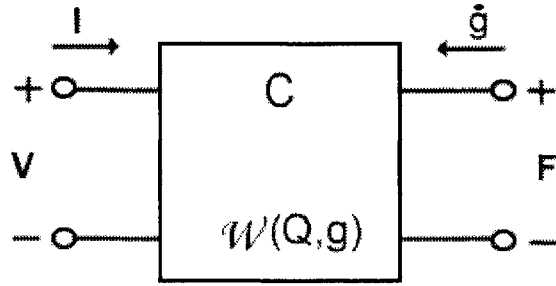
Figure 3-15: Two-port Voltage Controlled Capacitor [1]

The two-port capacitive system represents an electrostatic actuator by attaching the movable plate to a spring. The distance the spring, k, moves is defined as z. This voltage controlled, electrostatic actuator is modeled in Figure 3-16.
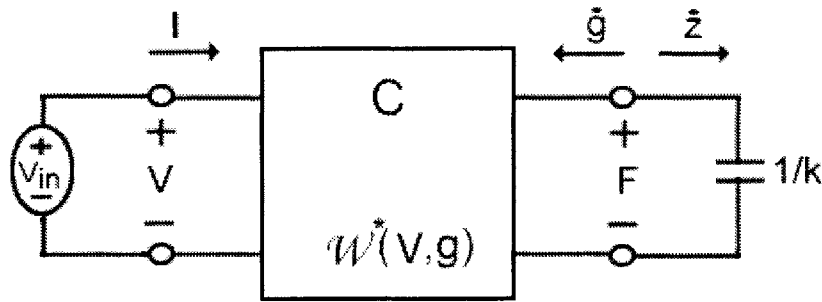
Figure 3-16: Voltage Controlled Electrostatic Actuator [1]

The electrical co-energy, W^*, defines the system because controlling the voltage does not have an effect on controlling the charge [1]. Therefore, the parallel plate capacitor is a non-linear element. Equation 3.10 is the co-energy of the system defined in mechanical and electrical terms using V as the voltage found across the capacitor, and g as the distance the parallel plate moves [1].

$$W^*(V,g) = QV - W(Q,g) \tag{3.10}$$

Taking the derivative of the co-energy differential equation, Equation 3.11, shows how it is related to both mechanical and electrical systems [1].

$$dW^*(V,g) = QdV - Fdg \tag{3.11}$$

Equation 3.11 is differentiated to find the electrostatic force, F_e defined in Equation 3.12.

$$F_e = -\frac{\partial W^*(V,g)}{\partial g}\bigg|_V = -\left[-\frac{\varepsilon A V^2}{2g^2}\right] = \frac{\varepsilon A V^2}{2g^2} \tag{3.12}$$

where A is the area of the variable structure width and the structure length, 8.5mm. F_e is a function of the equivalent capacitance:

$$F_e = \frac{\varepsilon A V^2}{2g^2} = C_{eq}\frac{V^2}{2} \tag{3.13}$$

Equation 3.12 can be arranged to find the electrostatic pressure, P_e shown in Equation 3.14. Plaza et al. [10] related the P_e defined in Equation 3.12 to the bonding or unbonding of the Plaza Test structures. Equation 3.14 shows the displacement of the parallel plate, g, and the voltage between the plate, V, are functions of the electrostatic pressure that pulls the plates together.

$$P_e = \frac{F}{A} = \frac{\varepsilon V^2}{2g^2} \tag{3.14}$$

Since both F_k and F_e have been derived, the net force on the upper plate is:

$$F_{net} = -F_e + F_k \tag{3.15}$$

The pull-in voltage, V_{pi}, calculated to model the Plaza Test surface contact, is the voltage when the stability of static equilibrium is lost, and the materials contact each other. The derivative of Eqn. 3.15 with respect to g is taken at equilibrium, F_{net} = zero. Eqns. 3.6, 3.12, and 3.15 are combined, to examine how F_{net} varies with a change in gap, g + δg. The pull-in voltage is derived to be:

$$V_{pi} = \sqrt{\frac{K_{eq}\, g_o^3}{\varepsilon A}} \tag{3.16}$$

The pull-in voltage, V_{pi}, and etch depth, g_o, of Eqn. 3.16 are normalized before graphing the electrostatic force against the spring force: the applied voltage, $V_{applied}$, to V_{pi}, and the change in displacement, g, of the plate to its original position, g_o. Eqns. 3.17 and 3.18 show this normalization.

$$V_n = \frac{V_{applied}}{V_{pi}} \qquad (3.17)$$

$$\zeta = 1 - \frac{g}{g_o} \qquad (3.18)$$

After this normalization, the spring and electrostatic forces are plotted using Equation 3.19. The left side of Equation 3.19 is related to the normalized electrostatic force, and the right side is related to the normalized spring force. Both sides of the equation are plotted in order to find when the electrostatic force is larger than the spring force indicating contact between the surfaces.

$$\frac{1}{2} \frac{V_n^2}{(1 - \zeta)^2} = \zeta \qquad (3.19)$$

3.3.2 Bonding: Linear Elastic Fracture Mechanics (LEFM) Modeling

The purpose of the modeling presented in this section is to determine the strain energy that must be supplied to bring the surfaces into contact. LEFM and ANSYSv.6.0 modeling is used to predict the energy release rate of each structure width. This strain energy can then be equated to the bonding energy after SiO_2 bond formation in order to determine whether the surfaces remain bonded. The surfaces of a structure at a particular width remain bonded when the toughness or work of adhesion, which is a function of the bonding conditions, exceeds the energy release rate. The actual toughness of the structures is determined experimentally.

Modeling the whole Plaza Test structure is arduous and time consuming, so a simple, symmetric model is used. Figure 3-17 shows the 2-D dimensions for half of the structure shown in Figure 3-4. The same heights and etch depths are $H_1=$ 762 μm, $H_2=$ 508 μm, and g_o=0.2 or 0.4 μm. Now, W is half of the total variable width, W_t, so W = 300 to 10 μm.
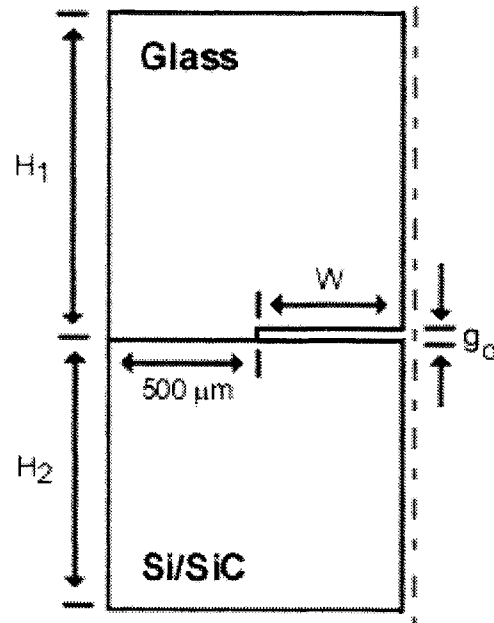
Figure 3-17: Symmetric Front of Structure

The bonding of two materials together is modeled as a crack closing. It is assumed that mode 1 fracture (the bonding process when the surfaces coming together at matched displacements are parallel to the crack plane) is the dominant mode. The bonding begins in the middle of the structure and extends to the side. Half of the bonded interface of glass to Si is shown in Figure 3-18 where B is the bond width, a is the crack length, and L is the length of the structure.
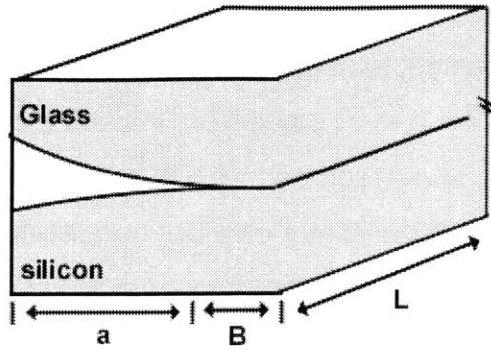
Figure 3-18: Crack Closing Dimensions

The energy release rate, G, defined in Equation 3.20 [30], is the rate of change in potential energy, W_p, as the bond area, dA, increases.

$$G = \frac{dW_p}{dA}$$ (3.20)

The change in potential energy, W_p, is defined in Equation 3.21 [30].

$$W_p = U - W_f$$ (3.21)

where U is the stored elastic strain energy, and W_f is the work done by external forces. Since this bonding system under consideration is displacement controlled, the work done by external forces, W_f, is zero. The position of the nodes along the interface of the materials is fixed and the forces are allowed to slowly bring the materials together. Therefore, in this bonding system, the strain energy release rate, G, is the rate of change of strain energy with increase in bond area:

$$G = \frac{dU}{dA}$$ (3.22)

where dA is defined as the area of the bond width, B, and length of the structure, L, and dU is the change in strain energy.

The total strain energy of the system is modeled using ANSYSv.6.0 in order to calculate the strain energy release rate. A symmetric 2-D model of the rectangular structure is built. The dimensions of the model are shown in Figure

3-17 and Figure 3-19. The boundary conditions are established. The left side is bounded by zero displacement in both the x and y directions. It is assumed that the right side is bounded by zero displacement in the x direction since it is a symmetric structure. It is also assumed that the top and bottom glass and Si/CVD SiC surfaces without the fixed boundary conditions are traction free. Nodes are established on the material surfaces along the interface.
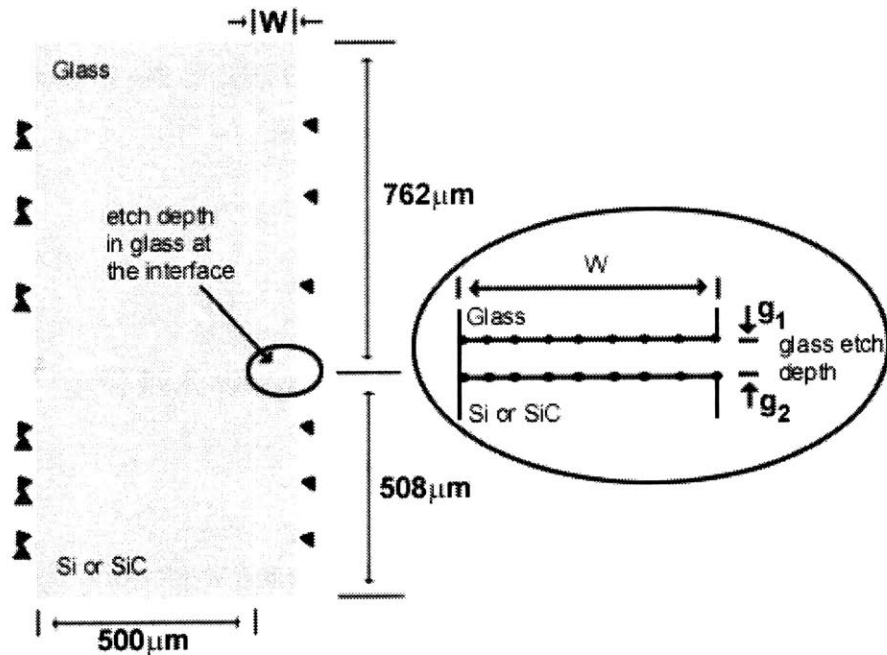
Figure 3-19: Symmetric ANSYS Model of Structure

An ANSYSv.6.0 input, listed in Appendix 7.1, was developed to pull down the nodes along the interfaces at different distances adding up to the total etch depth, g_o, ie. 0.2 μm. The glass is pulled a distance of g_1, and the Si or CVD SiC is pulled a distance of g_2 where $g_1 + g_2 = g_o$. Initially, the two center nodes on each material interface are pulled together, as shown in Figure 3-20, because of the singularity associated with only one pulled node on each interface. The strain energies, U, of all the elements are imported into Microsoft Excel[TM] and summed in order to find the total strain energy of the system for that particular deformed material distances. The process of pulling down a two pairs of nodes (on each surface) different distances, and the summation of the strain energy is repeated iteratively until the minimum energy configuration of the displaced

surfaces is obtained. Once the minimum strain energy, U_{min}, is found, the next three pairs of nodes (on each surface) are pulled down which includes the first two nodes and a third node on both interfaces. This continues on from the middle of the structure to the edges. The crack length, a, in Figure 3-20, corresponds to the unbonded part of the interface where the nodes are not pulled together. At a=0, the crack length is zero because the width, W, is totally bonded and all the nodes are pulled together.
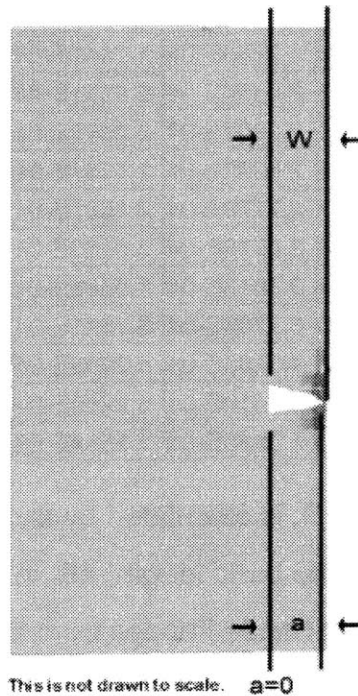
Figure 3-20: Two Deformed Interface Nodes (Not drawn to Scale)

Table 4 shows, in bold, the minimum U, U_{min}, found by pulling down the nodes different distances to a total etch depth of 0.2 µm on a W=300µm (symmetric for a 600µm width structure) Pyrex^{TM} and Si system.

Table 4: Minimum Strain Energies as a Function of Deformation

W = 300μm Symmetric for W_t= 600μm width (25 micron interface node spacing)				
Deformation Distance of Nodes (um)				
Pyrex^{TM} nodes, g_1	0.130	0.125	0.118	0.100
Si nodes, g_2	0.070	0.075	0.082	0.100
Finding Minimum Strain Energy, U_{min} (J)				
# nodes pulled				
2 (start bond)	1.4595E-04	**1.4557E-04**	1.4669E-04	1.5279E-04
3	1.7730E-04	**1.7657E-04**	1.7745E-04	1.8335E-04
4	2.0357E-04	**2.0251E-04**	2.0315E-04	2.0871E-04
5	2.2801E-04	**2.2665E-04**	2.2705E-04	2.3221E-04
6	2.5232E-04	**2.5067E-04**	2.5085E-04	2.5561E-04
7	2.7779E-04	2.7587E-04	**2.7584E-04**	2.8021E-04
8	3.0579E-04	3.0360E-04	**3.0338E-04**	3.0737E-04
9	3.3813E-04	3.3568E-04	**3.3530E-04**	3.3894E-04
10	3.7796E-04	3.7525E-04	**3.7476E-04**	3.7804E-04
11	4.3233E-04	4.2936E-04	**4.2881E-04**	4.3173E-04
12	5.2610E-04	5.2286E-04	**5.2241E-04**	5.2482E-04
13 (full bond)	1.3598E-03	**1.3564E-03**	1.3592E-03	1.3587E-03

The strain energy release rate, G, is calculated by dividing the difference in strain energy, ΔU, in units of J/m, by the bond length, ΔB, in units of meters, m. ΔU is found by subtracting U_{min} of two bonded nodes from three bonded nodes etc. in Table 4. The values of ΔU are put into Table 5 for further calculation of G. ΔB is the change in bond length of the nodes pulled together for that particular ΔU, i.e. if two nodes at 25μm apart on each interface are pulled, ΔB equals a bonded distance of 50μm. Crack length, a, of Figure 3-20 is found by subtracting ΔB from the width, W=300 μm. The crack length does not have to be multiplied by the structure length, 8.5 mm, because this 2D plot has strain energies that have a strain energy ,U, per unit thickness or length, L, of the structure. It is normalized by dividing a, by W. This is used to plot G vs. a normalized crack length, a/W, so all the different widths can be plotted on the same graph. Table 5 shows the final calculation of the strain energy release rate, G.

Table 5: Final Calculation of G, Energy Release Rate

# nodes pulled	U Strain Energy	Δ U	Δ B bond length	a crack length	a/W	G
	(J)	(Δ J)	(m)	(m)	W=300μm	(J/m²)
2	1.4557E-04					
3	1.77E-04	3.10E-05	5.00E-05	2.50E-04	0.833	0.620
4	2.03E-04	2.59E-05	7.50E-05	2.25E-04	0.750	0.346
5	2.27E-04	2.41E-05	1.00E-04	2.00E-04	0.667	0.241
6	2.51E-04	2.40E-05	1.25E-04	1.75E-04	0.583	0.192
7	2.76E-04	2.52E-05	1.50E-04	1.50E-04	0.500	0.168
8	3.03E-04	2.75E-05	1.75E-04	1.25E-04	0.417	0.157
9	3.35E-04	3.19E-05	2.00E-04	1.00E-04	0.333	0.160
10	3.75E-04	3.95E-05	2.25E-04	7.50E-05	0.250	0.175
11	4.29E-04	5.41E-05	2.50E-04	5.00E-05	0.167	0.216
12	5.22E-04	9.36E-05	2.75E-04	2.50E-05	0.083	0.340
13	1.36E-03	8.34E-04	3.00E-04	0.00E+00	0	2.780

Figure 3-21 shows the plot of G versus normalized crack length, a/W. These are values for G as the bond forms along the interface. At a/W = 0, there is a full bond and no crack. As a/W > 0, the crack length increases and the bond area decreases. At a/W = 0, G, is at its highest value and as a/W increases the structure becomes more compliant, so G decreases. There is a distinct minimum in the G versus a/W response. Initially at a/W = 1, the structure begins to bond. At this point a crack can easily debond the structure. It becomes harder to debond as G decreases to a minimum around a/W = 0.5. It slowly begins to become easier to debond again as a/W < 0.5. At a/W = 0, the structure is fully bonded and a crack can easily debond it because the driving force, G, is high. The value of G at this point should tend to be an infinitely large value since it is at the edge of the structure and very rigid, but the mesh is not sufficiently fine in that area to accurately capture this behavior. It is not understood why G begins to increase again when a/W> 0.5, but an obvious reason could be that this is not a simple beam or plate model.
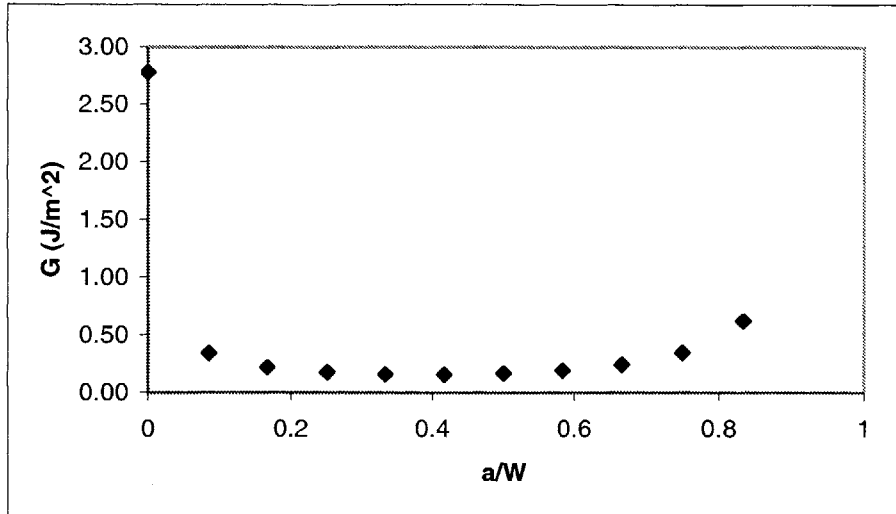
Figure 3-21: G versus Crack Length for 600μm Structure

For each part of the experiment, an arbitrary number of the bonded widths were modeled and plotted on the same graph. Figure 3-22 shows a magnified view of the increasing G trend as W decreases. As W decreases, the structure's stiffness increases resulting in bonds that are easier to crack.
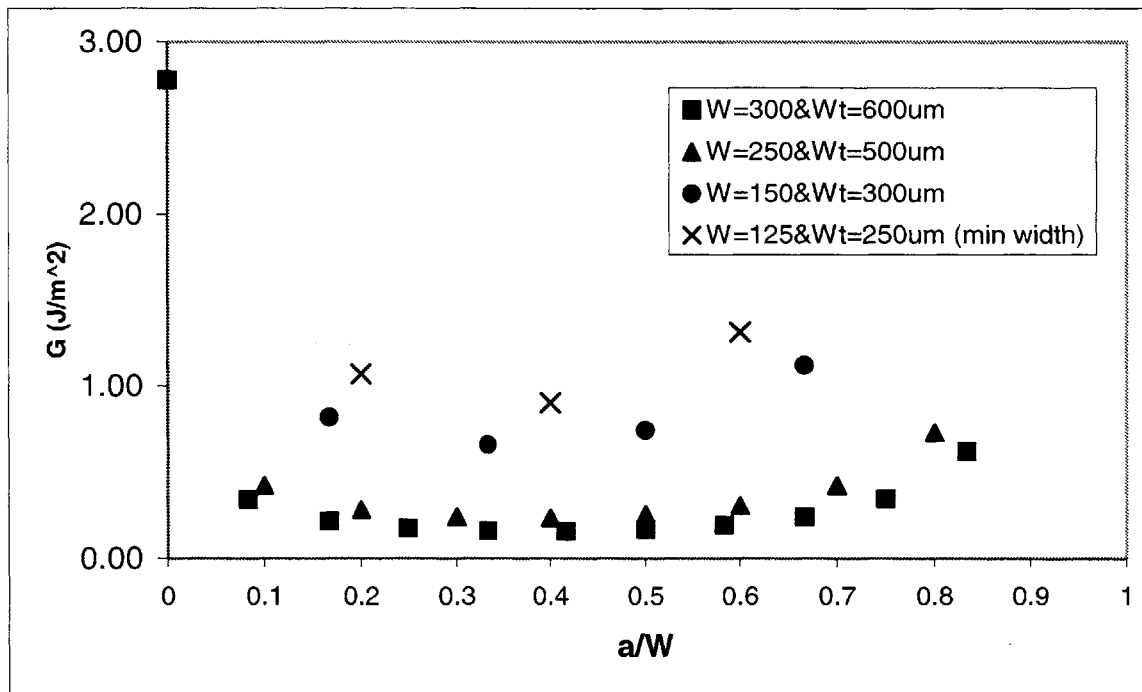
Figure 3-22: G as a Function of W

Each structure bonds at a minimum G, G_{min}. G_{min} defines the overall toughness or work of adhesion of the bonded structures on the Plaza Test Mask sample.

Once all the bonded structures are plotted, G_{min} is found experimentally by measuring the unbonded length on each structure using an optical microscope and its measurement grid. Figure 3-23 shows the area modeled, and the thin white line around it signifies the unbonded part of the structure defined as the crack length, a. Figure 3-23 is an acoustic microscopy image using a Sonoscan[TM] microscope of the top view of a 600μm width structure. This figure also shows a magnified top view of the crack length where W is the structure width, and a is the crack length. A schematic of a side view is also shown in Figure 3-23 for better viewing of the crack length, a, and variable width, W.
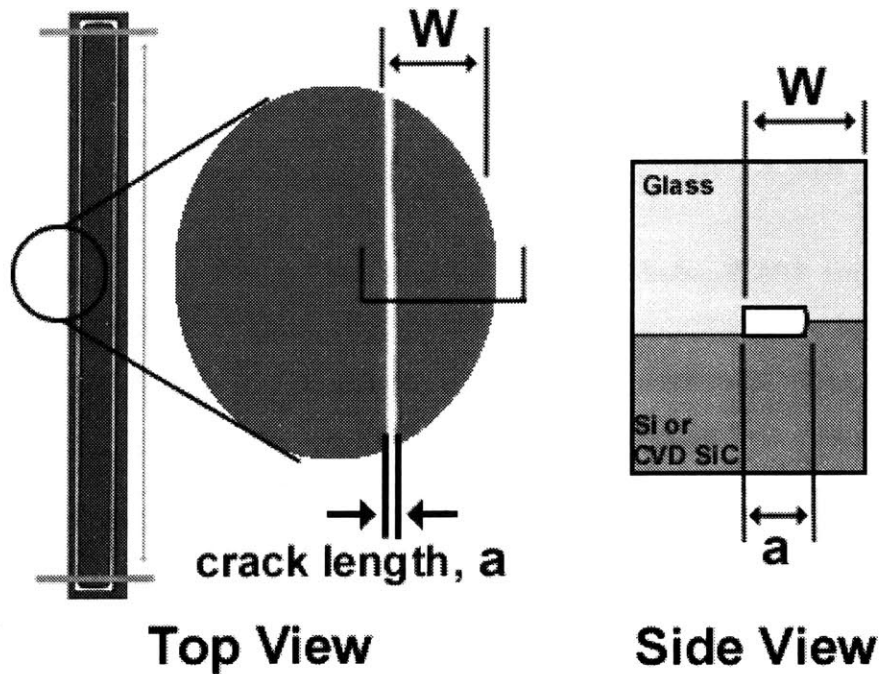
Figure 3-23: Acoustic Microscopy Image of Crack Length and Total Area Modeled

The unbonded length or crack length was found, divided by the width of the structure, W, and then plotted on the a/W x-axis of Figure 3-22 in order to find the approximate minimum strain energy release rate, G_{min}. The crack length value on the x-axis was used to find the approximate G_{min} value by drawing an arrow up from the measured crack length to the curve corresponding to the width being measured. The black arrows of Figure 3-24 indicate the positions of the bond front and its corresponding G_{min} for each structure's width. Since bond toughness is a function of the bonding conditions, each structure on the Plaza

Test Mask sample has a constant G_{min} value indicating the overall anodic bond toughness of a particular experiment.
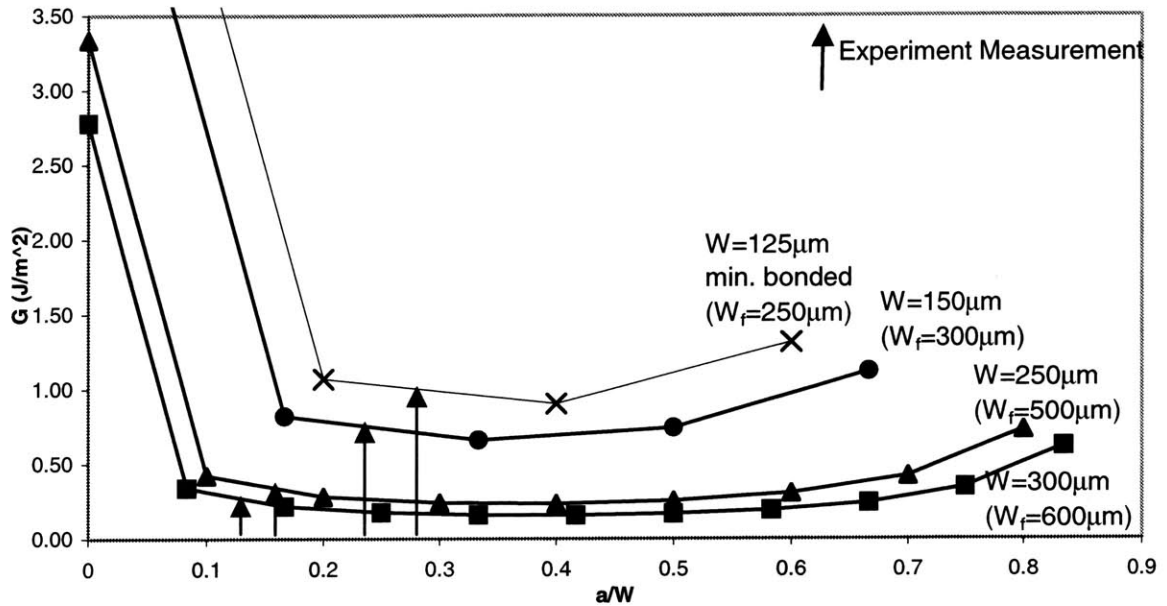
Figure 3-24: Bonded Structures and their Corresponding Minimum G

The bimaterial stress intensity factor, K, or fracture toughness values are calculated in order to compare to literature results. K and G_{min} are related in the following analysis and a crucial assumption [31].

The calculation of the stress intensity factor, K, assumes the materials are linearly elastic, homogeneous, and isotropic above and below the actual interface, and the overall system deformation is plane strain. Wan and Suo [31] take these assumptions, summarize interfacial fracture mechanics, and find an Irwin-type relation for K and G_{min}.

$$G_{min} = \frac{\left| K^2 \right|}{E^* \cosh^2 \pi\varepsilon} \tag{3.23}$$

E^* is found using Equation 3.24 where both $\bar{E}_1$ and $\bar{E}_2$ are the plane strain tensile modulus for each material:

$$\frac{2}{E^*} = \frac{1}{\overline{E}_1} + \frac{1}{\overline{E}_2}$$

(3.24)

The plane strain tensile modulus is:

$$\overline{E} = \frac{2\mu}{1 - \upsilon}$$

(3.25)

where μ is the shear modulus and υ is the Poisson's ratio.

Equation 3.26 is used to find ε of Equation 3.23. The oscillatory index, ε, takes into account different pathological behaviors in linear elasticity solutions for interfacial cracks:

$$\varepsilon = \frac{1}{2\pi} \ln \frac{1 - \beta}{1 + \beta}$$

(3.26)

A Dundurs elastic mismatch parameter defines β in Equation 3.27:

$$\beta = \frac{1}{2} \frac{(1 - 2\upsilon_2)/\mu_2 - (1 - 2\upsilon_1)/\mu_1}{(1 - \upsilon_2)/\mu_2 + (1 - \upsilon_1)/\mu_1}$$

(3.27)

where μ_1 and μ_2 are the shear moduli of each material and υ_1 and υ_2 are the Poisson's ratios of each material.

Rearranging Equation 3.23 in order to determine K is shown in Equation 3.28:

$$K = \sqrt{G_{min} E^* \cosh^2 \pi \varepsilon}$$

(3.28)

3.3.3 Flow Diagram of Contact and Bonding

Figure 3-25 shows a flow diagram for the two-part bonding model with inputs of the materials, Plaza Test structure geometry, applied voltage, and work of adhesion. Contact or pull-in is predicted to occur at the point of unstable equilibrium if the electrostatic force, F_e, (established from the applied voltage)

exceeds the elastic spring force, F_k. Since F_e brings the surfaces together, elastic strain energy is stored in the materials keeping them in contact. LEFM and ANSYSv.6.0 modeling were used to determine the strain energy release rate as a function of structure width needed to bring the surfaces into contact. Bonding occurs if the strain energy needed for contact exceeds the bonding energy from the interdiffusion and permanent SiO_2 bond formation processes. The input of a work of adhesion or strain energy release rate is used to predict the toughness of the bonded structures.

Input:
Materials, Plaza Test Structure Geometry, Applied Voltage, Work of Adhesion

Contact: (Figure 3-7)

Double Spring Mass Structure Model: Figure 3-9&10

Find $k_{1,2}$ using ANSYSv.6.0: Eqns.3.4 & 3.5

Find k_{eq}: Eqn. 3.3

Find Spring Force: F_k Eqn. 3.6

Voltage Controlled Model. Anodic Bond Circuit: Figure 3-13

Find C_{eq}: Eqns. 3.6-8

Find Voltage controlled electrostatic force F_{eq}: Eqn. 3.12

Find F_{net}: Eqn. 3.15

Find Pull-In Voltage as a function of k_{eq} and normalize.: Eqn. 3.16-18

Plot Eqn. 3.19: F_k vs. F_e Function of ζ

Surface Contacting

Yes

No

Bond: (Figure 3-8)

Symmetric Bonded Structure: Fig. 3-17

Iterative process of nodal deformation to find U_{min}: Figs. 3-19&20 Table 4

Calculate G: Table 5

Plot G vs. a/W: Fig.3-22

Surface Bonding

Yes

No

Experimentally Find: Toughness Fig. 3-23 & 3-24

Figure 3-25: Contact and Bond Model Flow Chart

3.4 Curvature Calculations

The characterization of residual curvatures developed in MEMS sensor elements, as a consequence of thermal processing during anodic bonding, is the objective of this study. The thermoelastic curvatures are important to analyze in order to understand the magnitudes resulting from the different bonding parameters. In particular, it is desired to understand whether curvature is entirely due to thermal expansion mismatch between the materials being bonded, or whether other process related effects play a role. After bonding, the sample cools down to room temperature. When the sample cools from the bonding temperature to room temperature, a curvature results between the materials because of their thermal mismatch (ΔTCE or $\Delta\alpha$). The curvature was calculated from classical plate theory and ANSYSv.6.0 modeling, and measured experimentally using the Tencor^{TM} machine. Plate theory error bars and Tencor^{TM} measurement scatter were calculated.

The temperatures used during bonding are 300°C and 350°C, which are far below the glass transition, melting, and sublimation temperatures shown in Table 6. Table 6 shows that the glass transition, melting, and sublimation temperatures are higher than the bonding temperatures. According to Ashby, bulk creep occurs at a range of 0.3-0.5 of the melting temperature, T_m [32]. This indicates that creep will occur in Si at a minimum temperature of 426°C (since the melting temperature is 1420°C [33]), which is still higher than the bonding temperatures. Since CVD SiC is a very hard and stiff material with high strength at elevated temperatures, it only experiences sublimation at 2700°C.[15]

---

[15] Morton Advanced Materials, CVD Silicon Carbide, MA, USA

Table 6: Material Temperature Properties [33] [16,17,18]

Material	Glass Transition Temperature (°C)	Melting Temperature (°C)	Sublimation Temperature (°C)
Pyrex[TM]	552	N/A	N/A
Hoya SD-2[TM]	721	N/A	N/A
Si	N/A	1420	N/A
CVD SiC	N/A	N/A	2700

3.4.1 Classical Plate Theory

Classical plate theory, a small deformation analysis, is used in order to study stress and deformations in multi-layered plates. Small deformation elasticity theory is used to determine how the stresses and curvature evolve from the strain mismatch in each layer of the multi-layer systems. In the present case, these bonded specimens are assumed to be bilayer plates with isotropic in-plane elastic properties and a thermoelastic strain mismatch. The layer thickness, the biaxial moduli, thermal coefficients of expansion, and lengths define the material properties and the rectangular geometry of the bilayer shown in Figure 3-26.

The composite plate has uniform thickness and uniform temperature. Initially, the bi-layer is flat without curvature and is stress free at an initial room temperature. Figure 3-27 shows that this bilayer at room temperature is a flat plate without any internal stresses. Once the temperature is increased to the bonding temperature, the bilayer is bonded, and then cooled down again to room temperature. Once this bilayer is bonded, the difference in thermal coefficient of expansion (TCE) produces a bow defining a curvature, shown in , Figure 3-27, because of delta T (ΔT). These calculations are used since the bow resulting from the difference in TCE is related to curvature.

Since L_x and L_y are much larger than the total thickness, [34], i.e.:

---

[16] Morton Advanced Materials, CVD Silicon Carbide, MA, USA
[17] Pyrex Data Sheet, downloaded from the Corning, Inc.
<http://www.corning.com/lightingmaterials/products/index_pyrex.html> accessed August 6, 2002
[18] Hoya Corporation, Glass Substrates for Silicon Sensors, CA, USA

$$(L_x >> h_1 + h_2 \; ; \; L_y >> h_1 + h_2)$$

where Lx and Ly are the lengths in the x and y direction and h_1 and h_2 are the thickness in the top, 1, and bottom, 2, layer, there is a state of equal biaxial stress of the principal stresses and strains in the plate [34].

$$\sigma_{xx} = \sigma_{yy} \text{ and } \varepsilon_{xx} = \varepsilon_{yy}$$
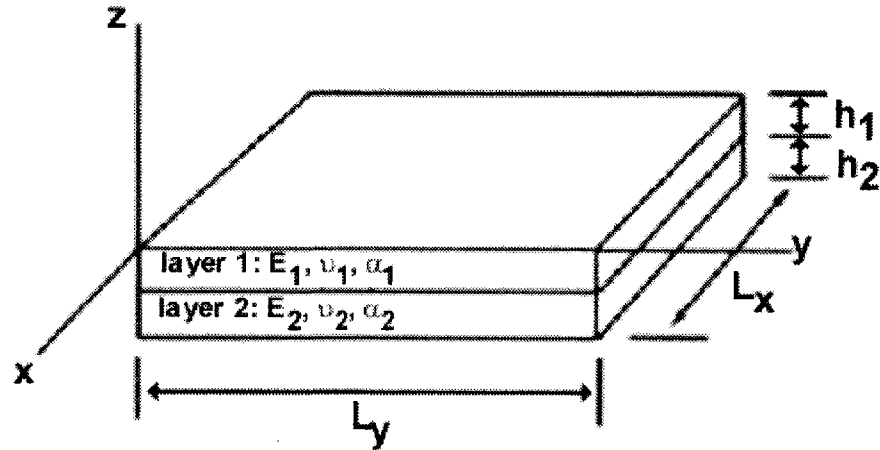
Figure 3-26: Bilayer Geometry [34]
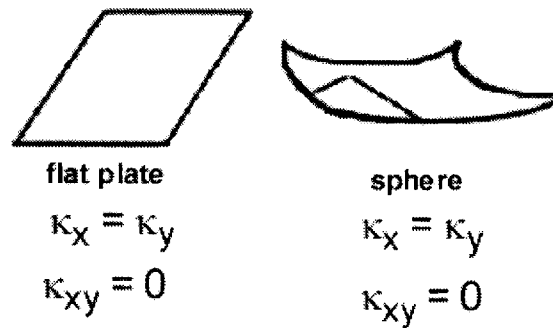
Figure 3-27: Plate Curvature [35]

The entire bilayer (apart from the free edges) exhibits a uniform, biaxial thermoelastic strain. This strain is a result of an in-plane normal strain, ε_o, that comes from the uniform stretch or contraction of the layers, and a strain gradient caused by the curvature, κ, of the layers. Through the thickness of each layer,

the stress variation is linear. There is a maximum stress at the interface, and a difference in stress value between layers.

3.4.2 Curvature Calculation from Classical Plate Theory

The following derivation of curvature from plate theory is found in [34]. The plate theory error bars of this calculation are also included.

Equation 3.29 shows that the total biaxial strain state in the x and y principal directions occurs from ε_o, the uniform expansion or contraction, and kz, as a function of thickness, from bending:

$$\varepsilon_{xx}(z) = \varepsilon_{yy}(z) = \varepsilon(z) = \varepsilon_o + \kappa z \tag{3.29}$$

The biaxial strain contributes to the two principal stresses found in each layer as a function of thickness:

$$\sigma_{xx,1}(z) = \sigma_{yy,1}(z) = \sigma_1(z) = E\_1 \{ \varepsilon(z) - [\alpha_1(z) \Delta T]\} \tag{3.30}$$

$$\sigma_{xx,2}(z) = \sigma_{yy,2}(z) = \sigma_2(z) = E\_2 \{ \varepsilon(z) - [\alpha_2(z) \Delta T]\} \tag{3.31}$$

where $E\_1 = \{E_1(z) / (1- \upsilon_1(z))\}$ and $E\_2 = \{E_2(z) / (1- \upsilon_2(z))\}$ are the biaxial modulus, E_1 and E_2 are the elastic Young's modulus, υ_1 and υ_2 are Poisson's ratio, α_1 and α_2 are the thermal coefficient of expansion of each material. ΔT is the difference of temperature from room temperature, 20°C, and bonding temperature, 300°C or 350°C. ΔT is negative since the final temperature is room temperature after the sample cools. The net force and moment, resulting from the principal stresses, cause an external reaction force and moment found using these equilibrium equations:

$$\text{force: } \int_{-h_2}^{0} \sigma_2(z)dz + \int_0^{h_1} \sigma_1(z)dz = 0 \tag{3.32}$$

$$\text{moment: } \int_{-h_2}^{0} \sigma_2 z(z)dz + \int_0^{h_1} \sigma_1 z(z)dz = 0 \tag{3.33}$$

The in-plane normal strain, ε_o, is derived from 3.29-3.33. It is dependent on geometry, change in temperature, thermal coefficient of expansion, Poisson's ratio, and elastic moduli of each layer:

$$\varepsilon_o = \frac{\Delta T}{D}\left\{X\alpha_1 + Y\alpha_2 + Z\left(4h_2^2\alpha_1 + 4h_1^2\alpha_2 + 3h_1h_2[\alpha_1 + \alpha_2]\right)\right\}$$ (3.34)

where $X = E\_1^2 h_1^4$, $Y = E\_2^2 h_2^4$, $Z = E\_1E\_2h_1h_2$, and $D = A + B + C(4h_1^2+6h_1h_2+4h_2^2)]$.

Finally, the K_{Plate_Theory}, plate theory curvature, is derived:

$$\kappa_{Plate\_Theory} = \frac{E}{D}6h_1h_2\left(h_1 + h_2\right)$$ (3.35)

where $E = E\_1E\_2 (\alpha_1 - \alpha_2)\Delta T$.

Equation 3.35 is dependent on $\Delta\alpha$, the biaxial moduli (E_1, E_2), thickness (h_1, h_2) and ΔT. The average material properties, $\Delta\alpha$ and biaxial moduli (E_1), are used to calculate curvature because the sample cools down from the bonded temperature to room temperature. The following calculations show how the average $\Delta\alpha$ (defined as effective α) and biaxial moduli (E_1) are calculated as a function of temperature.

First, the average Si biaxial modulus is calculated. The Si modulus of elasticity is dependent of crystal plane and direction, so the stress and strain in tensor form are related in Eqn. 3.36 [1]. The stress, σ_a is equal to summation of the stiffness coefficients, C_{ab}, and strain, ε_b. The constants, a and b, refer to the x and y axes or directions.

$$\sigma_a = \sum_b C_{ab}\varepsilon_b$$ (3.36)

After inverting Eqn. 3.36, Eqn. 3.37 shows how ε_b is equivalent to the summation of the compliance coefficients, S_{ab}, and σ_a [1]. The compliance coefficients, S, are equivalent to C^{-1}.

$$\varepsilon_a = \sum_b S_{ab} \sigma_b \qquad (3.37)$$

Si is a cubic, symmetric material, so instead of having 21 independent, C_{ab} components, this material has three. The stiffness coefficients are shown in matrix form [1]:

$$C = \begin{array}{cccccc}
C_{11} & C_{12} & C_{12} & 0 & 0 & 0 \\
C_{12} & C_{11} & C_{12} & 0 & 0 & 0 \\
C_{12} & C_{12} & C_{11} & 0 & 0 & 0 \\
0 & 0 & 0 & C_{44} & 0 & 0 \\
0 & 0 & 0 & 0 & C_{44} & 0 \\
0 & 0 & 0 & 0 & 0 & C_{44}
\end{array}$$

These stiffness coefficients, C_{ab}, are temperature dependent. Table 7 shows the temperature dependent stiffness factors used to calculate C_{11}, C_{12}, and C_{44} at a specific ΔT. In order to calculate these stiffness factors at each bonding temperature, ΔT is positive, since it is calculated by the difference between the bonding temperature (the final temperature) and the room temperature, 20°C (the room temperature). These calculated values are found in Table 8.

Table 7: Silicon Stiffness Material Constants [37]

Elastic Material Properties	Stiffness Constants
Elastic Stiffness at room temperature and atmospheric pressure	$C_{11} = 165.6$ GPa $C_{12} = 63.9$ GPa $C_{44} = 79.5$GPa
Temperature Dependence of the elastic stiffness Factors	$dC_{11}/dT = -9.4e-5$ K^{-1} $dC_{12}/dT = -9.8e-5$ K^{-1} $dC_{44}/dT = -8.3e-5$ K^{-1}

Table 8: Elastic Constants as a Function of Temperature [37]

ΔT (°C)	C_{11} (GPa)	C_{12} (GPa)	C_{44} (GPa)
80	164.4	63.44	78.98
130	163.6	63.13	78.65
180	162.8	62.81	78.32
230	162.1	62.50	77.99
265	161.5	62.28	77.76
280	161.3	62.19	77.66
330	160.5	61.87	77.33

Once C_{11}, C_{12}, and C_{44} are calculated in Table 8, each constant is inserted into a 6x6 matrix, and put into a Matlab v.6.1™ program. The Matlab v.6.1 ™ program, shown below, inverts this C matrix into an S matrix at ΔT from 20°C to 100°C.

C_{11} = 1.644e11;
C_{12} = 6.344e10;
C_{44} = 7.898e10;
C_{100}=[$C_{11}C_{12}C_{12}$0 0 0;C_{12} $C_{11}C_{12}$ 0 0 0; $C_{12}C_{12}C_{11}$ 0 0 0;0 0 0 C_{44} 0 0;0 0 0 0C_{44} 0;0 0 0 0 0C_{44}];
S_{100}=inv(C_{100})

The S matrix is calculated in order to find the S_{11} and S_{12} values as a function of temperature. Equation 3.1 uses S_{11} and S_{12} to calculate the biaxial modulus. Table 9 shows the value at each bonded temperature, and the average from the bonded temperature to room temperature. The CVD SiC and glass biaxial moduli are also included in Table 9. The values of the CVD SiC elastic modulus are taken from the manufacturer's data at certain temperatures, and then curve-fitted to obtain the values for the range of temperatures of interest. The calculated biaxial modulus for both Pyrex™ and HOYA SD-2™ glasses were calculated since the specific values have not been determined at each temperature. The glass biaxial modulus decreases as temperature increases. The biaxial modulus decreases approximately 1% per 100°C [38]. Each material's average biaxial modulus at the bonding temperatures, 300°C and 350°C, is used to calculate curvature.

Table 9: Average Biaxial Modulus

Biaxial Modulus Average (GPa)				
Temp ©	Pyrex™	HOYA SD-2™	Si	CVD SiC
20	79.500	114.81	180.51	589.87
100	78.710	113.67	178.89	584.81
150	78.310	113.09	177.94	581.65
200	77.910	112.52	177.30	578.48
250	77.510	111.94	176.68	576.14
300	77.120	111.37	175.44	573.78
350	76.720	110.80	174.83	571.79
avg_300	78.177	112.90	177.79	580.79
avg_350	77.969	112.60	177.37	579.66

Next, the effective α, is calculated using Eqn. 3.38. Equation 3.38 is defined using ΔT as the difference between the bonding temperature and room temperature, and the difference in expansion (ΔL) from the initial length (L_o) to the length at the specific temperature (L). It calculates the average TCE at each bonding temperature. This calculation assumes that the room temperature is 20°C.

$$\alpha = \frac{\frac{\Delta L}{L_o}}{\Delta T} \tag{3.38}$$

The Si thermal coefficient of expansion is determined using Equation 3.39 from [28], valid for 120<T<1500K. Table 12 shows the Si effective α calculations.

$$\alpha = 3.725e - 6\left[1 - \exp(-5.88e - 3(T - 124))\right] + 5.548e - 10 * T \equiv within \pm .2e - 6 \tag{3.39}$$

The effective α for Hoya SD-2™ and CVD SiC is found using a fit curve from manufacturer's data. According to Corning's Datasheet, the effective TCE for Pyrex™, Corning #7740, is constant at 3.25 ppm/C. Table 10, Table 11, and Table 13 show the effective values of α for these materials.

Now, the plate theory error bars, $K_{Plate\_Theory}(+)$ and $K_{Plate\_Theory}(-)$ are calculated from sources of error estimated in the effective values of α, manufacturer's thickness data, h_1 and h_2, and bonding temperature. The Si α calculation, Eqn. 3.39, has an error within +/-0.2 ppm/C [28]. In order to be consistent, it is assumed that the error is the same for Pyrex™, Hoya SD-2™, and CVD SiC. Table 10, Table 11, Table 12, and Table 13 show the estimated error in the effective values of α for each material.

Table 10: Effective Alpha for Pyrex[TM] [19]

Effective Alpha from 20°C (ppm/°C)			
Temp. (°C)	Pyrex[TM]	Error (+0.2)	Error (-0.2)
20	3.250	3.450	3.050
50	3.250	3.450	3.050
100	3.250	3.450	3.050
150	3.250	3.450	3.050
200	3.250	3.450	3.050
250	3.250	3.450	3.050
285	3.250	3.450	3.050
300	3.250	3.450	3.050
350	3.250	3.450	3.050

Table 11: Effective Alpha for Hoya SD-2[TM] [20]

Effective Alpha from 20°C (ppm/°C)			
Temp. (°C)	Hoya SD-2[TM]	Error (+0.2)	Error (-0.2)
20	2.260	2.460	2.060
50	2.400	2.600	2.200
100	2.607	2.807	2.407
150	2.787	2.987	2.587
200	2.923	3.123	2.723
250	3.059	3.259	2.859
285	3.154	3.354	2.954
300	3.194	3.394	2.994
350	3.298	3.498	3.098

Table 12: Effective Alpha for Silicon [26]

Effective Alpha from 20°C (ppm/°C)			
Temp. (°C)	Si	Error (+0.2)	Error (-0.2)
20	2.510	2.710	2.310
50	2.633	2.833	2.433
100	2.811	3.011	2.611
150	2.961	3.161	2.761
200	3.088	3.288	2.888
250	3.196	3.396	2.996
285	3.263	3.463	3.063
300	3.290	3.490	3.090
350	3.371	3.571	3.171

---

[19] Pyrex Data Sheet, downloaded from the Corning, Inc.
<http://www.corning.com/lightingmaterials/products/index_pyrex.html> accessed August 6, 2002
[20] Hoya Corporation, Glass Substrates for Silicon Sensors, CA, USA

Table 13: Effective Alpha for CVD SiC[21]

Effective Alpha from 20°C		(ppm/°C)	
Temp. (°C)	CVD SiC	Error (+0.2)	Error (-0.2)
20	2.373	2.573	2.173
50	2.506	2.706	2.306
100	2.713	2.913	2.513
150	2.901	3.101	2.701
200	3.068	3.268	2.868
250	3.215	3.415	3.015
285	3.314	3.514	3.114
300	3.345	3.545	3.145
350	3.462	3.662	3.262

The manufacturer's quoted thickness error is shown in Table 14.

Table 14: Thickness Error Bars [22,23,24,25]

Thickness Error Bars (µm)			
Material	Thickness Of Material	(+ Error Bar)	(- Error Bar)
Pyrex[TM]	762	787	737
Hoya SD-2[TM]	762	812	712
P-type Si	508	533	483
CVD SiC	470	495	445

ΔT error is shown in Table 15. Since the bonds were performed in an open bonder, the principal sources of error are from the difference in temperature reading on the temperature monitor, and the actual temperature on the bonding stage. A Type-K thermocouple was used to measure the actual temperature on the bonding stage. The difference in temperature is 13°C.

Table 15: ΔT Error Bars

Error (°C)	ΔT at 300°C	ΔT at 350°C
Positive Error Bar (+13)	293	343
Negative Error Bar (-13)	267	317

---

[21] Morton Advanced Materials, CVD Silicon Carbide, MA, USA.
[22] Pyrex Manufacturer's Data: Bullen Ultrasonics, Inc., Eaton, OH.
[23] Hoya Manufacturer's Data: Hoya Corporation USA, San Jose, CA.
[24] Silicon Manufacturer's Data: Si-Tech, Inc., Topsfield, MA.
[25] Accumet Engineering Corporation, Lapped and Polished Ceramic, Hudson, MA USA.

Table 16 shows an overview of the sources of error found to calculate the error bars.

Table 16: Total Sources of Error

Material Property	Error bar (+)	Error bar (-)
TCE, α: Pyrex™, HOYA SD-2™, Si, CVD SiC	+0.2 ppm/°C	-0.2 ppm/°C
Thickness, h: Manufacturer thickness		
Pyrex	+25 um	- 25 um
HOYA	+ 50 um	- 50 um
Si	+ 25 um	- 25 um
ΔT, Temperature difference during bonding	+ 13°C	- 13°C

3.4.3 Curvature Calculation from Experimental Results

The K_{tencor}, curvature, value is determined from the Tencor™ scan. The scans give a deflection measurement, and then K_{tencor} is calculated using the bow and curvature formulas. The following shows a procedure of how K_{tencor}, curvature, is calculated.

The Tencor™ machine is used to find the deflection. The laser scans the sample in the x-direction. The dimensions of the sample are Lx = 1.8 cm x Ly=1.2 cm. Since it is in a state of equal biaxial stress and strain, the scan direction is arbitrary. The scan length in the x-direction is approximately 1.28 cm. Figure 3-28 shows the die sample and scan.
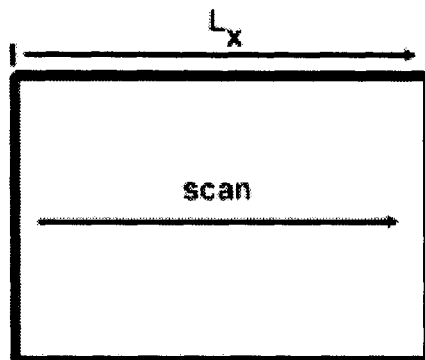
Die Sample

Figure 3-28: Die Size Sample Scan

The bow is related to a parabolic curve shown in Figure 3-29 and defined as:

$$bow = y = Px^2$$

(3.40)

At small values of the bow, the hemispherical curve from the deflection reading and parabolic curve are very similar in order for the relation and calculation to work [39]. The variable P in Equation 3.40 is the deflection measured by the Tencor™. The x^2 variable in same equation is the radius or ratio of half the die length to half the scan length defined in Equation 3.41.

$$x^2 = \frac{\left(\dfrac{die\_length}{2}\right)^2}{\left(\dfrac{scan\_length}{2}\right)^2}$$

(3.41)
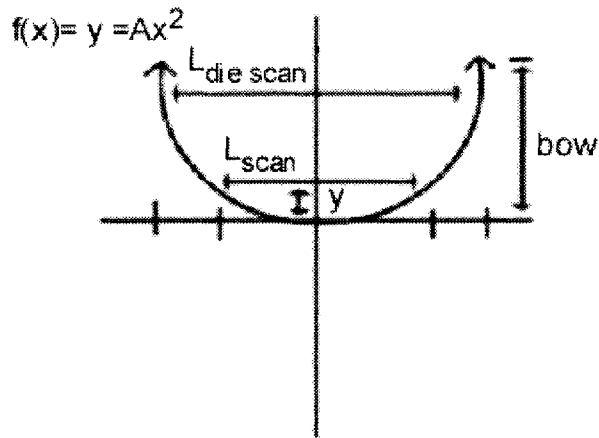
Figure 3-29: Bow Calculation

Once the bow is calculated, the radius of curvature, ρ, is found using Equation 3.42 [40]. See Figure 3-30.

$$\rho \approx \left(\frac{w^2}{8}\right)\left(\frac{1}{y}\right)$$

(3.42)

where w = scan length (1.28cm) and y = bow (Equation 3.40).
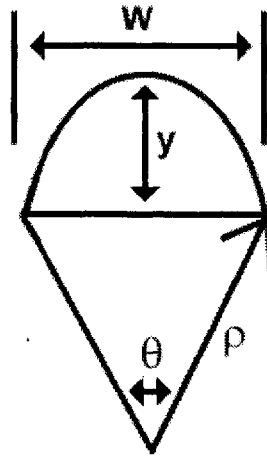
Figure 3-30: Bow Geometry

Finally, the curvature is calculated using Equation 3.43 [40].

$$K_{Tencor} = \frac{1}{\rho} \qquad (3.43)$$

where ρ is the radius of curvature of Equation 3.42.

The experimental curvature scatter is found from multiple sample deflection readings using the Tencor™. These scatter readings show the cumulative error from the bonding process and Tencor™ analysis.

3.4.4 ANSYSv.6.0 Curvature Modeling

ANSYSv6.0 modeling is performed in the following section because the bonded glass to Si/CVD SiC sample has a low aspect ratio, and the assumptions of plate theory break down. The calculation of the equal-biaxial stress state in a plate is dependent on L_x or $L_y \gg h_1 + h_2$ [34]. The sample has an aspect ratio of 10 because L_x or L_y is approximately ten times greater than the total thickness: 12,000μm (L_y) or 18,000μm (L_x) $\gg$ 1270μm (total thickness). The low aspect ratio of this bilayer plate is modeled in order to compare the ANSYSv.6.0 curvature predictions, K_{ANSYS}, to the calculated ones, K_{Plate_Theory}.

The ANSYSv.6.0 input listing is located in Appendix 7.1. This program finds the deflection of the bonded sample of glass to Si/CVD SiC. A 3-D bimaterial model,

using a 3-D 20-Node Structural Solid elements (SOLID95), was built, shown Figure 3-31, using the actual dimensions of the die size sample. The length of the sample is 18 mm, the width is 12mm, Pyrex^{TM} or Hoya SD-2^{TM} glass has a thickness of 762μm, and the Si has a thickness of 508μm. The top node on each of the four corners of the bimaterial is fixed in either the x, y, or z directions. Figure 3-31 shows the fixed boundary conditions on each node. A thermal load, ΔT, is applied to the structure. The output calculates the prediction of peak deflection in the y-direction.
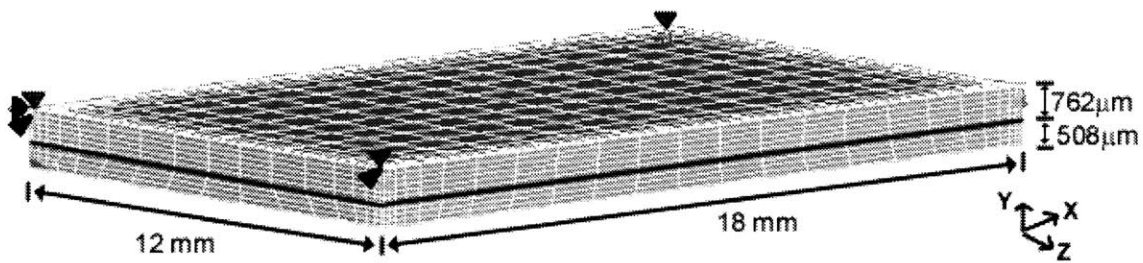
Figure 3-31: ANSYSv6.0 3-D Bimaterial Dimensions with Boundary Conditions

Figure 3-32 shows a deflected plate from the thermal load, ΔT=-330, and effective $\Delta \alpha$ between Pyrex^{TM} and Si. The effective α as a function of ΔT, elastic modulus, and Poisson's ratio, used as material properties in the model, are found in Table 2, and Table 10 - Table 13. The peak deflection from the fixed nodes on each edge is used to calculate the radius of curvature. For example, Figure 3-32 shows that 1.90μm is the peak deflection of the Pyrex^{TM}/Si bimaterial from each fixed node at zero deflection on the edges. This peak deflection value along with the bimaterial length (18mm) is used in Equation 3.42 to calculate the radius of curvature. Finally, the curvature is calculated using Equation 3.43.
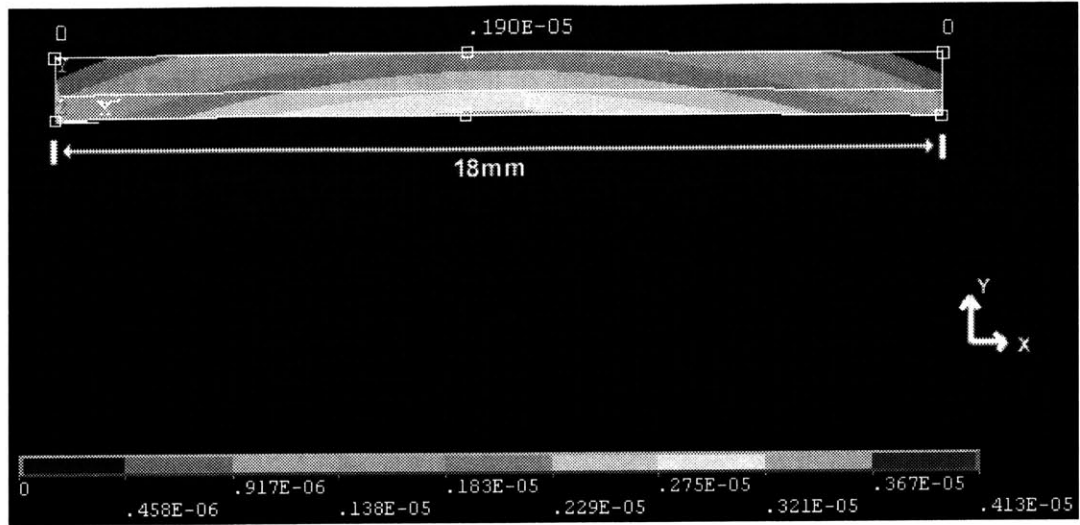
Figure 3-32: Side View of the deflection of Pyrex^{TM} glass bonded to silicon at ΔT=-330°C

Chapter 4
Anodic Bonding of Bulk Glass to Silicon and CVD Silicon Carbide

The following chapter details the bulk glass to Si and CVD SiC experimental procedure, process variables, and bonding equipment, microscopy analysis, and the bonding results and discussion in the context of the modeling of Chapter 3.

4.1 Experimental Procedure

All the materials were prepared in a Class 100 clean room.

First, a contact angle experiment was performed to test how well the hydrophilic and hydrophobic surfaces were established onto glass, Si, and CVD SiC. Hydrophobic and hydrophilic surfaces were created on Si and CVD SiC die size pieces after the pieces were cleaned using a 10 minute Piranha dip with a 3:1 concentration of H_2SO_4:H_2O_2 at 120°C, 3 minute DI wash, and N_2 gun dry. The hydrophobic surface was applied using a standard procedure of a 10 minute Piranha dip, 3 minute DI rinse, 1 minute 1:1 H_2O:BHF dip, 3 minute DI rinse, and a N_2 gun dry. A hydrophilic surface was created using a hydrophilic solution of 6:1:4, DI water: H_2O_2: NH_4OH at 60°C for 5 minutes [19]. The contact angles were measured on each material surface using a goniometer. The results from this contact angle experiment along with all the other variables of the experiment were added as variables in a matrix using a design of experiments software program, JMPv.3.1.

Second, the Plaza Test Mask and control samples used for modeling were prepared. Bulk Pyrex™ and Hoya SD-2™ 4-inch glass wafers with 30 mil thickness, and Si 4-inch wafers with 20 mil thickness were labeled and cleaned using a 20 minute 3:1 (H_2SO_4:H_2O_2) Piranha. A standard photolithography procedure was used to develop the Plaza Test Mask onto the glass wafers. The structures were etched into the glass because CVD SiC is very hard and etching into the material would be extremely time consuming. A 7:1 BHF solution was

used to etch bulk Pyrex™ wafers at an etch rate of 24nm/min, and a 20:1 $NH_4F:HF$ solution was used to etch bulk Hoya wafers at an etch rate of 100nm/min. The glass wafers were etched down to 0.2µm and 0.4µm. The etch depths of the Plaza Test structures were measured using the DEKTAK 3STv.2.12. After measuring the 0.2µm etch depth target, HOYA SD-2™ underetched depths ranged from 0.18µm-0.2µm whereas Pyrex™ resulted in overetched depths of 0.2µm-0.25µm. The photoresist was stripped and the glass wafers were cleaned using a 5 minute acetone dip, 2 minute IPA (isopropanol) wash, 5 minute DI wash, 5 minute Piranha, and 5 minute DI wash. The 20 die size Plaza Test Mask pieces on the glass wafer were diced into 20 1.8 cm x 1.2 cm samples using a Disco diamond blade dicing saw. Unetched glass die pieces were also cut into 1.8 cm x 1.2 cm control pieces for the curvature experiments. Finally, 1.8 cm x 1.2 cm die size Si pieces were cut from the wafers.

The CVD SiC die size samples were prepared differently. The CVD SiC wafers at a thickness of 475 µm were fabricated using chemical vapor deposition at Rohm and Haas. Ferro-Ceramic Grinding Inc. diced the wafers samples into 1.8 cm x 1.2 cm. Accumet Engineering Corporation lapped and polished the CVD SiC to a specific surface roughness needed for bonding. The new thickness of CVD SiC was approximately 470µm. These samples were cleaned using the Rohm Haas cleaning procedure: lint free cloth wipe, IPA-soaked lint free cloth wipe, 5 minute DI water with 2% Micro at 120°C dip, 5 minute DI water soak at 120°C, 90 second 1:1:1 $HF:HNO_3$: DI water soak at room temperature, 5 minute DI overflow rinse, 5 minute DI water ultrasonic at 120°C, 5 minute DI overflow rinse, and N_2 gun dry.

Once the glass, Si, and CVD SiC samples were prepared for bonding, they were taken into an open lab where the anodic bonding equipment was located. In this lab, the hydrophilic and hydrophobic surfaces were applied onto the Si and CVD SiC samples under a hood. Once the samples were taken out of the hydrophilic dip, they were dried using a N_2 gun, and taken directly to the anodic bonder to

bond with the glass samples. The Si or CVD SiC piece was placed first onto the hot plate of the anodic bonder which was connected to the anode, and then the glass piece was placed on top of the Si. The cathode was placed on top of the glass piece of the glass- Si pair. Temperatures of 300 or 350°C, voltages of 500 or 1000V, and a time of 10 minutes along with other variables of the JMPv.3.1 Experimental Matrix were the bonding parameters/conditions used. The JMPv.3.1 Experimental Matrix included several different parts defining the bonding conditions of particular experiments. Once the Plaza Test Mask samples were bonded, each was visually inspected in order to see how many structures of the array bonded. The number bonded was documented for the bond toughness analysis. A Zeiss KS 300 3.0 Microscope was used to measure the unbonded sides or crack lengths of each bonded structure.

A separate experiment to determine the difference between bonding a Plaza Test Mask with a hydrophobic versus hydrophilic Si surface was performed. Experiment 1 Part #7 of the JMPv.3.1 Matrix bonded Hoya SD-2^{TM} to a hydrophilic Si surface at 1000V and 350°C for 10 minutes. Another test was performed using the same bonding parameters as Experiment 1 Part #7, but using a hydrophobic Si surface. The bonded area was micro-imaged using an acoustic microscope, C-Mode Scanning Acoustic Microscope (C-SAM^{TM}) (trademark of Sonoscan^{TM}) with a 230 MHz center frequency transducer and a 0.25" focal length.

The bonding of the control samples used for the curvature experiment depended on which Plaza Test samples of the JMPV.3.1 Experimental matrix had successful bonded rectangular structures. The control samples were bonded using the same equipment and procedure as for the Plaza Test Mask samples. Once the samples were cooled to room temperature, they were taken to the Tencor^{TM} machine for analysis.

4.1.1 Process Variables

Anodic bonding involves several parameters that affect the quality of the bond. The applied voltage, bonding temperature, thickness of glass, bonding time, and pretreatment of surface all influence the bond quality of bonding Pyrex™ and Hoya SD-2™ glasses to Si and CVD SiC. Therefore, all these different variables are included in this study. A Design of Experiments software program, JMP v.3.1 was used to narrow down the overall 32-part matrix into an 8-part experimental matrix, Table 17. This matrix defines the conditions of bulk glass to Si and CVD SiC bonding.

Table 17: JMPv.3.1 Experimental Matrix

Experiment Part	# samples	Bulk Glass	Si Surface Dip	Glass Etch Depth (μm)	Voltage (V)	Temp. (°C)	Time (min.)
1	3	Pyrex™	Hydrophobic	0.2	1000	350	10
1 control	3	Pyrex™	Hydrophobic	No etch	1000	350	10
2	3	Pyrex™	Hydrophobic	0.4	500	300	10
2 control	3	Pyrex™	Hydrophobic	No etch	500	300	10
3	3	Pyrex™	Hydrophilic	0.2	500	300	10
3 control	3	Pyrex™	Hydrophilic	No etch	500	300	10
4	3	Pyrex™	Hydrophilic	0.4	1000	350	10
4 control	3	Pyrex™	Hydrophilic	No etch	1000	350	10
5	3	HOYA SD-2™	Hydrophobic	0.2	500	350	10
5 control	3	HOYA SD-2™	Hydrophobic	No etch	500	350	10
6	3	HOYA SD-2™	Hydrophobic	0.4	1000	300	10
6 control	3	HOYA SD-2™	Hydrophobic	No etch	1000	300	10
7	3	HOYA SD-2™	Hydrophilic	0.2	1000	300	10
7 control	3	HOYA SD-2™	Hydrophilic	No etch	1000	300	10
8	3	HOYA SD-2™	Hydrophilic	0.4	500	350	10
8 control	3	HOYA SD-2™	Hydrophilic	No etch	500	350	10

4.1.2 Anodic Bonding Equipment

The Anodic Bonder, open to the ambient environment, is shown in Figure 4-1. This schematic shows how the voltage and temperature are applied to the sample during the bonding period. The bonder consists of a 100 Watt D.C. American High Voltage supply, and K-type thermocouple temperature source. A resistor box is connected to the bonding equipment in series which is linked to the Labview program in the computer monitoring the change in sample current with respect to time. The change in voltage of a selected resistor, i.e. 2 Ohms in

Figure 4-1, from the resistor box is monitored and converted to give a current versus time output on the computer.
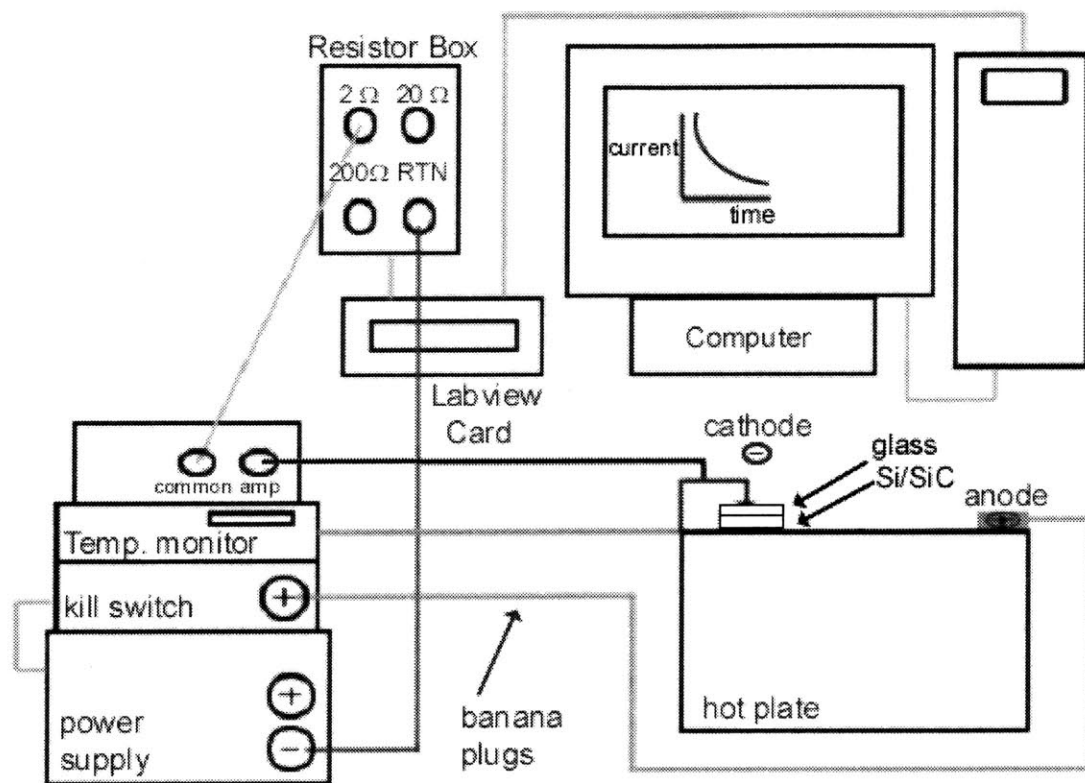
Figure 4-1: Schematic of the Anodic Bonder

4.1.3 Contact Angle Measurement

The contact angle of hydrophilic and hydrophobic surfaces is determined to quantify the degree of hydrophilic and hydrophobic surfaces on Pyrex^{TM}, HOYA SD-2^{TM}, Si, and CVD SiC. Figure 4-2 shows the contact angle between the water and the material surface. A drop of water was placed on the surface of each material and then the angle was measured by the goniometer.
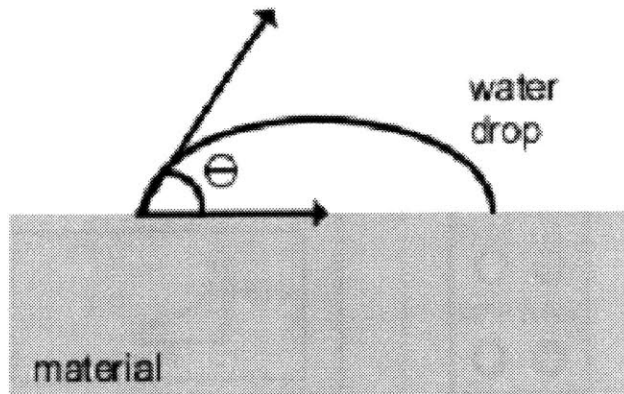
Figure 4-2: Contact Angle

4.1.4 Anodic Bonding using CVD SiC

A WYKO[TM] instument, measured the average RMS surface roughness of the CVD SiC samples at 169nm. References state that anodic bonding is successful using materials with an average RMS surface roughness of less than 1 μm [2]. In the present work bonding CVD SiC to bulk glass did not occur using temperatures of 300°C and 350°C, and voltages of 500V and 1000V. Since the temperatures and voltages needed to be kept low and consistent to the parameters normally used during anodic bonding, the surface roughness was investigated. The CVD SiC samples were outsourced to Accumet Engineering Corporation for polishing. The polished CVD SiC average RMS surface roughness was measured again using the WYKO[TM]. The lower RMS surface roughness, 45nm, resulted in successful bonding. A wide range of voltages, 200-1000V and low temperatures of 300°C and 350°C were used, and successfully bonded flat, unetched Pyrex[TM] and Hoya SD-2[TM] glass to CVD SiC. The Plaza Test Mask was etched into the glass (using the same procedure as in Section 4.1), and bonded to the CVD SiC using the JMPV.3.1 Experimental Matrix.

4.1.5 TEM and STEM/XEDS Work

Transmission electron microscopy (TEM) was performed on the control samples in order to observe depletion layers present in the Pyrex[TM] and Hoya SD-2[TM] when bonded to p-type Si and CVD SiC. Scanning transmission electron

microscopy and X-ray energy-dispersive spectroscopy (STEM/XEDS) microanalysis chemically analyzed these layers. Table 18 shows the arbitrary bonding parameters used to bond Pyrex™ and Hoya SD-2™ glass to Si and CVD SiC.

Table 18: TEM/STEM Bonding Matrix

Interface	Voltage (V)	Temp. (°C)	Time (min.)
Pyrex™ / Si	1000	350C	20
Hoya SD-2™ / Si	1000	350C	20
Pyrex™ / CVD SiC	1000	350C	20

Samples for each part of the experiment were bonded, cooled, and cut into 18 mm x 2 mm pieces. Each cross-section was ground to an approximate 100 μm thickness, diced into a smaller piece, and cemented to a copper grid. The samples cemented to the copper grid were ion-beam thinned to electron transparency using the cold stage of the GATAN DuoMill 600 DIF with beam accelerating voltage of 6kV, beam glancing angle of 15°, and sample rotating 360°.

The thinned samples were examined in a JEOL 2000 FX microscope. Each sample was observed at 200-kV, 10-100 kX magnification, using bright-field, Si dark-field, glass dark-field, Si weak-beam imaging conditions. Thicknesses of the depletion layers were measured by reference to the scale bar appearing on the negatives, and were subject to +/- 5% error.

A UHV dedicated VG HB603 STEM was used, operating at 250kV. The depletion layers were measured again using the scale bar on the computer monitor, and the X-ray counts of the different elements characteristic of each glass were collected along a scan through the interface and into the bulk of the glass.

4.2 Results and Discussion

4.2.1 Hydrophilic versus Hydrophobic Surfaces

There were two objectives for analysis of the hydrophilic and hydrophobic surfaces. First, the contact angle experiment gave results on how well hydrophobic and hydrophilic surfaces can be created on Si and CVD SiC. The hydrophilic surface contact angles determined how many available Si bonds there were on the native oxide, SiO_2, surface for –OH groups to bond. It was of interest to examine how well a native oxide forms on CVD SiC. Available Si bonds are crucial for anodic bonding because they form bonds with the oxygen anions. Second, anodic bonds were made to determine if using hydrophilic versus hydrophobic Si surfaces made a difference in the current versus time output, and the area bonded.

The different trials taken in order to establish hydrophobic and hydrophilic surfaces on the materials are shown in Table 19. The 1:1 H_2O:BHF dip in Trial 1 did not create a hydrophobic glass surface because BHF etches the glass, and keeps it naturally hydrophilic with almost complete wetting angles. In Trial 2, isopropanol established a hydrophobic glass surface, but there were still many particles left on the glass which made the surface unsuitable for anodic bonding. Therefore, the hydrophilic glass dip was eliminated from the JMPv.3.1 Experimental matrix. The results of Table 19 also show that very hydrophilic surfaces were established on p-type Si. The 1:1 H_2O:BHF dip also established a very hydrophobic surface. This proves that a native oxide is evident on the Si surface. However, there is no significant difference between the contact angle values of the hydrophobic versus hydrophilic CVD SiC surfaces in each trial. There is a difference in surface roughness between the first and second trial which might affect the contact angle. The second trial had samples with a lower surface roughness. The lower surface roughness did not dramatically distinguish between the hydrophobic surface contact angle of 24°, and hydrophilic surface, contact angle of 21°. The goniometer error of +/- 3° proves that the difference between the hydrophilic and hydrophobic surfaces is minimal. A native oxide must not readily form on the CVD SiC surfaces because there are not many available Si bonds on the surface due to the strength of the Si-C bonds.

Therefore, the hydrophilic and hydrophobic CVD SiC dips are also eliminated from the JMPv.3.1 Experimental matrix.

Table 19: Contact Angles of Materials

Material Sample 1	Hydrophobic dipped surface		Material Sample 2	Hydrophilic dipped surface	
	Avg. Contact angle Trial 1 (°)	Avg. Contact angle Trial 2 (°)		Avg. Contact angle Trial 1(°)	Avg. Contact angle Trial 2(°)
Pyrex™					
Sample 1	5	43	Sample 2	6	5
HOYA SD-2™					
Sample 1	5	47	Sample 2	7	8
P-type Si					
Sample 1	70	88	Sample 2	5	8
CVD SiC					
Sample 1	41	24	Sample 2	40	21
Error of (°): +/-3					

The second part of this analysis shows the relative area bonded using hydrophilic Si versus hydrophobic Si of Experiment 1 Part #7. A Sonoscan™ acoustic microscope imaged each bonded sample. Visually, there is no difference in bonded structure area achieved by using a hydrophilic versus hydrophobic Si surfaces. These results contradict Lee et al.'s findings [19]. Figure 4-3 shows the bonded sample with a hydrophobic Si surface. Figure 4-4 shows the bonded sample with a hydrophilic Si surface. One very noticeable change, is the difference in number of bonded structures from how the original samples of Experiment 1 Part #7 bonded. The minimum width of this new test is 160µm instead of the 200µm found in the first experiment. It is unusual to bond with the same voltage and temperature, and get a different number of bonded structures. However, the two-part bond model results in Section 4.2.3 explain why this could occur.
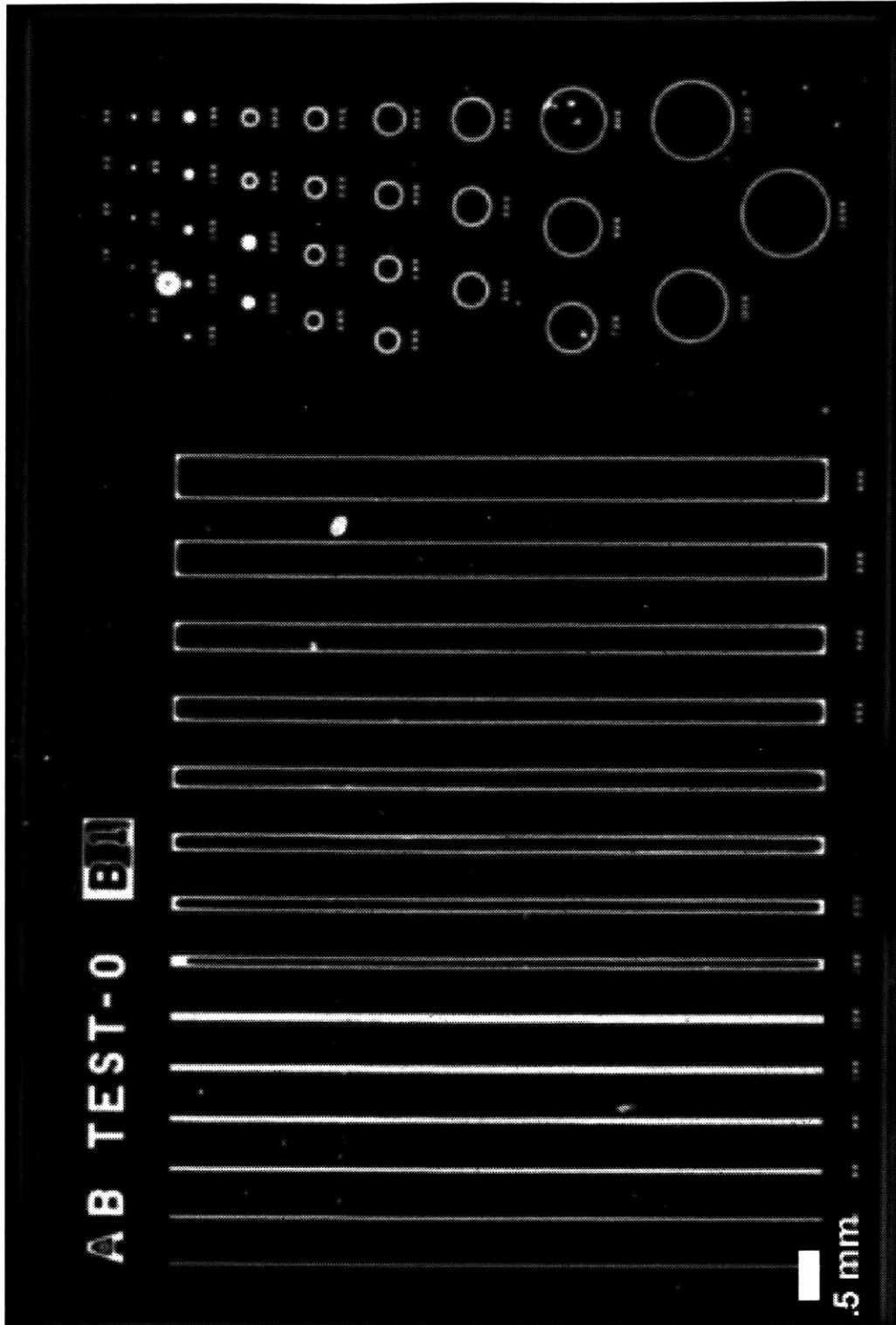
Figure 4-3: Bonded Sample with Hydrophobic Si Surface
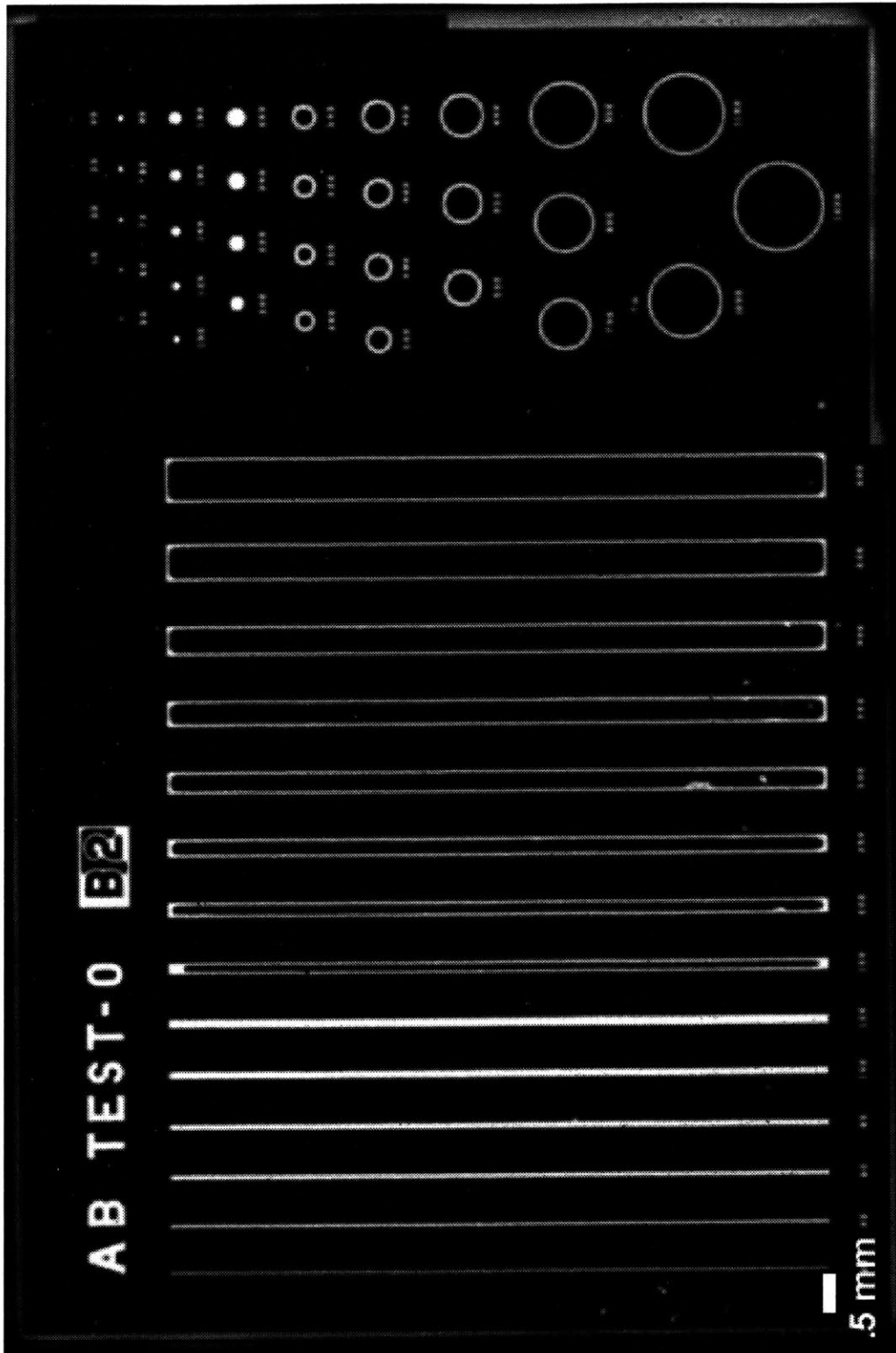
Figure 4-4: Bonded Sample with Hydrophilic Si Surface

Finally, the current versus time of hydrophobic versus hydrophilic experiments is compared to the results of both Lee et al. [19] and Cozma and Puers [17]. Figure 4-5 shows the results when bonding with the Plaza Test Mask. Bonding with hydrophilic versus hydrophobic p-type Si surface did not make a difference in the total area bonded or current versus time. These results support Cozma and Puers [17] findings because there is no significant difference in bonding current.
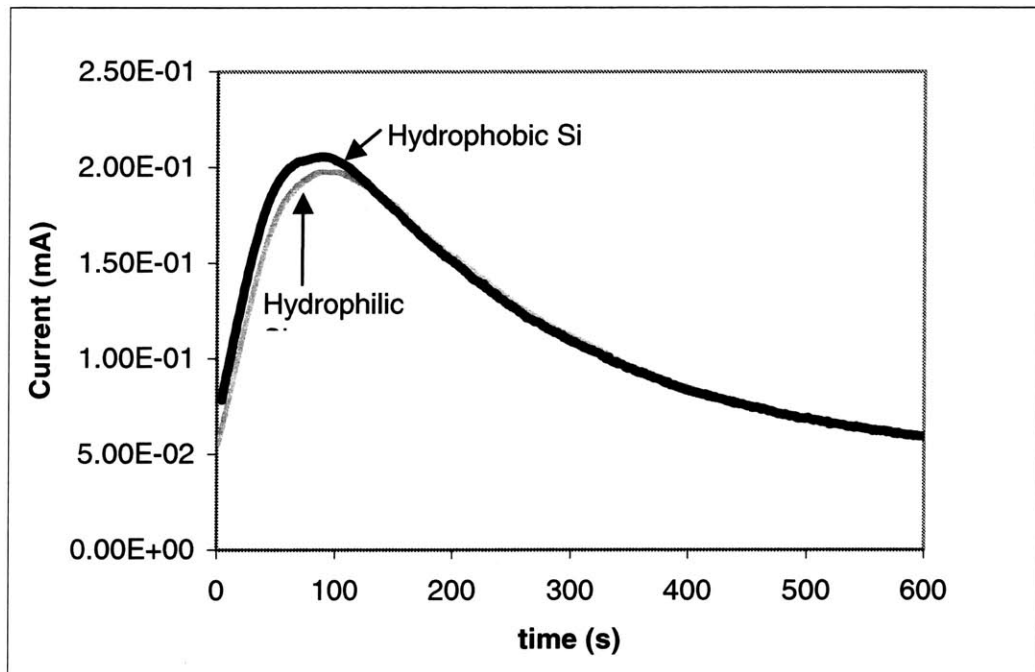
Figure 4-5: Hydrophilic vs. Hydrophobic P-type Si to Glass Bonding Current

There is not a distinct difference between bonded area and there is not a significant difference in bonding current because the applied voltage is the dominant mechanism and the surface energy is a secondary factor. A chemical analysis on the bonded interface and depletion layers would give a more detailed understanding if a hydrophilic surface aids in the anodic bonding mechanism.

4.2.2 JMPv.3.1 Experimental Matrix Results

The results of Experiment 1 bonding glass to Si and Experiment 2 bonding glass to CVD SiC are shown in Table 20 and Table 21. The minimum bonded width was determined when all the structures fully bond in the array to a minimum

width structure. Only successful bonding occurred using etch depths of 0.2µm. The parts that had partial to no bonded structures were not counted and defined as "no bond." From these results JMPv.3.1 could not predict reasonable minimum bonded widths for each part of the total thirty-two part array based on all the different variables. Since there were only three successful parts out of the original eight of Table 20 and one out of eight in Table 21, there was not enough data to define a reasonable response.

Table 20: Results of JMPv.3.1 Experimental Matrix: Exp. 1 Glass to Silicon

Exp. 1 Part	Sample #	Bulk Glass	Si Surface Dip	Glass Etch Depth (µm)	Volt. (V)	Temp. (°C)	Time (min.)	Minimum Bonded (µm) —
1	3	Pyrex™	Hydrophobic	0.2	1000	350	10	250
2	3	Pyrex™	Hydrophobic	0.4	500	300	10	No bond
3	3	Pyrex™	Hydrophilic	0.2	500	300	10	No bond
4	3	Pyrex™	Hydrophilic	0.4	1000	350	10	No bond
5	3	Hoya SD-2™	Hydrophobic	0.2	500	350	10	300
6	3	Hoya SD-2™	Hydrophobic	0.4	1000	300	10	No bond
7	3	Hoya SD-2™	Hydrophilic	0.2	1000	300	10	200
8	3	Hoya SD-2™	Hydrophilic	0.4	500	350	10	No bond

Table 21: Results of JMPv.3.1 Experimental Matrix: Exp. 2 Glass to Silicon Carbide

Exp. 2 Part	Sample #	Bulk Glass	Glass Etch Depth (µm)	Volt. (V)	Temp. (°C)	Time (min.)	Minimum Bonded (µm)
1	**3**	**Pyrex™**	**0.2**	**1000**	**350**	**10**	**500**
2	3	Pyrex™	0.4	500	300	10	No bond
3	3	Pyrex™	0.2	500	300	10	No bond
4	3	Pyrex™	0.4	1000	350	10	No bond
5	3	Hoya SD-2™	0.2	500	350	10	No bond
6	3	Hoya SD-2™	0.4	1000	300	10	No bond
7	3	Hoya SD-2™	0.2	1000	300	10	No bond
8	3	Hoya SD-2™	0.4	500	350	10	No bond

4.2.3 Two-Part Bond Model Results

The objectives of determining the principal Plaza Test Mask bonding mechanism, and applying it to the two-part bond model were accomplished. First, a discussion of the bonding mechanism is presented, and then the two-part contact/bonding model results.

The Plaza Test structures show evidence of elastic deformation during bonding. The following experimental and modeling results of the glass surface deformation demonstrate the pull-down nature of the bonded glass to Si and CVD SiC structures. The DEKTAK 3STv.2.12 profilometer scanned the top glass surface of the bonded structures on the die size sample, Figure 4-6 of Experiment 1 Part 1. Figure 4-7 shows a typical DEKTAK 3STv.2.12 scan, not drawn to scale, over the deformed 600µm and 500µm Pyrex™/Si surface. As shown in Figure 3-5 and Figure 3-10, 500µm separates each structure on the die size sample. The 500µm distance between the structures is arbitrarily defined as the reference plane, whereas the 600µm and 500µm structures deform −40nm below the reference level indicating pull-down. The ANSYSv.6.0 modeling described in Section 3.3.1 also showed a clear glass surface deformation of the bonded

structure. Figure 4-8 shows a deformation contour plot of the Pyrex[TM] glass bonded to Si. The Si material is not shown for clearer imaging. The applied constant pressure on each material surface caused the materials to deform a certain distance. Once the correct applied constant pressure placed on both interfaces allowed the materials to deform to fill the etch depth distance, 200nm, the glass surface deformation was found. The peak deformation on the Pyrex[TM] glass surface of Figure 4-8 is 71nm. Both experimental and modeling peak deformation results are compared in Table 22. Table 22 summarizes the Pyrex[TM] and Hoya SD-2[TM] glass surface pull-down of a 600µm etched structure bonded to either Si or CVD SiC. The ANSYSv.6.0 modeling and DEKTAK 3STv.2.12 scans do not account for the initial bow or error. The model results and experimental measurements are in broad agreement, suggesting that all the deformation is elastic, as modeled. However, the ANSYSv.6.0 surface deformation predictions (Table 22) could be closer in value to the experimental results. Assuming a fixed x and y boundary conditions on each side of the structure (Figure 4-8) is incorrect. If the x boundary condition was a constant value on at least one side of the structure (allowing for transverse strain) and the other side was fixed, and both sides were free in the y-direction (allowing for axial strain), then there would be smaller difference in surface deformation after bonding.
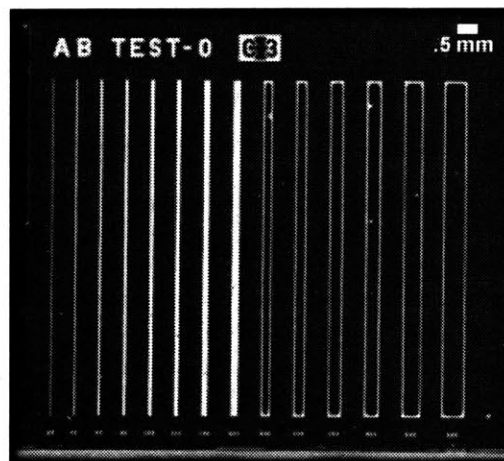
Figure 4-6: Acoustic Microscope Image of Bonded vs. Unbonded structures of Exp.1 Part 1
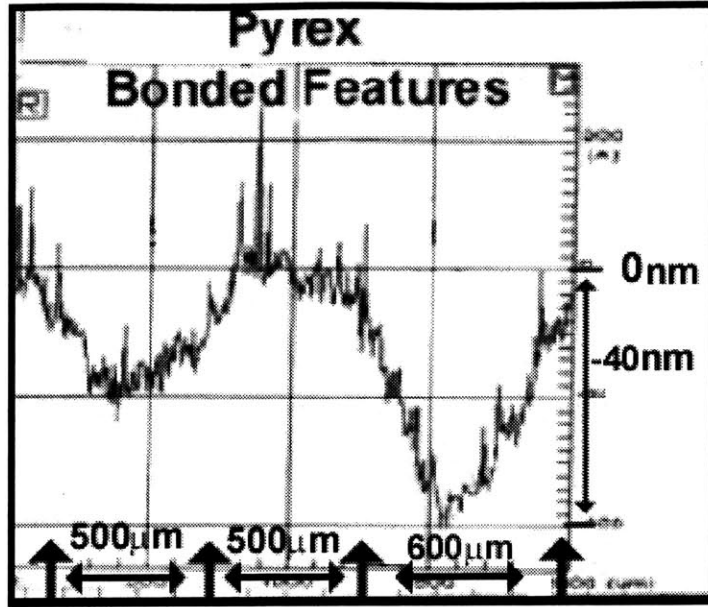
Figure 4-7: DEKTAK 3STv.2.12 Surface Scan of Pyrex/Si Bonded Structures
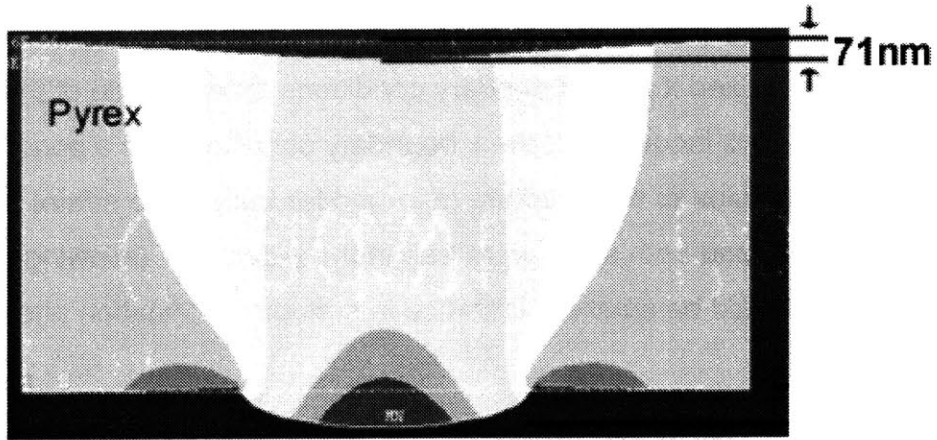
Figure 4-8: Pyrex[TM] /Silicon Deformation of 600 µm Width Structure

Table 22: Deformation of 600µm Structures with 0.2µm Etch Depth

Bonded Materials	DEKTAK Experimental Measurements (nm)	FEA Predictions (nm)
Pyrex[TM]/Si	-40	-71
Pyrex[TM]/CVD SiC	-25	-62
HOYA SD-2 [TM]/Si	-10	-45

Since elastic deformation is the principal mechanism, the use of the parallel plate capacitor pull-in model to predict contact, and linear elastic fracture mechanics to predict toughness is justified. The parallel plate capacitor model results indicate

that contact occurs when F_e exceeds the F_k at a distance in the etch depth, and V_n ($V_{applied}/V_{pi}$) is greater than 0.67. Stability is lost when the surfaces are moving at a distance in the etch depth and $F_e > F_k$. Figure 4-9 shows a magnified view of F_e as a function of width, W, versus F_k for Pyrex^{TM} to Si at 1kV and 0.2μm etch depth. This plot shows that all structures contact from W= 600μm down to 40μm. At W=600-80μm, contact occurs initially because the electrostatic force dominates at 1-g/go=0 when g= go=0.2μm. As g < go=0.2μm, the surfaces are moving and closing the etch depth. At W =40μm, the surfaces are still predicted to contact since instability occurs when,1-g/go >.5.
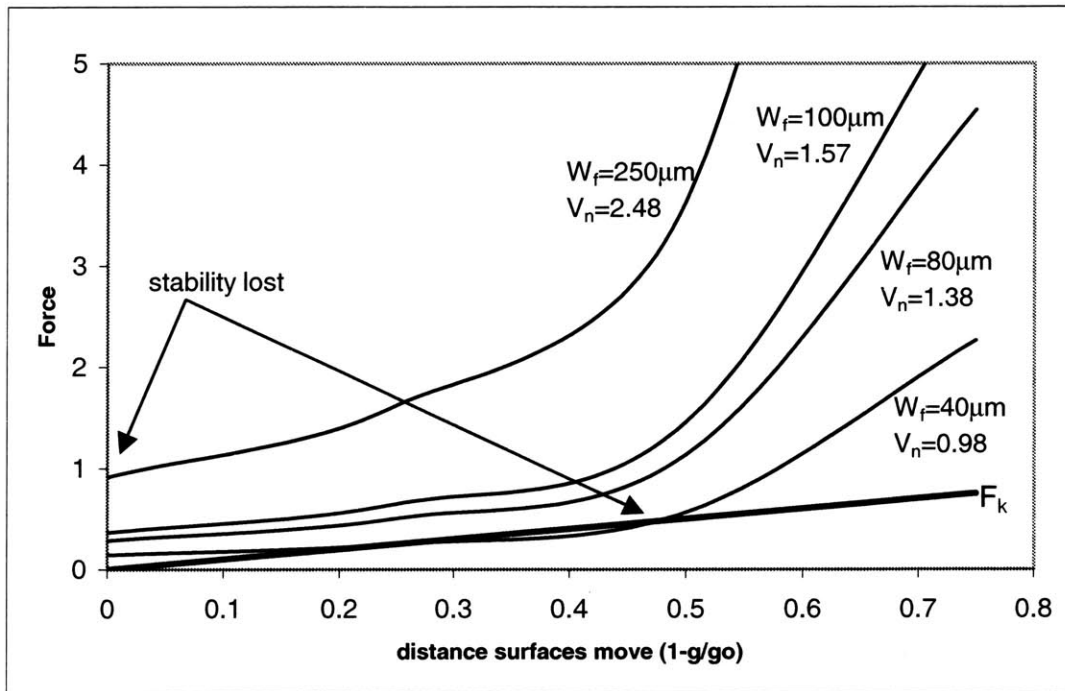
Figure 4-9: F_e as a function of W vs. F_k for Pyrex^{TM} and Si (1kV, g_o = 0.2μm etch depth)

After modeling different material systems and voltages, instability ($F_e > F_k$) at a specific width and distance in the etch depth, occurred when the ratio was greater than 0.67. V_{pi} is a function of g_o, W, and k_{eq}, so as the width decreases, V_n at a constant $V_{applied}$ also decreases. This is important because it shows the resistance of contact as a function of materials, geometry, and applied voltage.

The contact predictions are compared to the structures that remained bonded to a minimum width in Table 20 and Table 21. Table 23 shows which widths at $g_o=0.2\mu m$ are predicted to contact and which widths actually bond. Many widths predicted to contact, also bond. Therefore, the surface/ bonding energy provided by $V_{applied}$ exceeded the strain energy. Other widths predicted to contact down to a minimum bonded structure do not bond at the same minimum width because the strain energy was higher than the bonding energy.

Table 23: Table of V_n Predicting Contact at Minimum W_t versus Minimum W_t Bonded

Material Surface System	Voltage (V)	V_n at 600μm	Minimum W_t for Contact (μm)	V_n at Minimum W_t for Contact	Minimum W_t Bonded (μm)
Pyrex™ and Si $g_o = 0.2\ \mu m$	1000	4.32	40	0.98	250
	500	2.17	80	0.70	No bond
Hoya SD-2™ and Si $g_o = 0.2\ \mu m$	1000	3.79	40	0.89	200
	500	1.90	200	0.99	350
Pyrex™ and SiC $g_o = 0.2\ \mu m$	1000	3.58	40	0.85	500
	500	1.79	100	0.67	No bond

The strain energy also exceeded the bonding energy of the 0.4μm etch depth structures. None bonded in Table 20 and Table 21. However, the surfaces were predicted to contact. F_k is normalized in Figure 4-10 to show the difference in F_e as a function of g_o. F_e exceeds F_k indicating instability and predicting contact for the Pyrex™ to Si 600μm structure at 0.4μm and 1kV. The V_n ratio also indicates contact will occur since it is greater than 0.67 for each g_o.
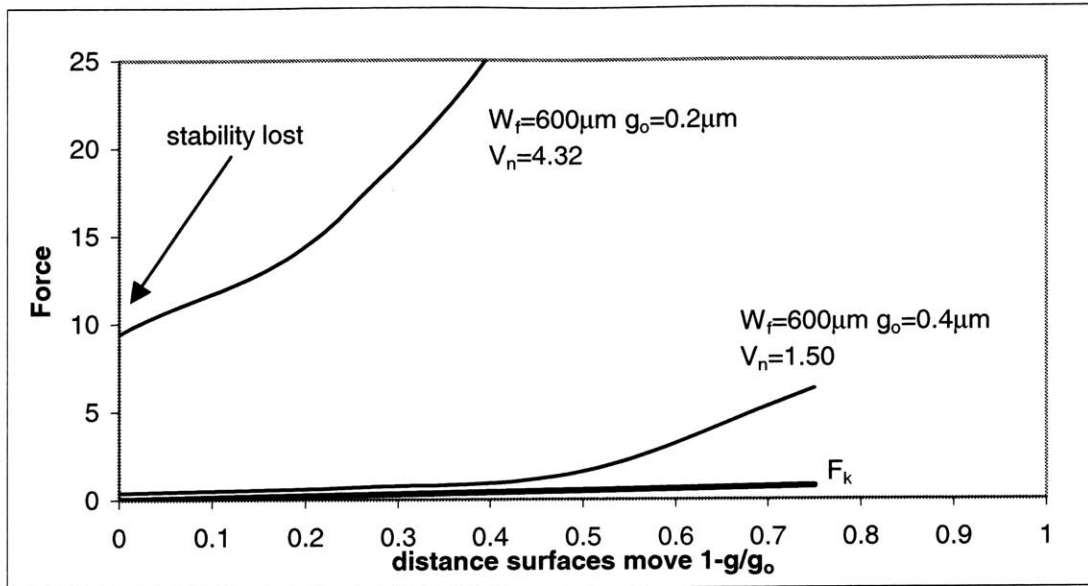
Figure 4-10: F_e as a function of etch depth (g_o) vs. F_k of Pyrex^{TM} and Si at 1kV

The G_{min} and K toughness values of the bonded structures were experimentally determined, calculated, and compared to literature results based on the boundary condition assumptions used in the model. First, the model was assumed to be constrained in the x- and y- directions on the opposite side to the symmetry line, and constrained in the x-direction on the symmetry line. These constraints did not allow rigid motion in these directions, which would result from bonding. There would have been some uniform transverse and axial strain. Therefore, the y-direction should be free on both sides of the model, and one side should be fixed in the x-direction and the other side should allow for a constant x-displacement. Second, modeling the nodal deformation or assuming boundary conditions along the 500μm surfaces between the etched structures when the voltage is applied and when it is off is uncertain and must be studied. This model assumed these surfaces were in contact, but in fact could be bonded before the structure bonds. However, constraining these 500μm surfaces to simulate a bond would not allow them to deform from the effect of the structure bonding or when the voltage is removed. Third, mode 1 fracture (or tensile opening or closing simulating bonding) was assumed as the dominant mode. In fact, the bonding is capable of mixed mode resulting from both mode 1 and mode

2 (or in-plane sliding of the bonding surfaces) since it is a bimaterial model and there is a difference of material properties at the interface. Mixed mode bonding would result in two stress intensity factors, one for each mode (tensile and shear). It could be possible that mode 2 has a significantly smaller effect than mode 1. However, the overall results in Tables 24 and 25 of the bonded glass to Si and CVD SiC, 600 and 500μm structures are promising. There is not a significant difference in toughness values. This trend is evident because the sides of the etched structures are very rigid and prevent the bond front from proceeding. However, this proves the anodic bond between glass and CVD SiC is comparable to glass to Si. Therefore, anodic bonding glass to CVD SiC is advantageous and is a reliable process.

The G_{min} values in Table 24 did not fully define the bond toughness as a function of bonding conditions. The G_{min} values between the structures vary significantly. For example, The 600μm bonded structure of Exp. 1 Part 1 has a G_{min} value of 0.28 J/m^2 differing from the 250μm structure G_{min} of 1.00 J/m^2. Table 25 shows the scatter between measured crack lengths on the minimum bonded structures. The difference in G_{min} values between all the structures in Table 24 is greater than the scatter. However, the measured crack lengths between each experimental part in Tables 24 and 25 clearly indicate a possible reason of why the ANSYSv.6.0 toughness predictions are not constant. The measured crack lengths between the structures do not vary significantly between each part. All the structures of Experiment 1 Part 1 have an average crack length of 73μm compared to an average 98μm of Experiment 1 Part 5. It seems that the ANSYSv.6.0 mesh is not fine enough at the edge of the etched region, so accurate strain energy release rate values in that area could not be calculated.

Even though the toughness is not constant, the ANSYSv.6.0 results are similar to literature results, assuming mode 1 fracture (bonding). The fracture toughness, K, calculated from G_{min}, in Table 25 are compared to Hurd et al.'s data [23]. Exp. 1 Part 1 is related to the straight-thru-crack (STC) results of Hurd et al. [23]

because similar conditions, 1kV, 350°C, and bonding materials (PyrexTM glass to Si) were used. The only differences were time, and the STC results were not interfacial values. The STC K value at 350°C was 0.680 MPa-m$^{1/2}$ [23], compared to the average K of 0.330 MPa- m$^{1/2}$ calculated from G_{min}. The average K value of this study is lower than the value found by Hurd et al. [23], so elastic deformation may not be the primary mechanism and diffusion may have a larger role in the bonding mechanism than expected. However, both values are on the same order of magnitude, so the calculated toughness values of this study are reasonable.

Table 24: Minimum G Results of Experiments 1 and 2

Experiment Part	W_t (μm)	W (μm)	Measured Crack Length, a (μm)	a/ W	G_{min} (J/m^2)
Experiment 1 Part 1	600	300	37.50	0.125	0.28
	500	250	38.97	0.156	0.35
	300	150	34.56	0.230	0.75
	250	125	34.56	0.276	1.00
Experiment 1 Part 5	600	300	46.32	0.154	0.27
	500	250	54.41	0.218	0.33
	300	150	49.26	0.328	0.81
Experiment 1 Part 7	600	300	41.94	0.140	0.30
	500	250	39.71	0.159	0.42
	300	150	36.03	0.240	0.90
	250	125	39.71	0.318	1.19
	200	100	38.97	0.390	1.67
Experiment 2 Part 1	600	300	52.21	0.174	0.29
	500	250	54.41	0.218	0.37

Table 25: Final Modeling Results of Experiments 1 and 2

Experiment Part	minimum bond W_t (μm)	minimum bond W (μm)	Measured Crack Length, a (μm)	a/ W	Min G (J/m^2)	K MPa*SQRT(m)
Exp 1 Prt 1						
Sample 1	250	125	32.35	0.259	1.10	0.341
Sample 2	250	125	34.56	0.276	1.00	0.325
Sample 3	250	125	35.29	0.282	0.99	0.324
Exp 1 Prt 5						
Sample 1	300	150	45.59	0.304	0.84	0.334
Sample 2	300	150	46.32	0.309	0.82	0.330
Sample 3	300	150	49.26	0.328	0.81	0.328
Exp 1 Prt 7						
Sample 1	200	100	38.24	0.382	1.69	0.474
Sample 2	200	100	38.97	0.390	1.67	0.472
Sample 3	200	100	41.18	0.412	1.71	0.477
Exp 2 Prt 1						
Sample 1	500	250	54.41	0.218	0.37	0.216
Sample 2	500	250	56.62	0.226	0.36	0.213
Sample 3	500	250	68.38	0.274	0.34	0.206

Overall, bonding (as opposed to contacting) is the limiting step because several structures were predicted to contact, but did not bond. However, the toughness results from the bonding model indicate that the inconsistent bonding energies per bonded structure on the array, suggests that a unique value of the interfacial work of adhesion is not sufficient to characterize the bonding process. No definitive explanation can be given, but the following reasons could explain why this is evident.

1. The mesh near the edge of the structure width should be very fine. This could lead to more constant G values.

2. Nodes along the surfaces of the materials are pulled into each other in order to simulate bonding. However, this ANSYSv.6.0 modeling process

may not relate to the anodic bond formation between the surfaces since there should be mixed mode bonding. Materials in this study do not bond to the ends of the whole structure, but they were modeled this way. The local force between the middle nodes is larger than the forces out toward the etch depth edges.

3. It is unclear what role diffusion plays during depletion layer formation and chemical bonding. However, it is likely that this plays some role in defining the effective toughness of the bonds.

4. Voltage may also have a significant role not only in contact, but keeping the materials bonded. The parts of the bond front at a specific width may move back to a minimum energy position once the voltage is removed. Voltage could also be the reason why only partial areas of the structures bonded.

4.2.4 Curvature Values

The curvature experiments had the objectives of proving that all the deformation during bonding was thermoelastic. The following results are shown in two parts.

First, the Tencor™ analysis proves thermoelastic deformation. Two samples of Pyrex™ and Hoya SD-2™ glasses were bonded to Si at approximately 300°C, and 1000V. The initial deflection measurement was made at room temperature using the Tencor™ machine. The samples were heated to temperatures, 100°C, 150°C, 250°C, and 285°C. The deflection was measured and curvature calculated at each elevated temperature. The curvature change (ΔK) , is calculated from the difference of curvature at each temperature to the curvature at room temperature. Figure 4-11 and Figure 4-12 show the calculated and experimental values of the curvature change as a function of temperature for both Pyrex™ and Hoya SD-2™ glasses. The curvature change goes to zero as the temperature increases to the bonding temperature, 300°C. This proves

Pyrex™ and Hoya SD-2 ™ bonded to Si elastically deform since the sample had no curvature during bonding at 300°C. Therefore, 300°C is the stress free bonding temperature. The curves are non-linear because of the ΔTCE between the materials. Since CVD SiC is a brittle material like Si, it will also exhibit linear elastic deformation.
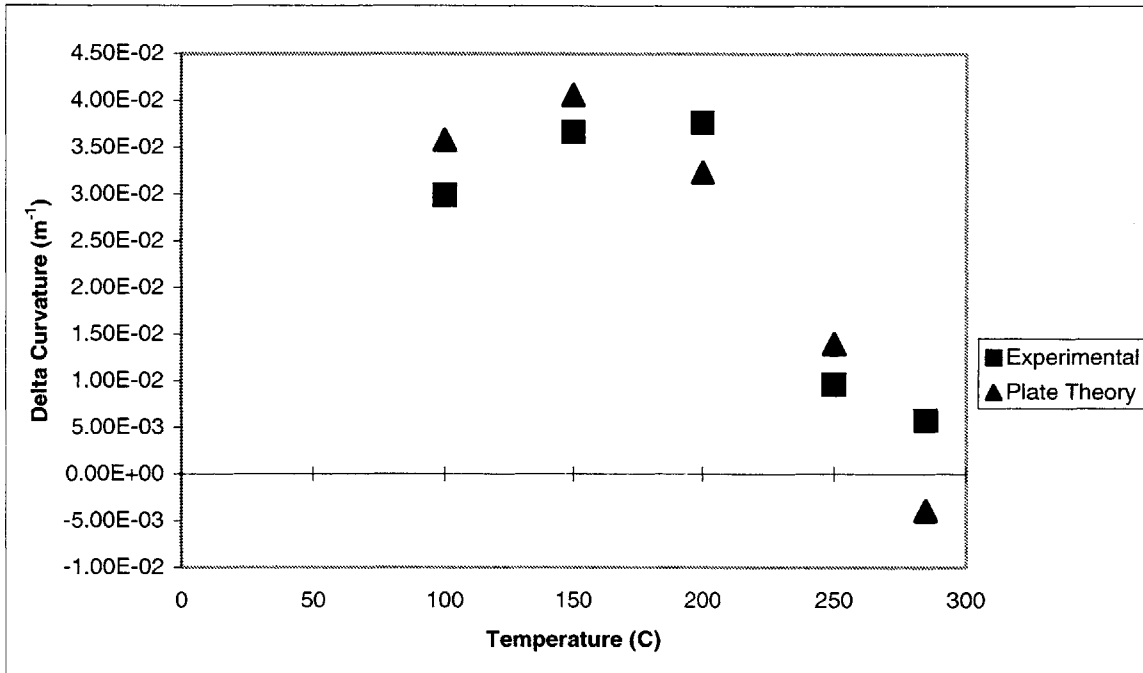
Figure 4-11: Delta K of Pyrex™/Si as a function of Temperature
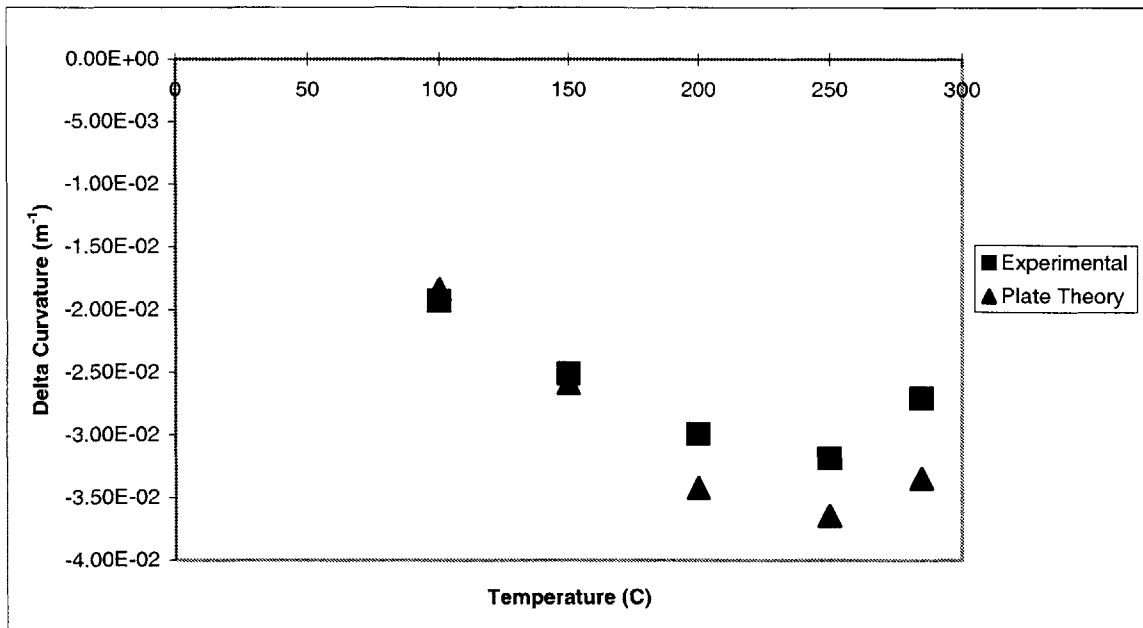
Figure 4-12: Delta K of Hoya SD-2^{TM}/Si as a function of Temperature

Second, the curvature values of each experiment calculated from plate theory, ANSYSv.6.0 modeling, and the Tencor measurements are shown in Figure 4-13. The K_{tencor} error bar range does not fall within $K_{Plate\_Theory}(+)$ and (-) bars because K_{tencor} not only carries the error from the bonding operation, but also error from the laser scans. The accumulation of sodium at the top of the die size samples made it difficult for the laser to read the actual curvature. Bonded Pyrex^{TM} to Si at -330°C showed the largest range of K_{tencor} values because there was the largest amount of sodium oxide on the top of the Pyrex^{TM} glass. The low aspect ratio of the plate theory calculation did not affect the difference in K_{ANSYS} curvature predictions using the actual bimaterial dimensions. K_{ANSYS} values fall within the K_{Plate_Theory} error bars.

The overall difference in the K_{Plate_Theory}, K_{tencor}, and K_{ANSYS} values between all the experiments is minimal. It shows that all the materials have a similar ΔTCE at the low bonding temperatures, so the residual stress is minimal. More specifically, the curvature values of Pyrex^{TM} to Si at ΔT=-330°C (Exp. 1 Part 1) compared to Pyrex^{TM} to CVD SiC at ΔT=-330°C (Exp. 2 Part 1) are comparable, and indicate no significant difference. This proves that bonding CVD SiC to glass is very promising. Using CVD SiC as a packaging material bonded to these glasses will induce a minimal amount of residual stress. Therefore, the amount of relaxation, and long-term degradation and instability in MEMS devices will be minimized versus current packaging techniques.
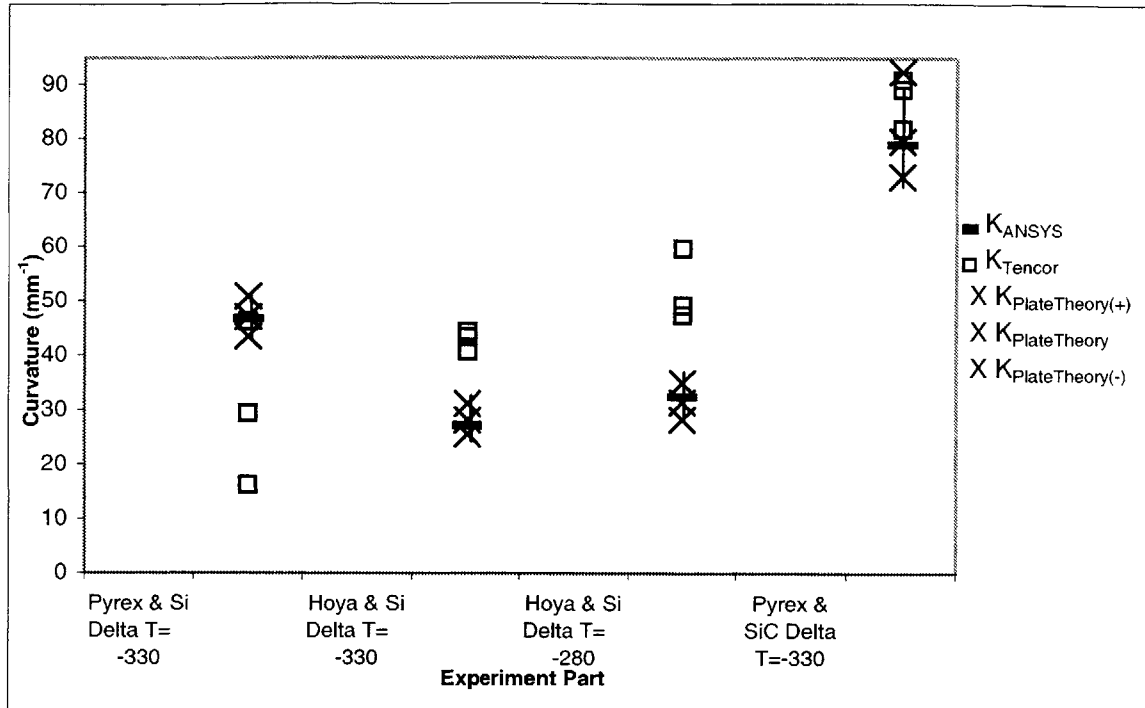
Figure 4-13: Curvature Values from Experiments 1 and 2

4.2.5 TEM and STEM/XEDS Chemical Results

The two main objectives in analyzing the anodically bonded interface and depletion layers were achieved. Using TEM, sample cross sections were ion-beam thinned to electron transparency and imaged with 200keV electrons to look for contrast evidence of depletion layer(s) in the glass and determine the composition of the glass/Si or CVD SiC interface. Using STEM/XEDS , a chemical analysis of the glass depletion layers was completed by scanning the sample with an electron beam and measuring X-ray emission from each element present.

All TEM images showed evidence of a layer of different mass density or scattering power near the interface of Pyrex™ /Si and Hoya SD-2 ™ /Si. Each depletion layer shown on the micrograph is defined by a darkline inserted for clarity. Xing et al. [13] recently found multiple layers in Pyrex™/Si interfaces, but only one was observed in this Pyrex™ study. Two layers were found near the Hoya SD-2™/Si interface . These layers are shown in Figure 4-14 and Figure

4-15. The 1μm width of the layer found in the Pyrex[TM] near the glass/Si interface is approximately three times larger than the 290nm layer width found in the Hoya SD-2[TM] near the glass/Si interface. A second, smaller, layer found in the Hoya SD-2[TM] near the glass/Si interface was approximately 60nm wide. These Pyrex[TM]/Si and Hoya SD-2[TM]/Si anodically bonded interfaces were highly planar with no evident nanoscale voids or defects. The glass layer, found immediately adjacent and parallel to the glass/Si anodic bonded interface, was less electron-dense. The decrease in electron scattering can be attributed to sodium depletion in Pyrex[TM] and to zinc or magnesium depletion in Hoya SD2[TM].
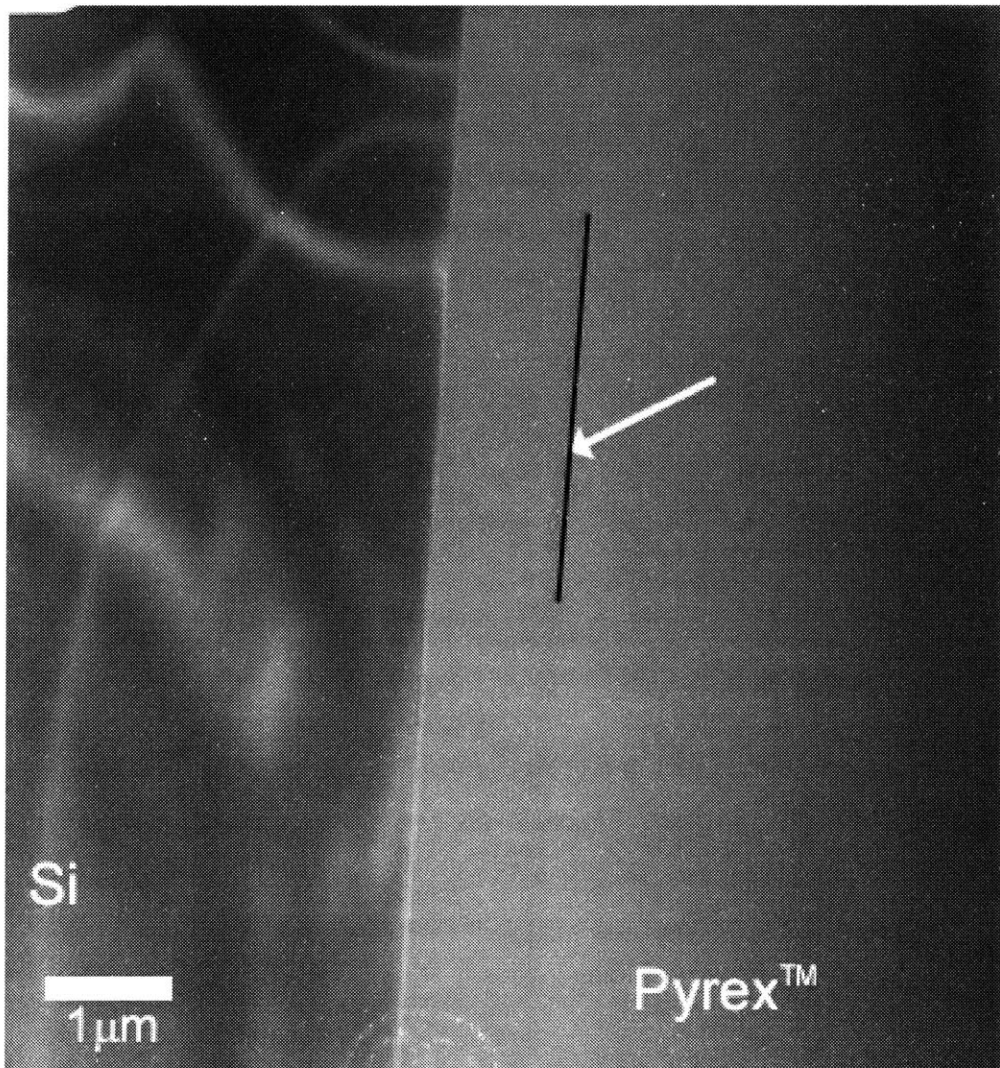
Figure 4-14: TEM Picture of Pyrex[TM]/Si Layer
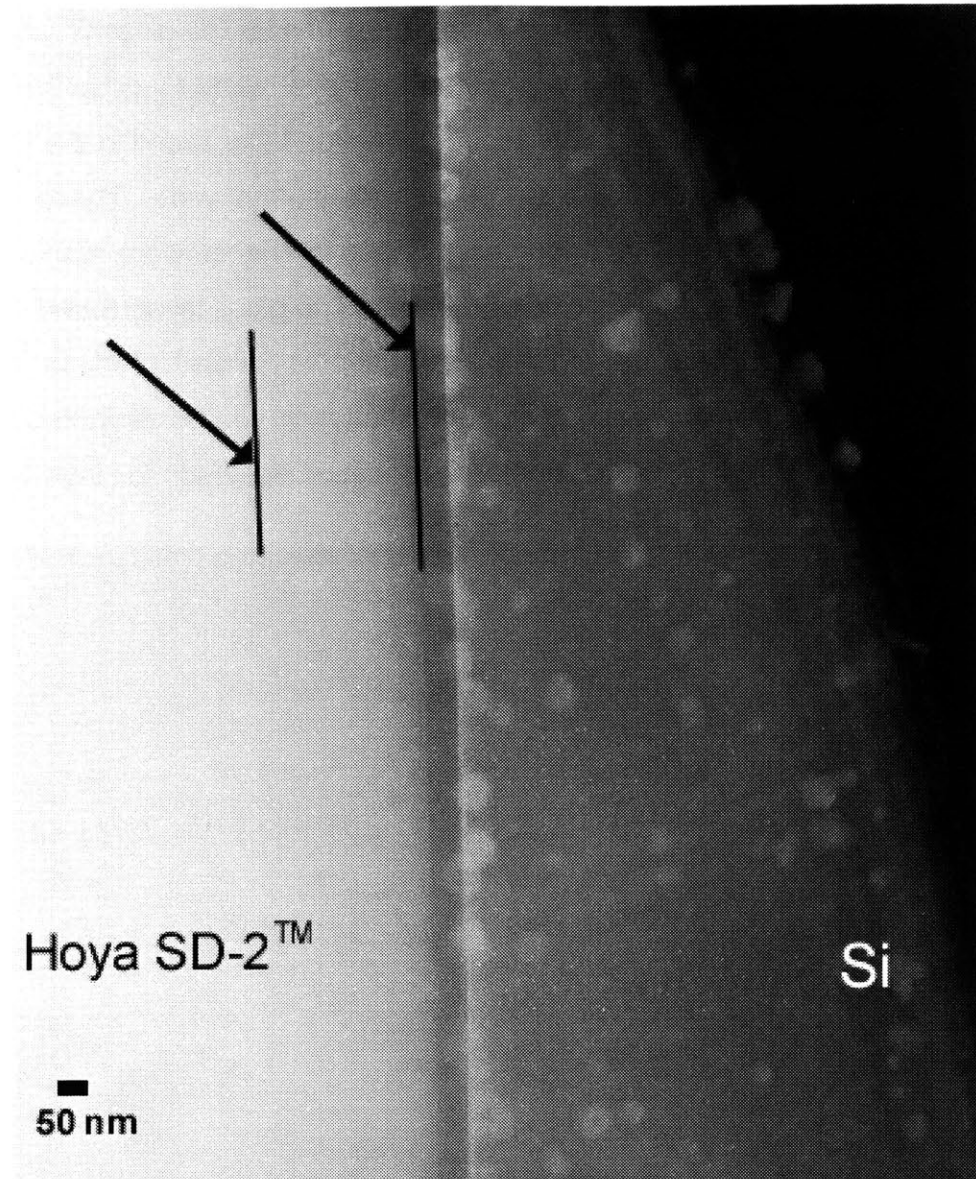
Figure 4-15: TEM Picture of Hoya SD-2^{TM}/Si Layers

TEM was also used to look at the Pyrex^{TM}/CVD SiC interface. The features of the Pyrex^{TM}/CVD SiC interface, Figure 4-16, are different from features of the Pyrex^{TM}/Si interface, Figure 4-14 . The Pyrex^{TM}/CVD SiC interface is very irregular. These interfacial features suggest that oxidation occurred at the interface during bonding.
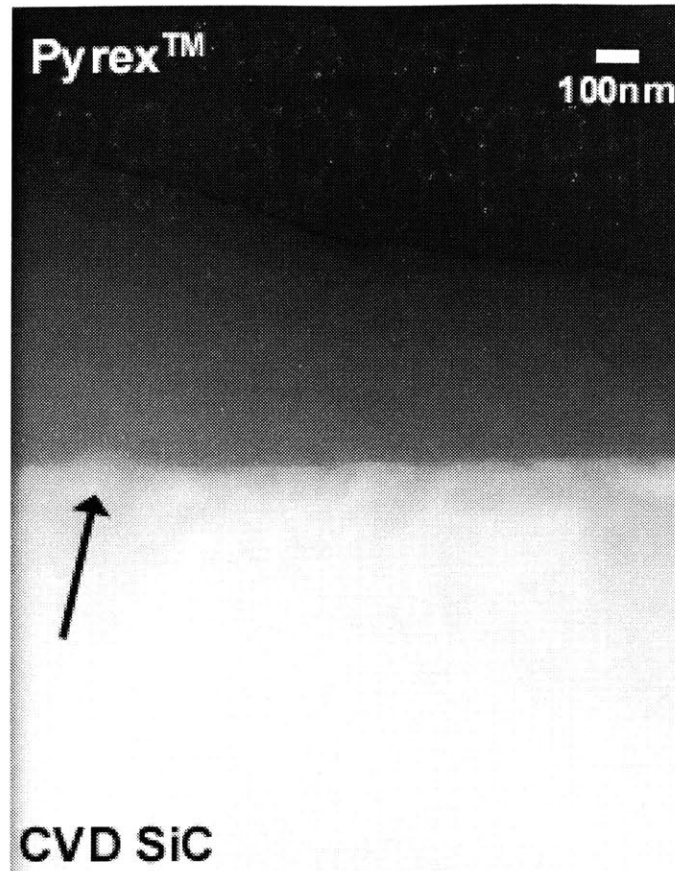
Figure 4-16: TEM Image of Pyrex™/CVD SiC Interfacial Features

Figure 4-17 from the STEM analysis also shows evidence of a depletion layer at the Pyrex™/CVD SiC interface. The width of the depletion layer near the Pyrex™/CVD SiC interface was larger (1.25μm) than the one that formed near the Pyrex™/Si interface, (1.0μm). These observations suggests that a different type of phenomenon is involved in bonding glass to CVD SiC compared to Si. There was no difference in contact angles on a hydrophilic versus hydrophobic CVD SiC surface. This may imply that the native oxide on the CVD SiC surface does not provide enough available Si bonds to establish these surfaces. If there are insufficient Si bonds available, then the oxygen anions at the interface, established during the anodic bonding process, may not have many Si atoms to bond to. The bonding mechanism may compensate for this unavailability by establishing a larger depletion layer.
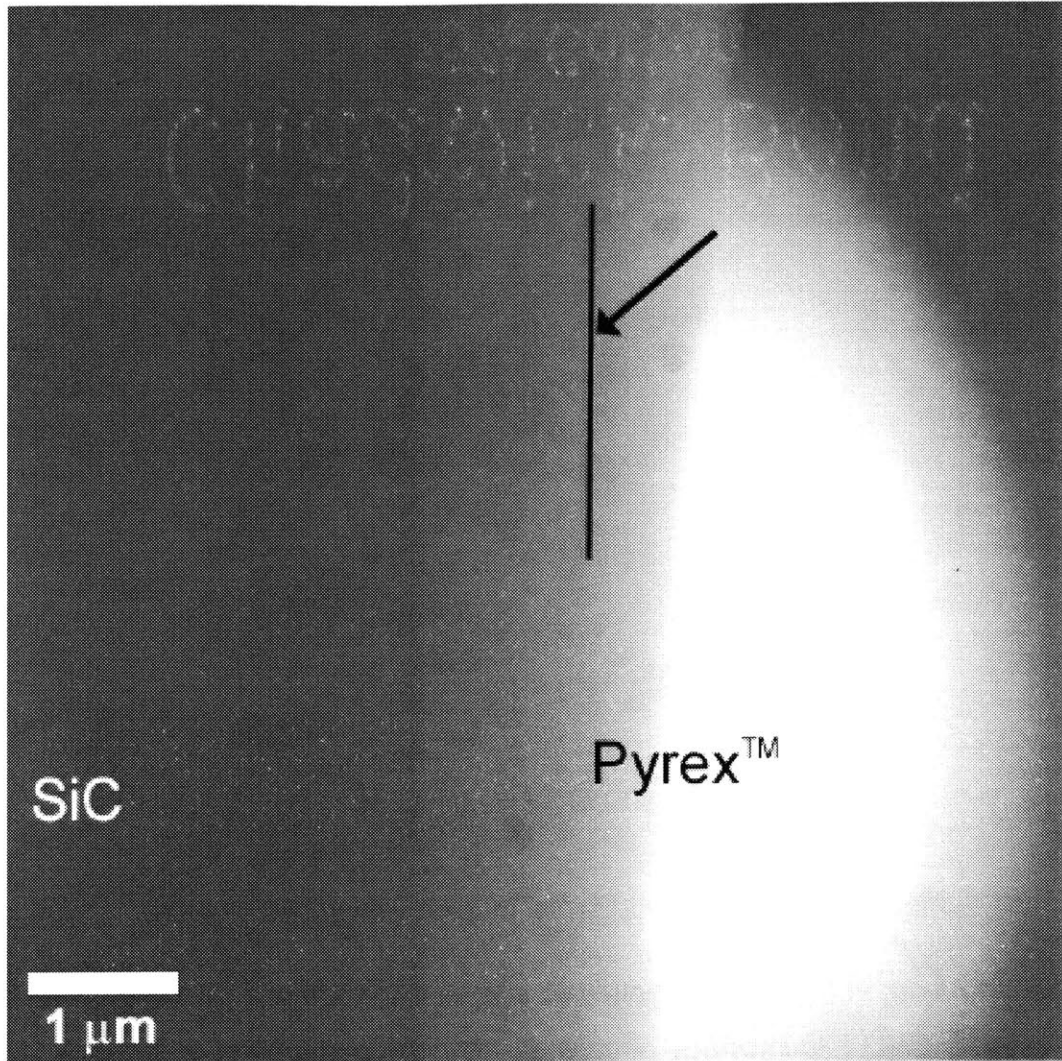
Figure 4-17: STEM Picture of Pyrex™/CVD SiC Layer

Plots of current vs. time show differences in bonding current behavior between Pyrex™ bonding to Si and Pyrex™ bonding to SiC. Albaugh [12] related the area under the initial current peak to the amount of charge that leaves the depletion layer. If this relationship is assumed, then Figure 4-18 suggests that the rate of current change in bonding these materials at 1000V, 350°C, and 20 minutes can be related to the depletion layer width in Figure 4-14 and Figure 4-17.

The area under the current vs. time plot, Figure 4-18, is larger for Pyrex™/CVD SiC than for Pyrex™/Si; therefore, more charge must be leaving the depletion layer during the bonding of Pyrex™ to SiC. Since more charge is leaving, the

depletion layer in the Pyrex™ glass should be larger when bonding to SiC. The TEM and STEM pictures, Figure 4-14 and Figure 4-17, show that this is the case. The depletion layer width of Pyrex™/Si is approximately 1 μm, which is smaller than the approximate 1.25μm depletion layer width of Pyrex™/CVD SiC. These data suggest that the current profile and the depletion layer are related. More charge must be diffusing into the CVD SiC lattice in order to form the bond, creating a larger depletion layer.
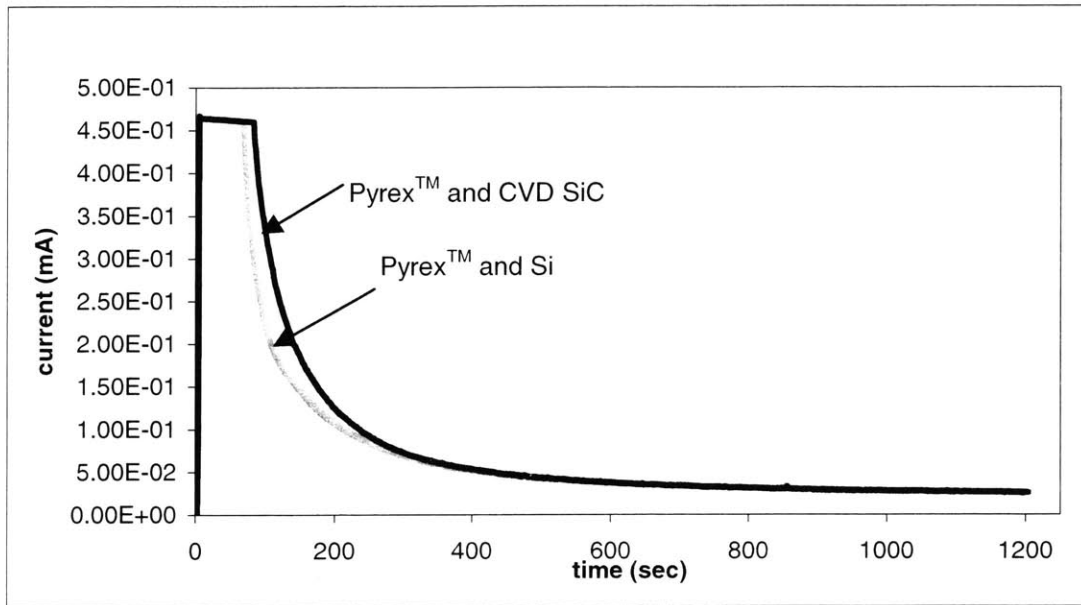
Figure 4-18: Current - time Profiles for Pyrex™ bonded to Si and CVD SiC

The STEM/ XEDS chemical analysis provides evidence for chemical depletion being associated with the observed layers of lower electron scattering. The HOYA SD2™ glass bonded to Si exhibits two distinct depletion layers, while the Pyrex™ bonded to Si shows only one band. Depletion of different elements integral to the glass were followed. Tables 26 and 27 show the composition of the Pyrex™ borosilicate glass and HOYA SD2™ Zn-aluminosilicate glass.

Table 26: Measured Pyrex™ Composition by XPS [41]

Compound	Pyrex™ (Mol %)
SiO_2	80.8
B_2O_3	12.0
Na_2O	4.2
Al_2O_3	2.0
K_2O	0.6
MgO	0.2
CaO	0.2

Table 27: Measured Hoya SD-2™ Composition[26]

Compound	Hoya SD-2™ (Mol %)
SiO_2	25-70
B_2O_3	1-5
Na_2O	1-5
Al_2O_3	20-30
MgO	2-5
ZnO	10-20
As_2O_3	1-5

In the chemical analysis STEM data, each element has been ratioed to Si, e.g. sodium/silicon (Na/Si), on the ordinate. The x-axis shows the distance in micrometers scanned, which was established from the number of pixels scanned. The ordinate shows the counts associated with the X-ray emission from the element measured.

Figure 4-19 shows the depletion behavior in the HOYA SD2™ glass sample corresponding to Figure 4-15. The STEM/XEDS scan began in the Si and reached the Si/HOYA SD2™ interface at 66nm. There is a large percentage change in the magnesium (Mg) content in the Si before reaching the Si/glass interface; therefore Mg is soluble in Si. From the Si/glass interface into the glass, there are several distinct elemental depletion regions. The first 60nm depletion layer is likely the depletion of Mg and aluminum (Al). The second depletion layer of Figure 4-15 has a width 290nm. Figure 4-19 shows this second depletion layer approximately begins at 130nm and ends at 420nm. The STEM/XEDS scan of this second depletion layer shows a real depletion of several elements: Mg, Na, and zinc (Zn). Al decreases monotonically within the second depletion layer until it becomes constant, along with the other elements, in the bulk glass. From

[26] Hoya Corporation, Glass Substrates for Silicon Sensors, CA, USA

114

420nm to the end of the scan, the elemental concentrations reach their constant values in the bulk glass. These results are unlike Visser et al.'s [20] findings. Visser et al. [20] found the only participants in the anodic bonding mechanism with HOYA SD2™ and Si were Na and Zn.
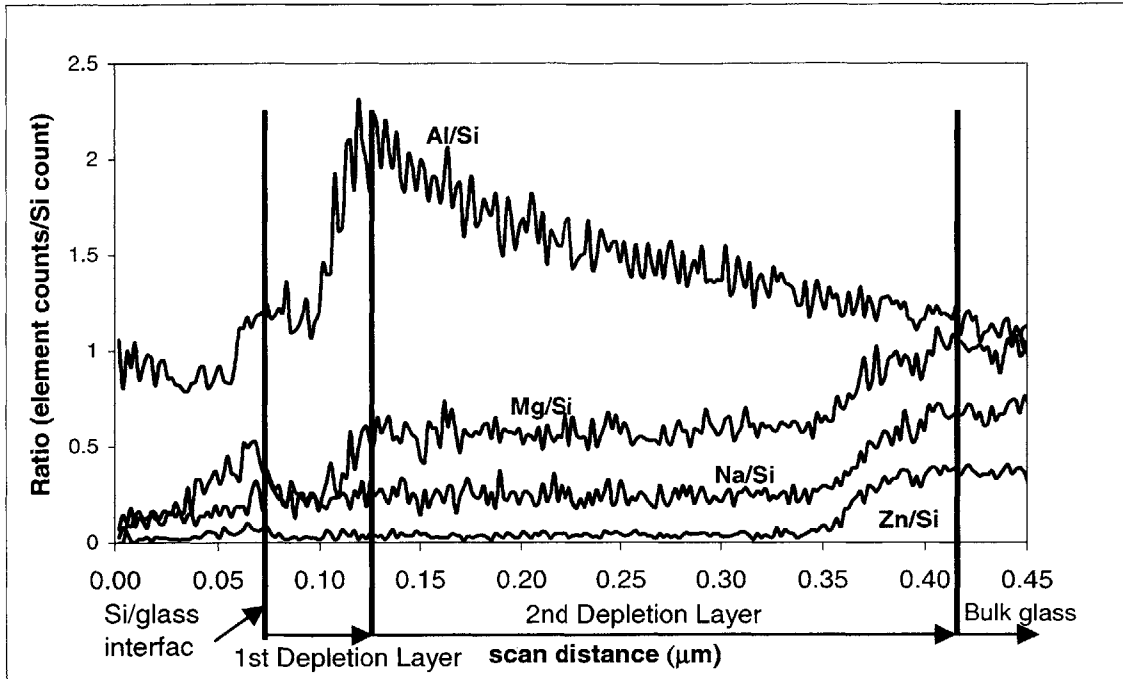
Figure 4-19: Ratio of Key Elements of Hoya SD-2™ to Silicon

Figure 4-14 shows a distinct depletion layer reaching from the Si/ Pyrex™ interface into the bulk glass. The STEM/XEDS analysis in Figure 4-20 and Figure 4-21 also reveal a layer depleted of several elements. The depletion layer is depleted of Al, Mg, and Na, as shown in Figure 4-20. The slopes of the Al, Mg, and Na X-ray signals over this layer are initially, steep, and then modestly increase into the bulk glass, indicating depletion. Figure 4-21 also shows a very likely depletion of potassium (K) and Ca (calcium) over the 1μm depletion layer for the same reason. Na should have a very distinct depletion in Pyrex™, as Visser et. al [20] found, but the detection of it using STEM/XEDS analysis is difficult, since the electron beam easily redistributes it. The K depletion agrees with Visser et al. [20], as they also found that Na and K ions play an important role in the anodic bonding mechanism. The depletion of Al, K, and Ca agrees

with Nitzsche et al.'s [6] results in Tempax™ glass, which has a very similar composition to Pyrex™. Overall, this study of the Pyrex™ depletion layer shows that several elements, Al, Mg, Na, K, and Ca, participate in the depletion mechanism, and some have more distinguishable depletion layers than others.
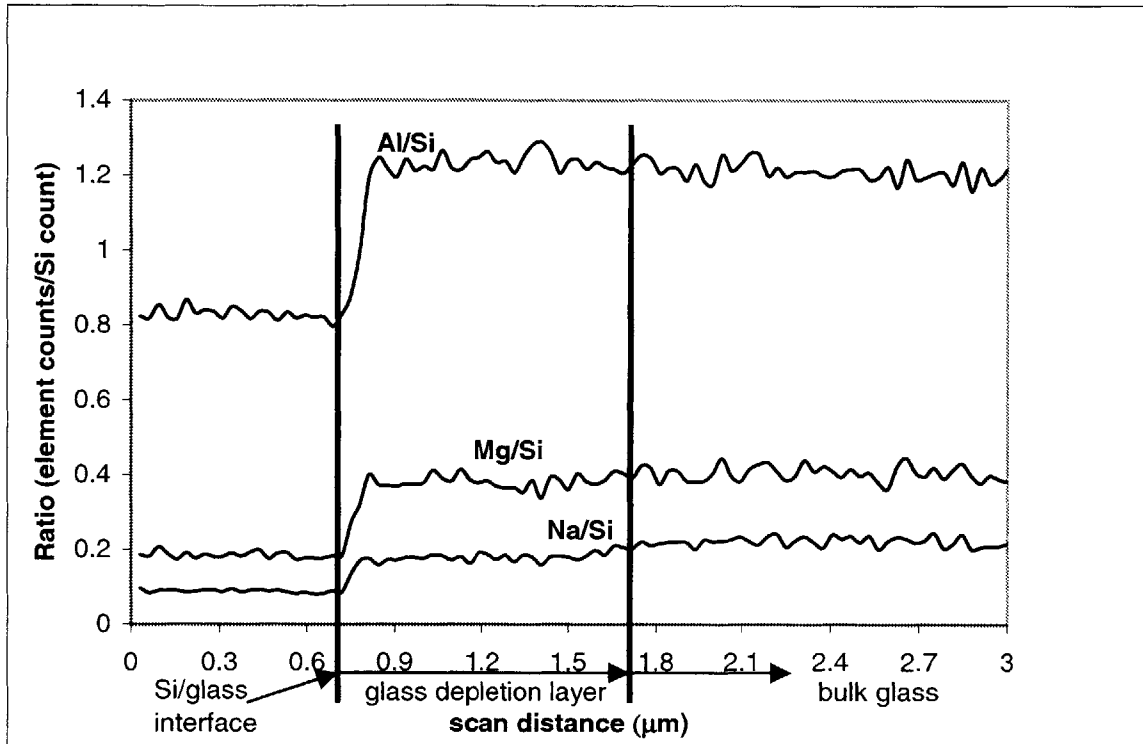
Figure 4-20: Ratio of Key Elements of Pyrex™ Glass to Silicon Part 1
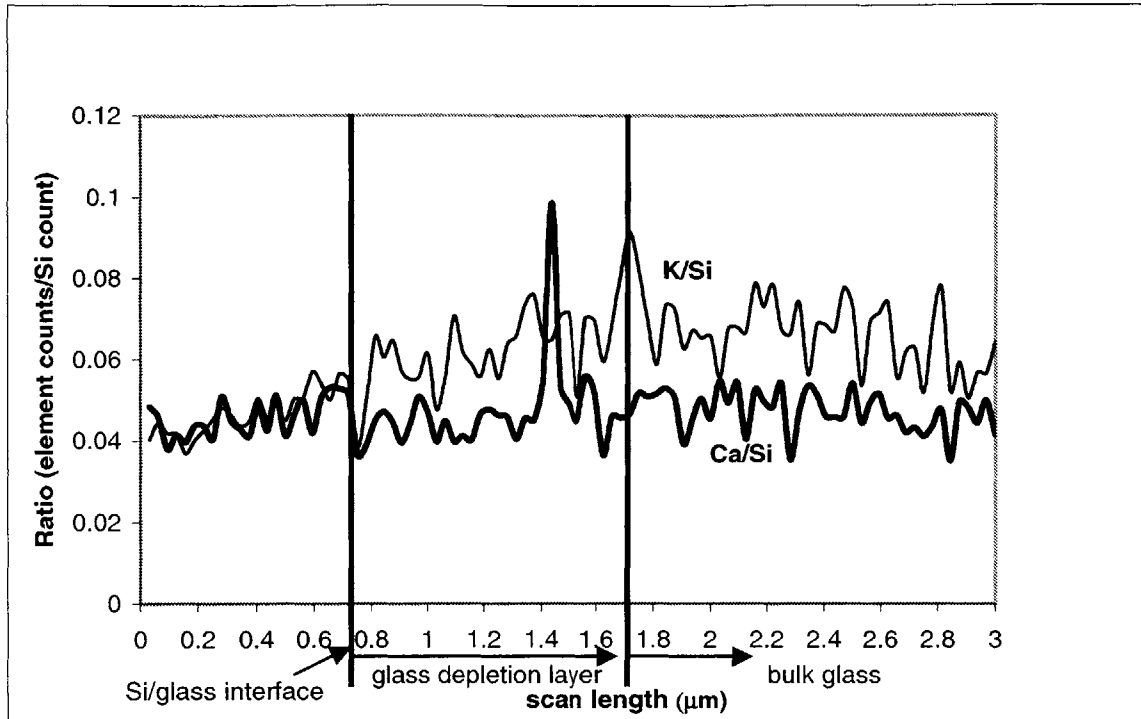
Figure 4-21: Ratio of Key Elements of Pyrex™ Glass to Silicon Part 2

These TEM/STEM analyses show that HOYA SD2™ exhibits a distinct difference in anodic bonding mechanism compared to Pyrex™ glass. STEM/XEDS also shows a difference in interfacial bonding and depletion layer width between the Pyrex™ bonded to Si and CVD SiC. In each glass, many more elements create depletion layers than previously found by other authors. The diffusion of several elements is significant within the network of the amorphous glass composed of many different compounds. Once the voltage is applied, several cation species diffuse toward the cathode creating depletion layers in the network. The network reconstructs because of the depletion of these diffusing elements. The oxygen anions in the network probably diffuse toward the interface and seek to bond with the positively charged Si or CVD SiC surface. It is believed that the oxygen will bond to any available Si dangling bonds of native oxide established on the Si or CVD SiC surface. Since the local neutrality around the sodium, magnesium, or aluminum cations in Pyrex™ glass is disturbed because of their diffusion to the negatively charged cathode, the network most likely seeks stability in the

reconstruction process by allowing the oxygen to move toward positively charged Si or CVD SiC surfaces.

Overall, this study demonstrates the reason why chemical analysis needs to be performed in order to understand the modeling of the anodic bonding mechanism. It indicates a significant amount of information about the nature of the glass and interface during the bonding mechanism.

Chapter 5
Anodic Bonding of Thin-Film Glass to Silicon and CVD Silicon Carbide

This chapter details the thin-film fabrication and bonding procedures of sputtered Pyrex™ and lapped glass, and bond quality from acoustic microscope images.

5.1 Experimental Procedure

The sputtered Pyrex™ and the lapped glass samples were prepared in a Class 100 cleanroom. Both samples were bonded in the open lab using the same anodic bonding equipment as bulk glass anodic bonding. The following experimental procedures describe the sputtered and lapped thin-film glass processes.

5.1.1 Sputtered Pyrex™ Glass Procedure

First, the sputtered glass samples were prepared. Sputtering HOYA SD-2™ glass is a non-standard process, so it was difficult to sputter, and too risky to explore. Therefore, sputtered Pyrex™ glass was used for this study. Glass thickness, and bonding voltages and temperatures were used as process monitor variables.

4" double-sided polished p-type, Si wafers with 20 mil thickness were cleaned in a 20 minute Piranha immersion, and spin-dried. A 500nm +/- 50nm thermal oxide layer was grown at 1100°C on both sides of the Si wafer. A Shipley 1822 resist was coated on one side of the Si wafer, in order to etch the oxide on the backside with a Buffered HF (BHF) dip. The resist was stripped using a 7 minute 1:1 H_2SO_4:H_2O_2 dip. The single-sided oxide, p-type Si wafers were outsourced to Thin Film Concepts for sputter deposition. Approximately, 1.5 μm of Pyrex™ glass was sputtered on top of the oxide. The sputtered Pyrex™ glass wafers from Thin Film Concepts were annealed at 550°C for 2 hours in a nitrogen environment and cleaned. A photolithography step using the Plaza Test Mask,

similar to the bulk glass procedure, was performed. The Plaza test structures on the sputtered Pyrex™ were etched using a 7:1 BHF dip. The etch rates of non-annealed and annealed sputtered Pyrex™ versus bulk Pyrex™ glass were explored since the sputtering process and the annealing step affect the final glass composition. The DEKTAK 3STv.2.12 measured the distance etched at different times in order to obtain the target (0.2μm) etch depth. Since the annealed sputtered Pyrex™ has a higher etch rate, as shown in Table 28, a shorter etch time was required. This new etch rate was used to etch the 0.2μm depth.

Table 28: Etch Rates of Annealed vs. Non-Annealed Sputtered Pyrex™

Sample	Time (min)	Distance (μ)	Etch Rate (μ/min)
Non-annealed Sputtered Pyrex™	7	1.563	0.223
Annealed Sputtered Pyrex™	7	0.237	0.034
Bulk Pyrex™	8.33	0.2	0.024

Finally, the sputtered glass wafers were diced into 18mm x 12mm die size samples, and anodically bonded to another Si sample following the same bonding procedure as for the bulk glass. The Si-sputtered Pyrex™ glass piece was placed on top of a bulk p-type Si sample on the anodic bonder. Figure 5-1 shows a side view of a fabricated thin-film sputtered Pyrex™ glass sample being anodically bonded to p-type Si.
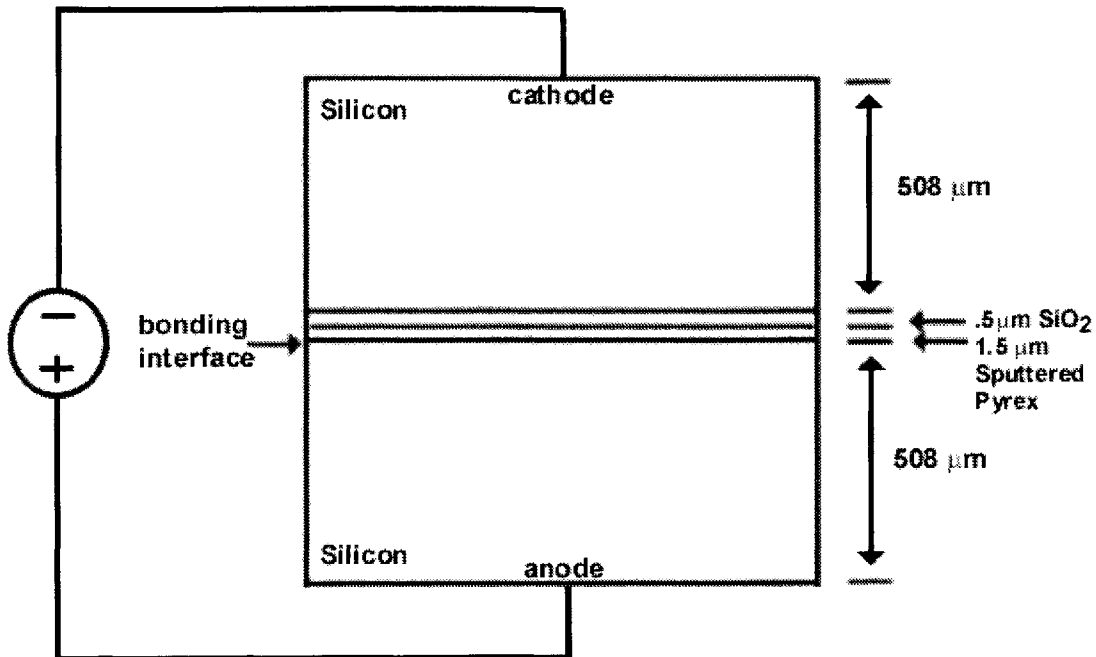
Figure 5-1: Anodic Bonding of Sputtered Pyrex ™ Glass to Silicon

A table of bonding conditions was not established until samples bonded successfully. Several tests were performed at lower voltages, 30-100V, temperature of 350°C, and a time of 10 minutes, but bonding Si/sputtered Pyrex™ to Si was not successful over the entire die.

5.1.2 Lapped Glass Procedure

Next, lapped glass anodic bonding was explored because a thin-layer of glass can be produced by lapping it. This process was advantageous because both Pyrex™ and Hoya SD-2™ glasses could be lapped. The following procedure describes the detailed fabrication process. A drop gauge measured the thickness at the center, top, and bottom of each bulk 4" 30 mil Pyrex™, and 20 mil Hoya SD-2™ and p-type Si wafers. Both glass and p-type Si wafers were cleaned using the standard pre-anodic full wafer bond procedure. A 30 second 1:1 Piranha solution, DI rinse, IPA spray, DI rinse, and N_2 dry cleaned the glass wafers, and a 10 minute 1:1 Piranha solution, DI rinse, 1 minute 1:1 HF:H_2O, DI rinse, and N_2 dry cleaned the Si wafers. Using the EV501 Wafer Bonder, glass to Si wafers were anodically bonded for 1 hour in a N_2 vacuum at 300°C and 970V. The bonded wafer pairs were cooled, and outsourced to Valley Design for

lapping. The bonded wafer pair was mounted, the bow squeezed out, and the top Pyrex™ and Hoya SD-2™ glass wafers were polished or lapped to a final thickness. A drop gauge measured the lapped glass thickness at different areas on the wafer. Pyrex™ glass was lapped to approximately 10 μm +/- 5 μm, and Hoya SD-2™ glass was lapped to approximately 20μm +/- 10 μm. The lapped glass underwent a photolithography step using the Plaza Test Mask, similar to the bulk and sputtered glass procedures. A 7:1 BHF dip etched the lapped Pyrex™, and a 20:1 NH_4F:HF dip etched the lapped HOYA SD-2™. The etch depths were measured using the DEKTAK 3STv.2.12. The lapped glass had similar etch rates as the bulk glass. Finally, the lapped glass wafers and Si wafers were diced and applied to the anodic bonder using the same bonding procedure as for the bulk glass. Figure 5-2 shows a side view of a fabricated Si-lapped glass sample being anodically bonded to p-type Si.
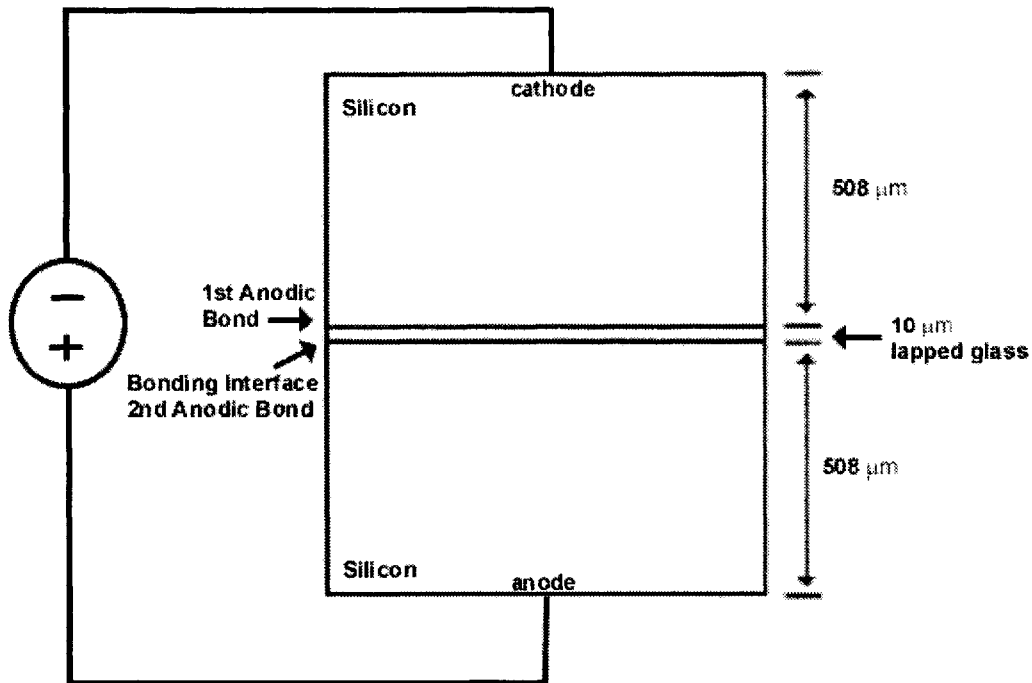
Figure 5-2: Anodic Bonding of Lapped Glass to Silicon

A table of bonding conditions was not established until the lapped glass-Si successfully bonded to another bulk Si piece using different voltages 30-100V, and a constant 350°C and 10 minutes. These bonding results were successful.

Both the time and voltage was increased in order to see if the partially bonded areas of the Plaza Test structures increased. The bonded Si-lapped glass to Si and CVD SiC samples were outsourced to Sonoscan™ for the acoustic microscopy bond quality assessment. A C-Mode Scanning Acoustic Microscope, C-SAM™, with a 230 MHz center frequency transducer and 0.25" focal length was used to image the samples

5.2 Results and Discussion

Sputtered Pyrex™ glass did not bond to p-type Si at 100V, 350°C, and 10 minutes. The applied voltage was too high and caused dielectric breakdown. A lower voltage of 20V using 350°C and 10 minutes was applied to the sample, but bonding still did not occur. Bonding was unsuccessful because most of the voltage was, most likely, being distributed on the SiO_2 layer instead of the sputtered Pyrex™. Therefore, the SiO_2 needed to be shorted by sputtering a gold layer on the Si- SiO_2 –sputtered Pyrex™. Unfortunately, the samples still did not bond to Si at 20V-50V, 350°C, 10 - 20 minutes. The sputtered Pyrex™ glass was probably depleted of the essential elements, i.e. sodium, or the voltage was still breaking down the glass. Therefore, sputtered Pyrex™ glass was considered too risky to bond, so the lapped glass process was explored. Thin-film evaporated glass was not attempted because of the dearth of resources and experimentation performed in this new area.

The lapped glass process has several advantages: a SiO_2 layer was not needed, the final glass composition had etch rates comparable to bulk glass, and both Pyrex™ and HOYA SD-2™ glasses were lapped into a thin layer on Si. The target thickness was 10 μm because it needed to be larger than the depletion layer thickness, and the lapping procedure produced a non-uniform surface. Full wafer glass to Si anodic bonds were achieved using 300°C, so this lower temperature would not significantly change the near interface region of the final lapped glass thickness. Voltage and time varied with temperature fixed at 350°C. 350°C (versus 300°C) was chosen as the die size bonding temperature because

a higher temperature allowed for better bond quality. Samples successfully bonded at these conditions. It should be noted that bonding the other side of the glass a second time can cause detrimental effects at the bonded interface. Figure 5-3 shows the difference of the three cases: regular bulk glass to Si anodic bonding, Visser et al.'s [20] reverse polarity anodic bonding, and the lapped glass to Si anodic bond. Visser et al. [20] discovered that reversing the polarity (Si is negatively charged and the glass is positively charged) caused debonding and defects at the bulk glass/Si interface. Part 2 of Figure 5-3 shows the effect of reverse polarity on the bonded interface. The cations, such as Na^+, move back to the interface bond, accumulate, and can cause debonding. Part 3 of Figure 5-3 shows what could occur when bonding lapped glass a second time. The cations, such as Na^+, could move to the initial bulk bonded interface, accumulate, and cause debonding.
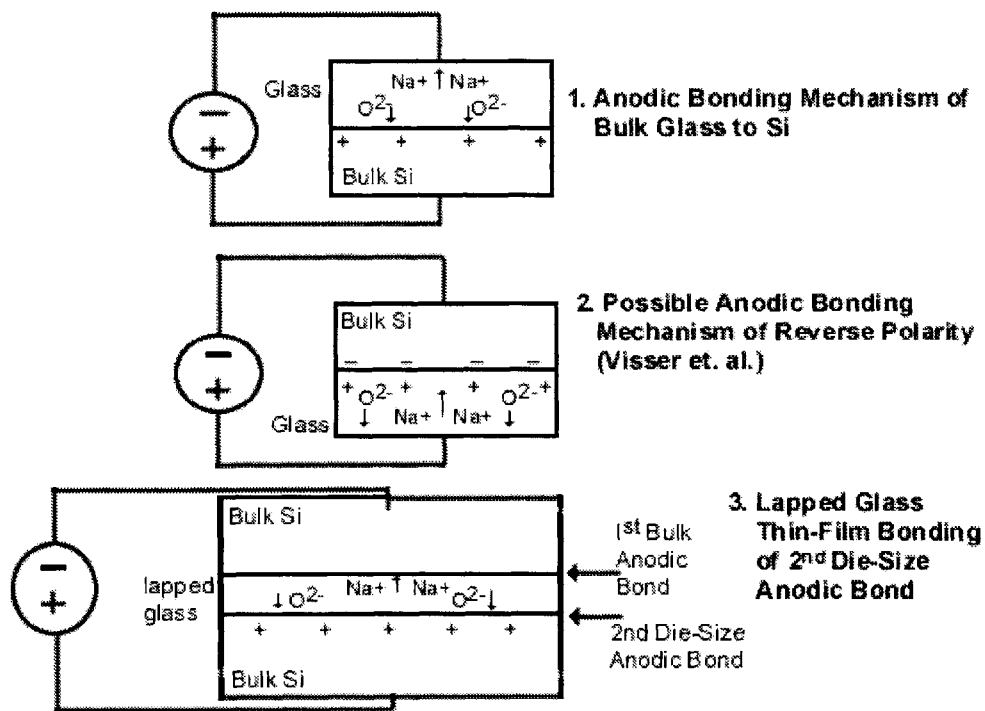
Figure 5-3: Difference of Bonding Bulk Glass to Lapped Glass using Reverse Polarity

An acoustic microscope was used to obtain the bond quality of the Plaza Test structures in order to determine if the second anodic bond caused debonding of

the initial bulk anodic bond. The following describes the acoustic microscopy analysis.

A full description of the procedures was dictated by [42]. A summary is provided here. The sample receives pulses of ultrasound generated from the acoustic microscope's transducer. The pulses of ultrasound travel through the coupling medium (distilled water), and into the sample. Some of the ultrasound is reflected back to the sending transducer and some is transmitted further into the part when reaching a boundary or interface between two materials. If the ultrasound encounters an air gap (void), all of the ultrasound is reflected back to the sending transducer. The A-Scan images show the reflected signals or echoes from the entire part. The distance between the echoes is related to the material thickness by the ultrasonic velocity in that material. As the transducer scans over the part, the electronic gate can be set to collect only the echoes from a particular interface/depth in the sample which allows for level-specific images to be created. The darker areas on the images show bonds, and the bright white, irregular areas show voids or unbonded areas.

The difference in material properties between glass and Si is small, so they have a similar acoustic impedance (Z). Silicon has an acoustic impedance of approximately 20 Ns/m^3, glass has a value of approximately 15, and air $\approx$ 0. At the interface with another material, the difference between the acoustic impedances affects the reflected echo signal: Z_1 is the acoustic impedance of the first material at an interface and Z_2 is the acoustic impedance of the second material. The reflected echo, R, is calculated in Equation 5.1.

$$R = \frac{(Z_2 - Z_1)}{(Z_2 + Z_1)}$$

(5.1)

The calculated reflection coefficient R from echoes reflected at interfaces using these materials is:

silicon to glass: (15 - 20) / (15 + 20) = -0.14

glass to silicon: $(20 - 15) / (20 + 15) = +0.14$
silicon to air: $(0\ \ - 20) / (0\ \ + 20) = - 1.0$

Positive reflection coefficient R values indicates a positive echo when the central peak appears above the center line, whereas negative reflection coefficient R values indicates a negative echo when the central peak will appear below the center time axis [42]. So, the change in amplitude of the echo from a bonded to disbonded interfacial region is very distinct on the acoustic image.

Two acoustic images through the Si and CVD SiC surfaces of the lapped glass sandwich were taken: the image through the Si of the first bulk anodic bond at 970V, 300°C, and 1 hour, and the image through the Si or CVD SiC of the second die size anodic bond using different bonding conditions. A side view of the lapped sample, Figure 5-4, indicates where each bond is defined, and when the etched Plaza Test Mask is bonded.
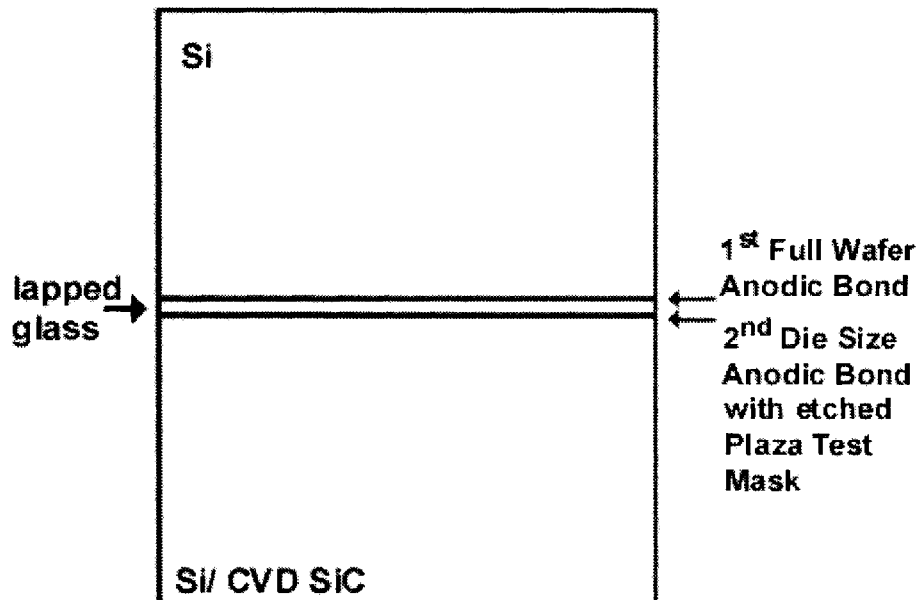
Figure 5-4: Side View of Lapped Sample

The lapped Pyrex^{TM} glass-Si bonded interface of the first full wafer anodic bond was imaged on a die size sample before bonding the opposite side of the glass to bulk Si. Figure 5-5 shows the scan through the Si. There are no bonded structures at this interface during the first bulk wafer bond to Si, so discrete voids

are not present in this acoustic image. Therefore, this interface bond is a uniform and complete bond. The bright color gray indicates that an amplified echo was used to show tiny details of the bonded interface. The fringes on the borders indicate possible transducer interaction with the materials [42].
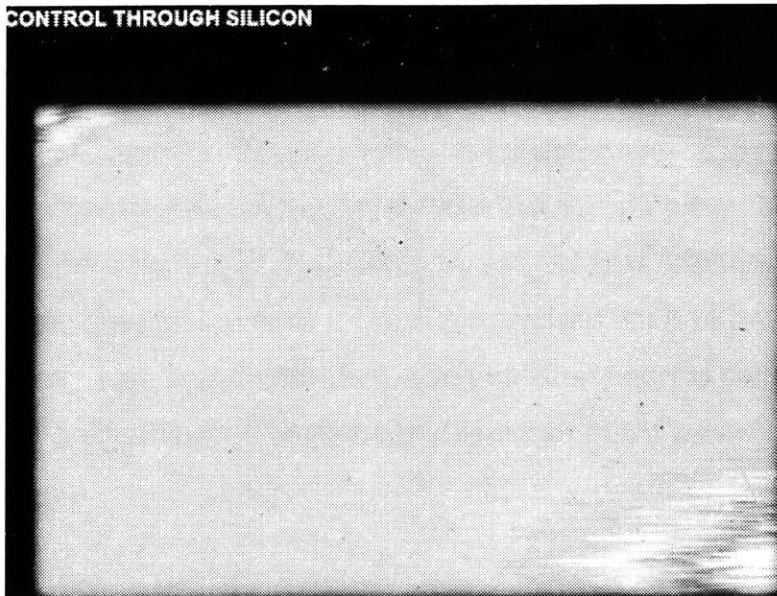
Figure 5-5: Image of First Pyrex^{TM}-Si Bulk Anodic Bond

The first Si- lapped Pyrex^{TM}-Si samples were bonded at 50V and 100V, at 350°C and 10 minutes. Both Si sides of the sample were A-scanned. From these scanned images, the results shown in Figure 5-6 of the 50V-350°C-10 minute sample, showed a clearer image of the partially bonded Plaza Test structures. Figure 5-6 shows an A-scan through the Si of the first, full wafer anodic bond. A waveform was applied to this first anodic bond in order to distinguish between unbonded and bonded regions, and to examine if reverse polarity affected the first anodic bond. The waveform, shown in Figure 5-6, is labeled in three parts: #1 shows the echo reflected from the center, irregular area of this sample, #2 shows the echo reflected from a bonded structure, and #3 shows a echo reflected from a void or unbonded region. Figure 5-6 also shows a small change in echo shape between the bonded and disbonded areas of this sample. The disbonded area at #3 has a "V" shape formed from a small positive lobe on either side of a larger negative center peak [42]. The bonded areas are clearly shown

by the dark areas of the rectangular structures. The bonded area by #2 and throughout the bottom of the axis of Figure 5-6 has a "W" shape formed by two large negative peaks and a large positive peak joining them together [42]. The two negative peaks forming the "W" are possibly from the difference between the top and bottom of the bonded rectangular structures. The irregular area of #1 and throughout the axis of the sample is different because it does not have a clear "V" or "W" echo shape. It has an in-between shape consisting of a higher center positive peak, and a smaller negative echo in the bonded structure [42]. This odd-shaped echo could have formed for one possible reason. The interfaces between the bulk Si- lapped glass- bulk Si are separated by a very thin 10μm glass layer, and the thickness is uneven from the lapping process. Therefore, the two echoes reflecting from both interfaces, each defined by a width in time, are very close together and interfere by overlapping as a single echo [42].
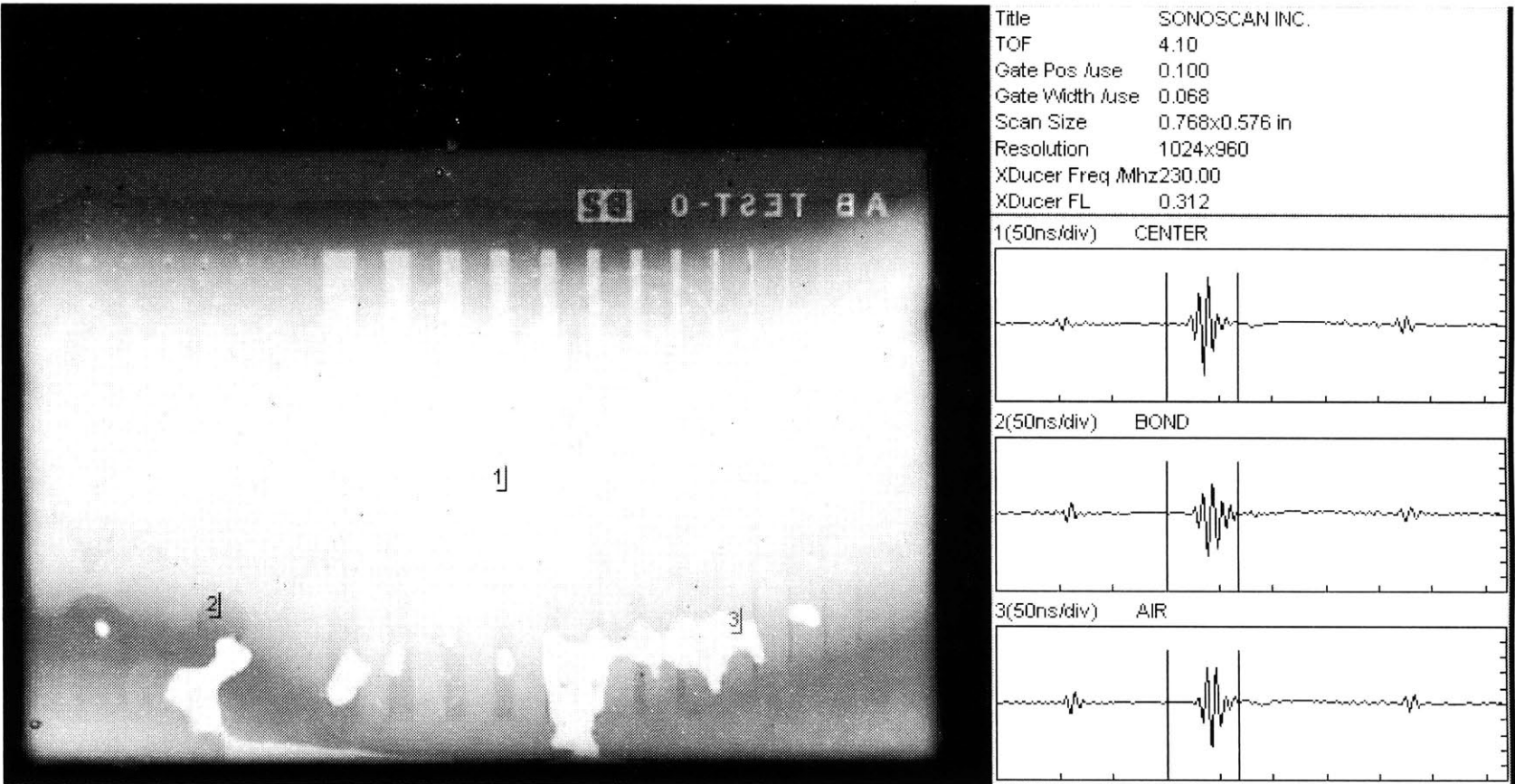
Figure 5-6: Waveform of 1st Full Wafer Anodic Bond of Si-Pyrex™ of Sample 1

Figure 5-7 shows an image of the second die size anodic bond of the same sample #1 (shown in Figure 5-6). Bonded versus unbonded structure regions are still distinguishable. The same areas of unbonded features are also shown in Figure 5-6. There cannot be straight-through holes of these unbonded features in the lapped glass between interfaces. This proves that since the glass layer is so thin, it is difficult to tell if this first full anodic bond of Figure 5-6 is debonding because of the applied bonding conditions used to form the second die size bond.
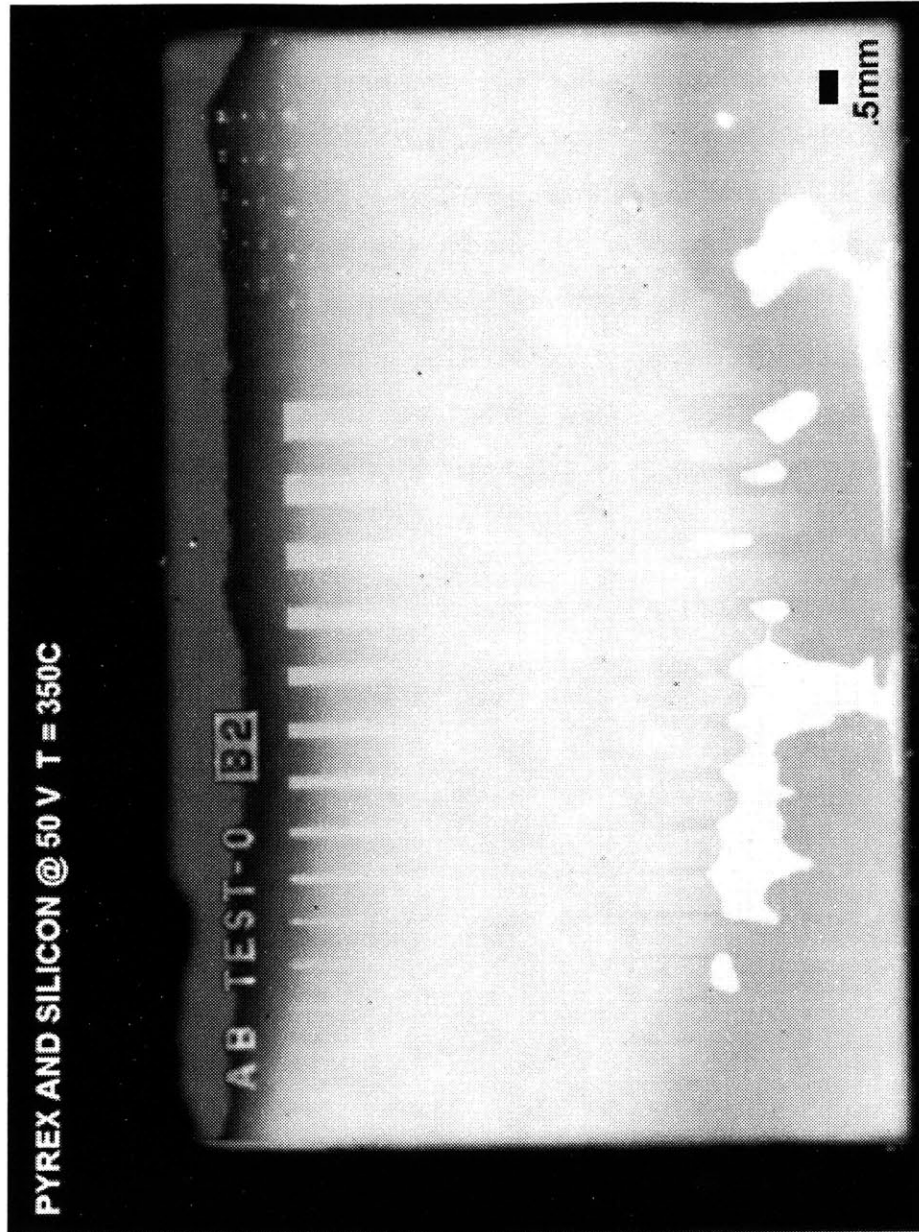
Figure 5-7: Image of Die Size Anodic Bond of Sample #1

Since acoustic microscopy was unsuccessful in determining if the second anodic bond affected the first full wafer anodic bond, the effect of the bonding conditions on the second die size bond quality were studied. Therefore, only images of the second die size anodic bond are shown.

Several more samples were bonded under conditions ranging from 30-100V, 10-20 minutes, and 350°C in order to observe an increase in bonded structure area.

The sample bonded at 350°C, 80V, and 20 minutes gave clear acoustic imaging results without showing an irregular echo encompassing a significant portion of the die. Figure 5-8 shows that the bonded area of the structures increased when a longer time of 20 minutes and higher voltage of 80V was used for bonding. The darker gray areas could have formed because of the change in material composition or density. The elemental composition of the glass is most likely changing since certain elements are depleted in the anodic bonding mechanism. When the voltage and temperature are applied, the cations in the lapped glass involved in the mechanism, i.e. Na^+, could be moving and changing the density of the glass.
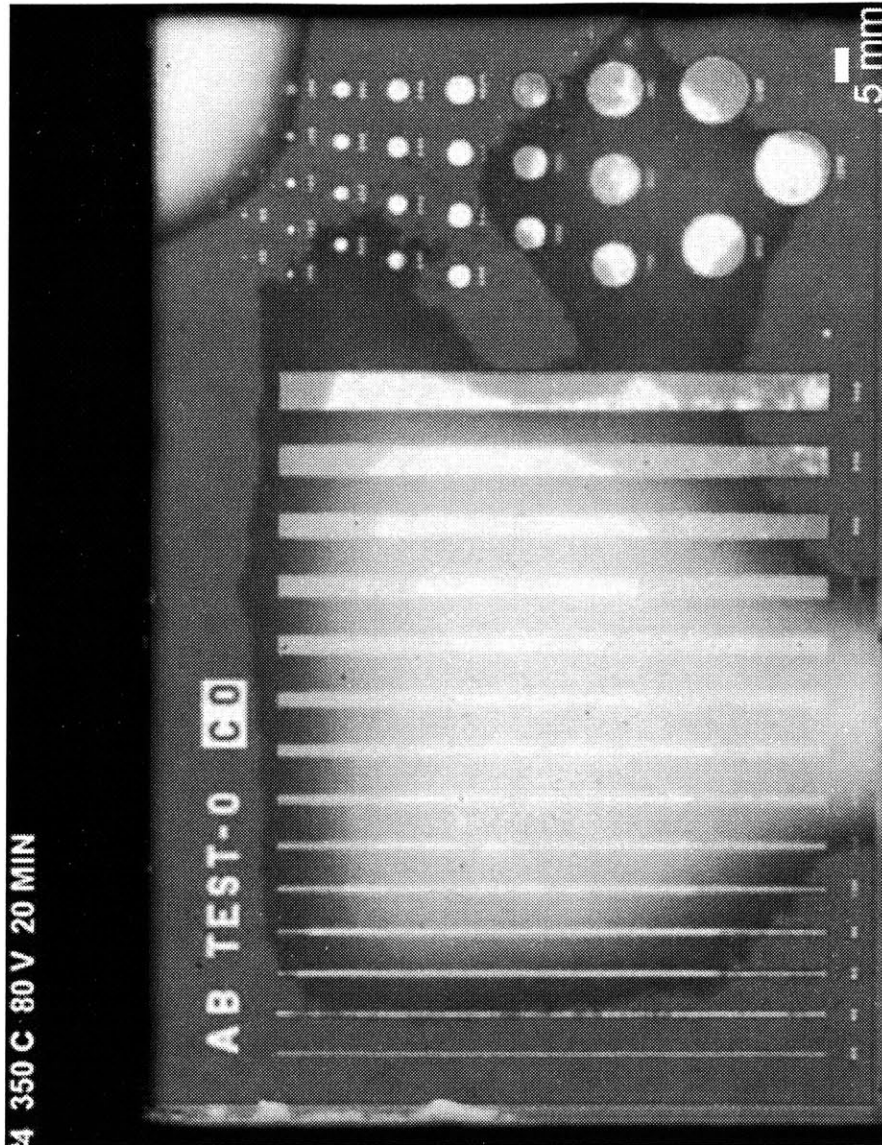
Figure 5-8: Sample #2 Die Size Bond at 350°C, 80V, and 20 min.

The 3rd sample bonded at 350°C, 80V, and 45 minutes produced discouraging results because the acoustic image showed several irregular echoes. It was difficult to determine if the bonded area of the structures increased with longer bonding time.

Finally, CVD SiC was bonded to Si-lapped Pyrex^{TM}. Since 350°C and 80V gave the most promising results for the bonding of Si and Pyrex^{TM}, these same bonding conditions were used. Experiments using 20 minutes and 45 minutes were repeated and the 45 minute bonding condition resulted in an increased area

of bonded structure. The bond quality assessment of Si-lapped Pyrex™ to CVD SiC gave more promising results because irregular echoes did not form. Figure 5-9 shows that there is also a distinct, darker color found between the structures. This again, could be due to a change in density of the glass resulting from a compositional change of the elements due to the voltage and temperature.
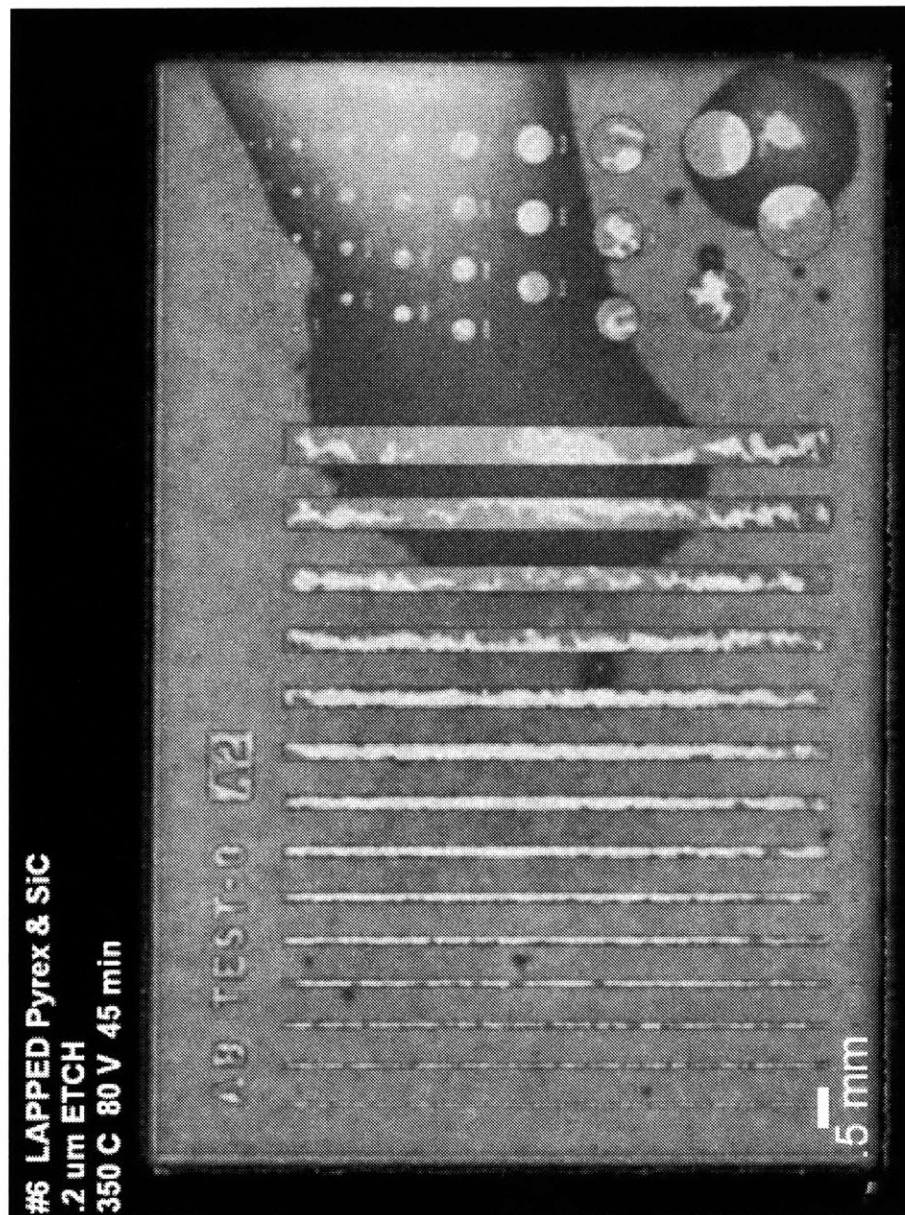
Figure 5-9: Sample of Si-Lapped Pyrex™ to CVD SiC Bonded at 350°C, 80V, and 45 min

Bonding Si- lapped Hoya SD-2^{TM} to Si and CVD SiC was also successful. The following figures show the acoustic images from this analysis. Si- lapped Hoya SD-2^{TM} was bonded to Si at 350°C, 80V, and 20 minutes. Figure 5-10 shows irregular echoes occurring, but there is still partial bonding of the structures. Bonding Si- lapped Hoya SD-2^{TM} to CVD SiC at 350°C/80V/ 20 proved unsuccessful because the sample broke before it was imaged. Another sample bonded at 350°C, 80V, and 45 minutes was imaged, but the acoustic microscopy image was very unclear.
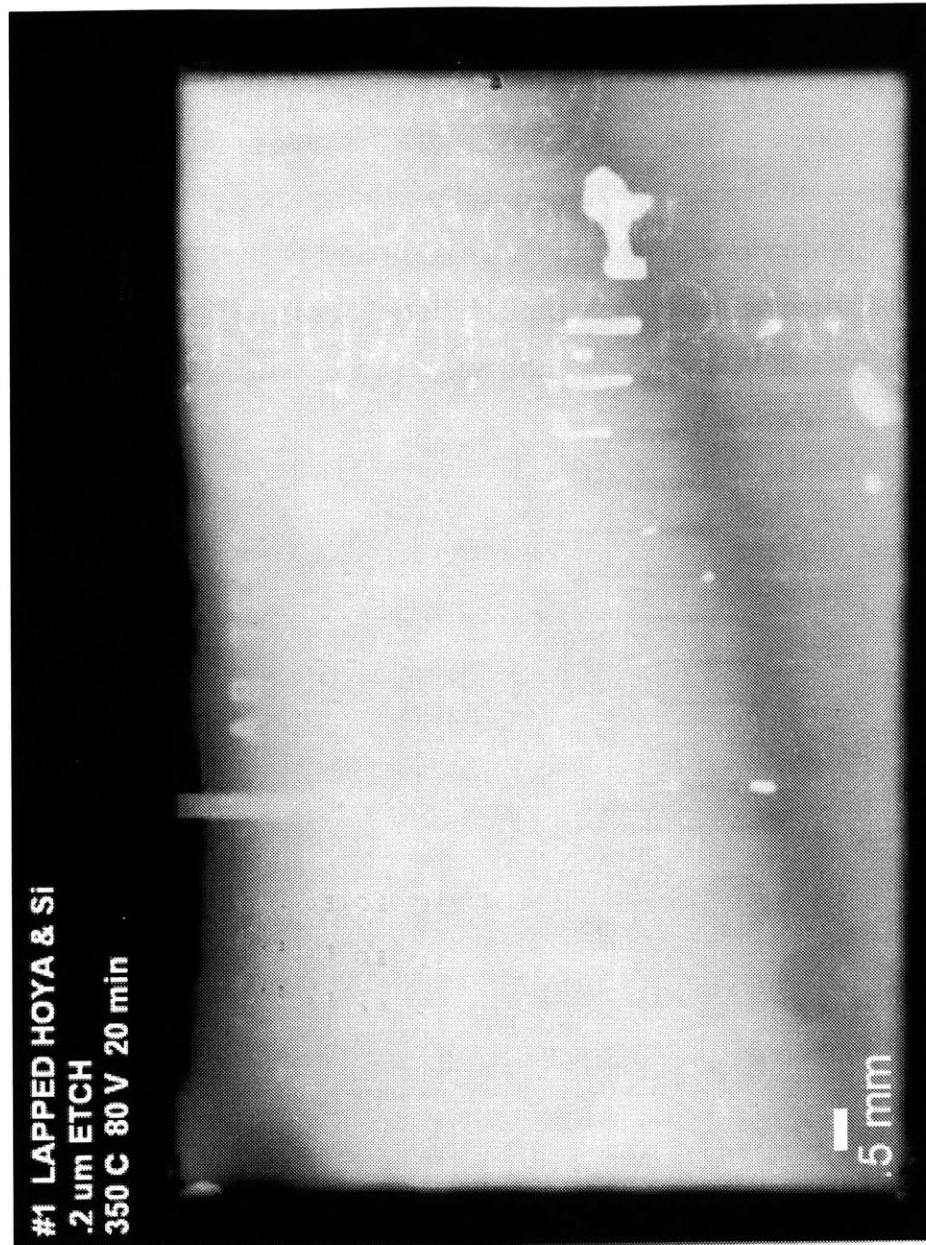
Figure 5-10: Sample of Si-Lapped Hoya SD-2™ to Si Bonded at 350°C, 80V, and 20 min

Overall, the acoustic microscopy analysis did not provide a reliable measure of bond quality as a function of the reverse voltage on the double-bonded specimens. However, the second die size bond quality of the Plaza Test structures was successful. These experiments demonstrated that an increase in time and voltage increased the bonded area. The mechanism behind this improvement is unclear. One possible reason could be an increase in diffusion

at the interface. The bonding of the structures is also very random, since areas of the structures bond at different locations. This could also occur because of diffusion, and/or the effect of the bonding conditions of the second die size bond.

[THIS PAGE INTENTIONALLY LEFT BLANK]

Chapter 6
Conclusions and Recommendations for Future Work

6.1 Conclusions

This thesis has examined the process technology, materials, science, and mechanics of anodic bonding. Each examination area has produced several key conclusions.

1. Hydrophilic and hydrophobic surfaces on the Si and CVD SiC bonded to glass were not found to be a significant factor in the anodic bonding process because there was no difference in bonded structures and current versus time.

2. A new, low temperature process was established to bond bulk and lapped Hoya SD2^{TM} and Pyrex^{TM} to SiC which has never been done prior to this work. It was found that the SiC RMS surface roughness of less than 45nm is required for a successful process.

3. A two-part model for bonding the Plaza Test structures was developed and tested. The Plaza Test structures showed evidence of elastic deformation during bonding. The overall model was found to be capable of reasonably predicting which structures contact and bond. More structures were predicted to contact, but did not remain bonded when the voltage and temperature were removed. Therefore, the bonding mechanism is the limiting factor to which structures remain bonded on the Plaza Test sample. Finally, the bond toughness was not correctly predicted using ANSYSv.6.0, so refinement to the overall model is necessary.

4. Microscopy and chemical analyses confirmed the depletion of multiple species. It was found that the diffusion of a particular species is a function of the composition of the glass.

5. The induced thermoelastic residual stress was tested and found to be minimal between the glass to Si and CVD SiC, which is very advantageous for device performance.

6. Si-sputtered Pyrex thin-film glass did not bond successfully to Si or CVD SiC because of the change in composition of the sputtered glass versus bulk glass, or the applied voltage broke down the thin film. Si- lapped Pyrex™ and Hoya SD-2™ glasses were fabricated and successfully bonded to Si and CVD SiC. The acoustic microscopy results did not give reliable bond quality results because of the very thin-layer used and the limits of the microscope.

From all these key tests and results, it is shown that anodically bonding CVD SiC to glass is as advantageous as bonding Si to glass and represents a promising packaging technology.

6.2 Recommendations for Future Work

The anodic bonding mechanism is complex, and future work is needed to fully understand how two surfaces form a bond. Si to Si anodic bonding using thin-film glass is also very advantageous, but it is a new process, and bond quality analysis must be explored before it can be considered reliable. The following recommendations outline the approach needed for future experimental and modeling work.

The bonding model must be refined. A full electrostatic and elastic model should replace the parallel plate capacitor. Both elastic deformation and diffusion need to be coupled in the model. The role of voltage, temperature, time, surface chemistry, etch depth, and roughness must be studied during contact and bonding. A fine nodal mesh around the etch depth in the finite element analysis will give more accurate toughness values near the edge of the width. Since the experimental crack lengths are all similar, they would probably converge to a

similar toughness value. As noted in Section 4.2.3, the boundary conditions on the overall model should be changed. The fixed x- and y- boundary conditions on each side of the model prevents rigid motion that should result from the interfacial bonding of the structures. Therefore, the y-direction must be left unconstrained on both sides, and the x-direction can be constrained on one side and the other side must have a constant value in order to account for the transverse strain effect. The boundary conditions of the 500μm nodal surfaces on the sides of the Plaza Test structure must be analyzed in order to predict how these will deform when the voltage is applied during bonding and when it is removed. Mode 1 (tensile) bonding was assumed, but mixed mode, including mode II (shear) bonding, should be accounted for in the modeling analysis since a bimaterial is bonded at the interface.

The toughness calculations do not determine the overall quality of the bond, so other shock, hermeticity, vibration tests etc. must be done. Not only will toughness values help better understand the anodic bonding process, but also chemical analysis. Since the TEM and STEM/XEDS images and analysis gave successful results, it is recommended these techniques be used to study the role of surface chemistry. SIMS (Secondary Ion Mass Spectrometry) is also recommended to give an even more sensitive depth profiling of the molecular structure and depletion layer(s). This analysis would determine if hydrophilic surfaces increase bond toughness. Future STEM/XEDS work will require better TEM samples more uniformly thin across the CVD SiC to glass interface, so that chemical analysis can be more reliable and compared for glass bonded to Si.

Potential delamination of the lapped glass interface can occur. Another analysis technique must be used to distinguish the two interface bonds. Acoustic microscopy using fourier analysis as a function of frequency instead of time could possibly decipher the differences between the echoes from each interface in the frequency, not time, domain. However, devoting more time and experimentation to e-beam deposition anodic bonding should be pursued and characterized using

the Plaza Test Mask and different bonding conditions because it is a more promising method.

Finally, bulk glass-to-SiC anodic bonding must be put into practice for actual MEMS devices.

Chapter 7 Appendix

7.1 ANSYSv.6.0 input

```
!*Si_bond.mac
!* This program finds the stiffness,k,
!*constant of bonded glass to Si.  A 2-D
!*model of the front view of a Plaza Test
!*Mask Structure with the etch depth is
!*built.  The same pressure is applied to
!*the glass surface on the etch depth and
!*the Si surface on the opposite to
!*simulate bonding.  The deformation of
!*each surface simulating bonded is
!*added to see if it equals the etch depth.
!*If it does, then the force is calculated
!*from the pressure, and divided by the
!*deformation of each material to get each
!*material's k constant. The same program
!*is used to bond glass with CVD SiC, but
!*with different dimensions.
/PREP7
multipro,'start',8
*cset,1,3,ht,'Enter Rectangle Height',762e-6
*cset,4,6,etch,'Enter Etch Depth',.2e-6
*cset,7,9,len1,'Enter Middle Rectangle
Length',600e-6
*cset,10,12,len2,'Enter Side Rectangle
Length',500e-6
*cset,13,15,Siht,'Enter Si Height',508e-6
*cset,16,18,Young,'Enter Youngs
Modulous',86.8e9
*cset,19,21,poiss,'Enter Poisson's Ratio',.244
*cset,22,24,press,'Enter Pressure (positive is
ok)',1e6
*cset,61,62,'Enter at your own risk!!!!!'
multipro,'end'
!* Geometry
RECTNG,0,len2,0,ht,
RECTNG,len2,len2+len1,etch,ht-etch,
RECTNG,len2+len1,2*len2+len1,0,ht,
RECTNG,0,2*len2+len1,-Siht,0,
!* Structure
/NOPR
/PMETH,OFF,0
KEYW,PR_SET,1
KEYW,PR_STRUC,1
KEYW,PR_THERM,0
KEYW,PR_FLUID,0
KEYW,PR_MULTI,0
!*
FLST,2,4,5,ORDE,2
FITEM,2,1
FITEM,2,-4
AGLUE,P51X
!* Plane Strain
ET,1,PLANE82
!*
KEYOPT,1,3,2
KEYOPT,1,5,0
KEYOPT,1,6,0
!* Material Properties
MPTEMP,,,,,,,,
MPTEMP,1,0
MPDATA,EX,1,,Young
MPDATA,PRXY,1,,poiss
!*
MPTEMP,,,,,,,,
MPTEMP,1,0
MPDATA,EX,2,,130e9
MPDATA,PRXY,2,,.279
!* Mesh: Line Spacing
FLST,5,18,4,ORDE,6
FITEM,5,1
FITEM,5,3
FITEM,5,-11
FITEM,5,13
FITEM,5,17
FITEM,5,-23
CM,_Y,LINE
LSEL, , , ,P51X
CM,_Y1,LINE
CMSEL,,_Y
!*
LESIZE,_Y1,30e-6, , , , , , ,1
!*
LPLOT
TYPE,  1
MAT,   1
REAL,
ESYS,    0
SECNUM,
!*
MSHAPE,0,2D
MSHKEY,0
!*
FLST,5,3,5,ORDE,3
FITEM,5,2
FITEM,5,5
FITEM,5,7
```

```
CM,_Y,AREA
ASEL, , , ,P51X
CM,_Y1,AREA
CHKMSH,'AREA'
CMSEL,S,_Y
!*
AMESH,_Y1
!*
CMDELE,_Y
CMDELE,_Y1
CMDELE,_Y2
!*
TYPE,  1
MAT,     2
REAL,
ESYS,    0
SECNUM,
!*
CM,_Y,AREA
ASEL, , , ,     6
CM,_Y1,AREA
CHKMSH,'AREA'
CMSEL,S,_Y
!*
AMESH,_Y1
!*
CMDELE,_Y
CMDELE,_Y1
CMDELE,_Y2
!*
/UI,MESH,OFF
!* Boundary Conditions
FLST,2,4,4,ORDE,4
FITEM,2,4
FITEM,2,10
```

```
FITEM,2,19
FITEM,2,21
!*
DL,P51X, ,ALL,0
!*
FLST,2,1,4,ORDE,1
FITEM,2,5
!* Apply Pressure Load
SFL,P51X,PRES,-1*abs(press),
FLST,2,1,4,ORDE,1
FITEM,2,20
!*
SFL,P51X,PRES,-1*abs(press),
!*
FINISH
/SOLU
/STATUS,SOLU
SOLVE
FINISH
/POST1
/EFACE,1
AVPRIN,0, ,
!* Output Plots
PLNSOL,U,Y,2,
/WAIT, 5
ASEL,S,MAT,,1
ALLSEL,BELOW,AREA
/REPLOT
/WAIT,5
ASEL,S,MAT,,2
ALLSEL,BELOW,AREA
/REPLOT
/WAIT,5
!* End of Program
```

```
!*SE_1_1_600_1_2_bond.mac
!* This program finds the strain
!*  energies of the all the nodes of
!*  bonded glass to
!* Si.  A 2-D symmetric model of the front
!*view of a Plaza Test structure with the
!*etch depth is  built.  The nodes on each
!*glass  and Si surface of the etch  depth
!*are pulled at different  distances to
!*equal the etch depth distance.  The
!*nodal deformation simulates bonding.
!*Different distances of the material's
!*nodes are pulled. The total strain energy
!* of all the nodes of each particular
!*distance is summed.  The lowest value
!*of the summed total strain energy is
!*used at that particular distance to
!*calculate the energy release rate, G.
!*This program is an example for
!*deforming 2 nodes on the glass and Si
```

```
!*of a symmetric 300 micron Plaza Test
!*structure. The same program is used
!* to bond glass with CVD  Si carbide, but
!* with different  dimensions.
/PREP7
/NOPR
/PMETH,OFF,0
KEYW,PR_SET,1
KEYW,PR_STRUC,1
KEYW,PR_THERM,0
KEYW,PR_FLUID,0
KEYW,PR_MULTI,0
/GO
!* Geometry
RECTNG,0,500e-6,0,762e-6,
RECTNG,500e-6,800e-6,.2e-6,762e-6,
/REPLOT
RECTNG,0,500e-6,0,-508e-6,
RECTNG,500e-6,800e-6,0,-0.000508,
FLST,2,4,5,ORDE,2
```

```
FITEM,2,1                              FITEM,5,-18
FITEM,2,-4                             CM,_Y,LINE
AGLUE,P51X                             LSEL, , , ,P51X
!*  Plane Strain                       CM,_Y1,LINE
ET,1,PLANE82                           CMSEL,,_Y
!*                                     !*
KEYOPT,1,3,2                           LESIZE,_Y1,10e-006, , , , , , ,1
KEYOPT,1,5,0                           !*
KEYOPT,1,6,0                           TYPE,   1
!*  Material Properties                MAT,      1
MPTEMP,,,,,,,,                         REAL,
MPTEMP,1,0                             ESYS,      0
MPDATA,EX,1,,63.6e9                    SECNUM,
MPDATA,PRXY,1,,.2                      !*
MPTEMP,,,,,,,,                         MSHAPE,0,2D
MPTEMP,1,0                             MSHKEY,0
MPDATA,EX,2,,130.2e9                   !*
MPDATA,PRXY,2,,.279                    FLST,5,2,5,ORDE,2
!* Mesh: Line Spacing                  FITEM,5,6
FLST,5,7,4,ORDE,6                      FITEM,5,8
FITEM,5,1                             CM,_Y,AREA
FITEM,5,3                             ASEL, , , ,P51X
FITEM,5,5                             CM,_Y1,AREA
FITEM,5,9                             CHKMSH,'AREA'
FITEM,5,20                            CMSEL,S,_Y
FITEM,5,-22                           !*
CM,_Y,LINE                            AMESH,_Y1
LSEL, , , ,P51X                       !*
CM,_Y1,LINE                           CMDELE,_Y
CMSEL,,_Y                             CMDELE,_Y1
!*                                     CMDELE,_Y2
LESIZE,_Y1,25e-6, , , , , , ,1        !*
!*                                     TYPE,   1
FLST,5,1,4,ORDE,1                     MAT,      2
FITEM,5,23                           REAL,
CM,_Y,LINE                            ESYS,      0
LSEL, , , ,P51X                       SECNUM,
CM,_Y1,LINE                           !*
CMSEL,,_Y                             FLST,5,2,5,ORDE,2
!*                                     FITEM,5,5
LESIZE,_Y1,.2e-6, , , , , , ,1        FITEM,5,7
!*                                     CM,_Y,AREA
FLST,5,3,4,ORDE,3                     ASEL, , , ,P51X
FITEM,5,4                            CM,_Y1,AREA
FITEM,5,6                            CHKMSH,'AREA'
FITEM,5,19                           CMSEL,S,_Y
CM,_Y,LINE                            !*
LSEL, , , ,P51X                       AMESH,_Y1
CM,_Y1,LINE                           !*
CMSEL,,_Y                             CMDELE,_Y
!*                                     CMDELE,_Y1
LESIZE,_Y1,10e-6, , , , , , ,1        CMDELE,_Y2
!*                                     !*
FLST,5,3,4,ORDE,3                     /UI,MESH,OFF
FITEM,5,14                           !* Boundary Conditions
FITEM,5,17                           FLST,2,2,4,ORDE,2
```

```
FITEM,2,4
FITEM,2,17
DL,P51X, ,SYMM
FLST,2,2,4,ORDE,2
FITEM,2,4
FITEM,2,17
!*
/GO
DL,P51X, ,ALL,0
FLST,2,2,4,ORDE,2
FITEM,2,6
FITEM,2,14
DL,P51X, ,SYMM
FLST,2,2,4,ORDE,2
FITEM,2,6
FITEM,2,14
!*
/GO
DL,P51X, ,UX,0
FLST,2,1,1,ORDE,1
FITEM,2,2
!*  Specific Interfacial Nodal Deformation
/GO
D,P51X, ,-.125e-6, , , ,UY, , , , ,
FLST,2,1,1,ORDE,1

!* plate_bending.mac
!* This program finds the deflection of
!* the bonded die-size sample of glass
!* to Silicon. A 3-D model is built with the
!* dimensions of the rectangular die
!* size sample and fixed at a node on
!*each side of the bonded rectangular
!*piece.  A delta temperature is applied to
!* the structure in order to find the
!*curvature.
/PREP7
!*
!*Define 3-D elements
ET,1,SOLID95
!*
!*Define material properties
MPTEMP,,,,,,,,
MPTEMP,1,0
MPDATA,EX,1,,63.6e9
MPDATA,PRXY,1,,.2
MPTEMP,,,,,,,,
MPTEMP,1,0
UIMP,1,REFT,,,
MPDE,ALPX,1
MPDE,ALPY,1
MPDE,ALPZ,1
MPDATA,ALPX,1,,3.25e-6
MPTEMP,,,,,,,,
MPTEMP,1,0
MPDATA,EX,2,,130e9
```

```
FITEM,2,12736
!*
/GO
D,P51X, ,.075e-006, , , ,UY, , , , ,
FINISH
/SOLU
/STATUS,SOLU
SOLVE
FINISH
/POST1
AVPRIN,0, ,
!* Get Nodal Strain Energy Values
!* and write to .txt file.
PLESOL,SENE, ,2,
*DIM,s_array,array,4742,
*DO,i,1,4742,1
*GET,the_s_energy,ELEM,i,SENE
s_array(i)=the_s_energy
*ENDDO
*CFOPEN,  S_E_1_1_600_1_2, xls
*VWRITE,  s_array(1)
   (E15.9)
*CFCLOSE
!* End of Program

MPDATA,PRXY,2,,.279
MPTEMP,,,,,,,,
MPTEMP,1,0
UIMP,2,REFT,,,
MPDE,ALPX,2
MPDE,ALPY,2
MPDE,ALPZ,2
MPDATA,ALPX,2,,3.3712e-6
!*Define each layer geometry of bimaterial
BLOCK,0,18e-3,0,508e-6,0,12e-3,
BLOCK,0,0.018,0.000508,1270e-6,0,0.012,
!*Glue volumes together
FLST,2,2,6,ORDE,2
FITEM,2,1
FITEM,2,-2
VGLUE,P51X
!*Define thickness element edge length
FLST,5,8,4,ORDE,6
FITEM,5,1
FITEM,5,3
FITEM,5,6
FITEM,5,8
FITEM,5,25
FITEM,5,-28
CM,_Y,LINE
LSEL, , , ,P51X
CM,_Y1,LINE
CMSEL,,_Y
!*
LESIZE,_Y1,150e-6, , , , , , ,1
!*
```

```
!*Mesh each material          CMDELE,_Y
TYPE, 1                       CMDELE,_Y1
MAT,    1                     CMDELE,_Y2
REAL,                         !*
ESYS,    0                    /UI,MESH,OFF
SECNUM,                       !*Define boundary conditions on
!*                            !*each top corner of the plate
SMRT,6                        FLST,2,1,3,ORDE,1
SMRT,7                        FITEM,2,16
SMRT,2                        !*
CM,_Y,VOLU                    /GO
VSEL,,,,    3                 DK,P51X, ,0, ,0,ALL, , , , , ,
CM,_Y1,VOLU                   FLST,2,1,3,ORDE,1
CHKMSH,'VOLU'                 FITEM,2,9
CMSEL,S,_Y                    !*
!*                            /GO
VSWEEP,_Y1                    DK,P51X, ,0, ,0,UX,UY, , , , ,
!*                            FLST,2,1,3,ORDE,1
CMDELE,_Y                     FITEM,2,15
CMDELE,_Y1                    !*
CMDELE,_Y2                    /GO
!*                            DK,P51X, ,0, ,0,UY, , , , , ,
TYPE, 1                       TUNIF,-330,
MAT,    2                     FINISH
REAL,                         /SOLU
ESYS,    0                    /STATUS,SOLU
SECNUM,                       SOLVE
!*                            FINISH
CM,_Y,VOLU                    /POST1
VSEL,,,,    1                 /EFACE,1
CM,_Y1,VOLU                   AVPRIN,0, ,
CHKMSH,'VOLU'                 !*
CMSEL,S,_Y                    !*Print out of deflection contour map in
!*                            !*Y direction
VSWEEP,_Y1                    PLNSOL,U,Y,2,
!*                            !* End of Program
```

[THIS PAGE INTENTIONALLY LEFT BLANK]

References

[1]   Senturia,S.D., <u>Microsystem Design</u>, Kluwer, Boston, M.A., 2001.

[2]   Ko, W.H., Suminto, J.T., and Yeh, G.J., "Bonding Techniques for Microsensors," *Micromachining and micropackaging of Transducers*, Elsevier, Amsterdam, 1985, pp. 41-61.

[3]   Wei, J., Wang, Z.P., Xie, H., and Lan, Ng Fern, "Role of Bonding Temperature and Voltage in Silicon-to-Glass Anodic Bonding," *Proceedings of the 4th Electronics Packaging Technology Conference*, Singapore, 2002, pp.85-90

[4]   Di Cioccio, L., Tiec, Y. Le, Letertre, F., Jaussaud, C., and Bruel, M., "Silicon Carbide on insulator formation using the Smart Cut Process," *Electronic Letters*, Vol. 32, No. 12,1996, pp.1144-1145.

[5]   Jakobsen, H., Lapadatu, A., Kittilsland, G., "Anodic Bonding for MEMS," *Electrochemical Society Proceedings*, Vol. 27,2001,pp. 243-253.

[6]   Nitzsche, P., Lange, K., Schmidt, B., Grigull, S., Kreissig, U., Thomas, B., and Herzog, K., "Ion drift processes in Pyrex-type alkali-borosilicate glass during anodic bonding," *J. Electrochem. Soc.*, Vol.145, No.5,1998, pp.1755-1762.

[7]   Hanneborg, Anders, Nese, Martin, and Ohickers, Per, "Silicon-to-silicon anodic bonding with a borosilicate glass layer," *Journal of Micromech. Microeng.*, Vol. 1, 1991, pp.139-144.

[8]   Yasseen, A. Azzam, Wu, Chien Hung, Zorman, Christian A., Mehregany, Mehran, "Fabrication and Testing of Surface Micromaching Polycrystalline SiC Micromotors," *IEEE Electron Device Letters*, Vol. 21, No.4, 2000, pp.164-166.

[9]   Tong, Q.Y., Lee, T.H., Werner, P., and Gosele, U., Fabrication of Single Crystalline SiC Layer on High Temperature Glass, " *J. Electrochem. Soc.*, Vol. 144, 1997, pp. L111-L113.

[10]   Plaza, J., Esteve, J., Lora-Tamayo, E., "Nondestructive Anodic Bonding Test," *J. Electrochem. Soc.*, Vol.144, No. 5, 1997, pp. L108-110.

[11]   Wallis, George, "Field Assisted Glass-Metal Sealing," *Journal of Applied Physics*, Vol. 40, No. 10, 1969, pp. 3946-3949.

[12]   Albaugh, Kevin, Rasmussen, Don, "Mechanisms of anodic bonding of silicon to Pyrex glass," *Proc. IEEE Solid-State Sensors and Actuators Workshop*, 1988, pp.109-110.

[13]   Xing, Q.F., Yoshida, M., and Sasaki, G., " TEM Study of the interface of anodic-bonded Si/glass," *Scripta Materialia*, Vo. 47, 2002, pp.577-582.

[14]   Enikov, E.T., Boyd, J.G., "A finite-element formulation for anodic bonding," *Smart Materials and Structures*, Vol. 9, 2000, pp. 737-750

[15]   Wallis, George, "Field assisted glass sealing," *Electrocomponent Science and Technology*, Vol. 2, No. 1,1975, pp. 45-53.

[16]   Albaugh, Kevin, "Electrode phenomena during anodic bonding of silicon to sodium borosilicate glass," *J. Electrochem. Soc.*, Vol. 138, No. 10., 1991, pp. 3089-3094

[17]   Cozma, A., Puers, B., "Characterization of the electrostatic bonding of silicon and Pyrex glass," *J. Micromech. Microeng.*, Vol. 5, 1995, pp.98-102.

[18]   Lee, Thomas M.H., Lee, Debbie H.Y., Liaw, Connie Y.N., Lao, Alex I.K., and Hsing, I-Ming, "Detailed characterization of anodic bonding process between glass and thin-film coated silicon substrates," *Sensors and Actuators*, Vol. 86, 2000, pp.103-107.

[19]   Lee, Duck-Jung, Ju, B.K., Jang, Ju, Lee, K.B., and Oh, M.H., "Effects of a hydrophilic surface in anodic bonding," *J. Micromech. Microeng.*, Vol. 9, No. 4, 1999, pp. 313-318.

[20]   Visser, M.M., Plaza, J.A., Wang, D.T., and Hanneborg, A.B., "Chemical analysis of bonded and debonded silicon-glass interfaces," *J. Micromech. Microeng.*, Vol. 11, 2001, pp. N1-N6.

[21]   Tong, Q.-Y., and Gosele, U., Semiconductor Wafer Bonding: Science and Technology, Wiley, New York, 1999.

[22]   Obermeier, E., "Anodic Wafer Bonding," *Electrochemical Society Proceedings*, Vol. 95-7, 1995, pp. 212-220.

[23]   Hurd, D.S., Caretta, R., Gerberich, W.W., "An experimental fracture mechanics study of a strong interface: The silicon/glass anodic bond," *J. Mater. Res.*, Vol. 10, No. 2, 1995, pp.387-400.

[24]   Choi, W.B., Ju, B.K., Lee, Y.H., Jeong, J.W., Haskard, M.R., Lee, N.Y., Sung, M.Y., and Oh, M.H., " Experimental analysis on the anodic bonding with an evaporated glass layer, *J. Micromech. Microeng.*, Vol. 7, 1997, pp.316-322.

[25]   Gerrish, N., and Borenstein, J., D. Charles Stark Draper Laboratory. Private Communications, July 2001.

[26]   Brantley, " Calculated elastic constants for stress problems associated with semiconductor devices, " *J. Appl. Phys.*, Vol. 44, No.1, 1973, pp.534-535.

[27]   Wortman, J.J., Evans, R.A., " Young's Modulus, Shear Modulus, and Poisson's Ratio in Silicon and Germanium, " *J. Appl. Phys.*, Vol. 36, No.1, 1965, pp.153-156.

[28]   EMIS, Properties of Silicon, EMIS Datareviews Series No.4, IMSEPC, The Institution of Electrical Engineers, London and New York, 1988.

[29]   Wallis, George, "Direct-current polarization during field-assisted glass-metal sealing," *J. Amer. Ceram. Soc.*, Vol. 53, 1970, pp.563-567.

[30]   Anderson, T.L., Fracture Mechanics Fundamentals and Applications 2nd Edition, CRC Press, Inc., New York, 1995.

[31]   Wang, J.S., Suo, Z., "Experimental determination of interfacial toughness curves using Brazil nut sandwich," *Aca. Met.*, Vol. 38, No. 7,pp.1279-1290.

[32]   Ashby, M.F., Materials Selection in Mechanical Design, Butterworth-Heinemann, Oxford, 1992.

[33]   Glazov, V.M., Chizhevskaya, S.N., Glazoleva, N.N., Liquid Semiconductors, Plenum Press, New York, 1969.

[34]   Suresh, S., Fatigue of Materials 2nd Edition, Cambridge University Press, United Kingdom, 1998.

[35]   Finot, M., Suresh, S., "Small and Large Deformation of Thick and Thin-Film Multi-Layers: Effects of Layer Geometry, Plasticity, and Compositional Gradients," *J. Mech. Phys. Solids,* Vol. 44, No. 5, pp.683-721.

[36]   Ugural, A., Fenster, S., Advanced Strength and Applied Elasticity 3rd Edition, Prentice Hall, Inc., New Jersey, 1995.

[37]   Moon, Hyung-Soo, Design of Si-SiC Hybrid Structures for Elevated Temperature Micro-Hybrid Turbomachinery, Ph.D. Thesis, Massachusetts Institute of Technology, 2002.

[38]   Ahrens, Thomas J., ed., A Handbook of Physical Constants: Mineral Physics and Crystallography, Vol. 2, American Geophysical Union, Washington, D.C.,1995.

[39]   Timoshenko, and Woinowsky-Krieger, Theory of Plates and Shells, McGraw-Hill, New York, 1959.

[40]   Flinn, P.A., " Principles and Applications of Wafer Curvature Techniques for Stress Measurements in Thin Films, " *Material Research Society Symposium Proceedings*, Vol. 130, 1989, pp. 41-51.

[41]   Shelby, J.E., Effect of Radiation on the Physical Properties of Borosilicate Glasses, *J. Appl. Phys.,* Vol. 51, No. 5, May 1980.

[42]   Bailey, J., Sonoscan^{TM}, Inc., Private Communications, September 2003.